Important Notice

AVO Inversion by Simultaneous
P-P and P-S Inversion

by

Jeffrey A. Larsen

M.Sc. Thesis
University of Calgary
Department of Geology and Geophysics
September, 1999

CREWES

Consortium for Research in Elastic Wave Exploration Seismology

ABSTRACT

This thesis presents a method to simultaneously invert P-P and P-S pre-stack seismic data to derive estimates of compressional and shear impedance values. These estimates of compressional and shear impedance can thus be used to correlate anomalous lithology and pore-fluid content changes in the subsurface. The simultaneous inversion method utilizes a model-based, weighted stacking approach similar to established P-P methods. The primary difference with this method is the inclusion of P-S seismic data and thus a different set of model-based weights. These weighted stacking methods are compared using synthetic data, as well as data from a three-component, three-dimensional (3C-3D) survey from the Blackfoot field in Alberta, Canada.

The simultaneous inversion method has been shown to give similar results to standard P-P weighted stacking methods using synthetic noise-free data. Further results show the simultaneous inversion method performs significantly better in areas of high noise or weak P-P reflectivity than comparable methods using P-P seismic data only.

ACKNOWLEDGEMENTS

TABLE OF CONTENTS

LIST OF FIGURES

LIST OF TABLES

CHAPTER 1

Introduction

1.1 Thesis organization

This thesis is organized as follows. In chapter 1 some background detail regarding elastic rock properties and their link with lithology and pore-fluid content are discussed. Further discussion includes the application of P-wave amplitude variation with offset (AVO) methods and multi-component seismology to derive estimates of these rock properties. Chapter 2 contains a number of accuracy tests for P-S reflectivity approximations and a simple density-compressional impedance relation. The complete derivation of a least-squares, linearized simultaneous inversion method for all single mode conversions at a given interface (P-P, P-S, S-P and S-S modes) is also developed. Chapter 2 further discusses the potential for non-linear simultaneous inversion using the exact Zoeppritz equation solution via the Generalized Linear Inversion method.

In chapter 3, the weighting behavior of the 2-parameter linearized, simultaneous inversion method is examined and compared to a standard method utilizing P-P seismic data only. Simultaneous inversion accuracy is then tested and compared to the same standard P-P method. Next, a comparison of inversion accuracy is undertaken in the presence of noisy data for the simultaneous and P-P inversion methods. A series of tests are then performed to measure inversion accuracy using a limited-offset stacking

procedure rather than each offset contribution directly. The simultaneous inversion method is then applied to synthetic data derived from well logs in the Blackfoot field. The inversion results using this data will be examined using both noise-free and synthetic data containing varying levels of noise. Finally, additional sources of error are discussed in relation to using the simultaneous inversion method on surface seismic data.

In chapter 4 the simultaneous inversion method is applied to 3C-3D seismic data from the Blackfoot field. The processing of the vertical and radial component seismic datasets will first be discussed. Reflection events in these datasets are then correlated in depth and formed into weighted stacks of normalized compressional and shear impedance reflectivity. These weighted stacks are then compared for the two inversion methods and several conclusions are made regarding the validity of each inversion method.

1.2 Introduction

In recent years the potential benefit of incorporating multi-component seismic data has been realized. This topic is currently of major interest in the petroleum exploration industry and was the subject of a recent SEG workshop in 1998. The primary goal of this study is to directly link the amplitude variation with offset (AVO) response with multi-component seismic data. This study will also show the benefit in performing AVO analyses simultaneously rather than separately.

1.2.1 Background

P-wave velocity (Vp or α), S-wave velocity (Vs or β) and density (ρ) can be used to describe the rock matrix and pore fluid properties in a given rock. Pickett (1963) found that sandstones, limestones and dolomites could be differentiated using Vp/Vs. Domenico (1977) further observed that Vp/Vs was useful in discriminating sandstone, calcareous sandstone, limestone, dolomite and shale. Domenico (1977) further observes that Vp and Vs are higher for clean sandstones than shaley sandstones. Further examples from the literature indicating the utility of Vp/Vs as a lithology discriminator, including: Johnson (1988; sands versus carbonates), Fuller et al. (1989; sand versus shale), Ramirez (1990; salt versus clastics), and Mazotti (1984; high-velocity layers in general). Koefoed (1955)

observed the dependence between lithology and Poisson's ratio, and Shuey (1985) applied this observation to amplitude variation with offset (AVO) measurements using a linearized approximation to the Zoeppritz equations (Aki and Richards, 1980).

A number of authors have observed the link between Vp, Vs and pore fluid content. Biot (1956), Gardner and Harris (1968), Kuster and Töksoz (1974), Wang and Nur (1987) all noted the impact upon Vp and Vs by pore fluid content. Tatham and Stoffa (1976) further observed a characteristic drop in Vp/Vs for gas-saturated sandstones. It was further shown by Ito et al. (1979) that the impact of steam upon rock Vp/Vs is very similar to the effect of in-situ natural gas. This observation was applied in conjunction with AVO methods to show its effectiveness in monitoring heavy oil recovery (Tsingas and Kanasewich, 1991). The effect of different hydrocarbon saturations on Vp, Vs and Vp/Vs also has been studied. Domenico (1977) and Murphy (1984) found that Vp and Vp/Vs decrease significantly in consolidated rock with increasing gas saturation. Castagna et al. (1985) show that in wet sandstones Vp/Vs will decrease with increasing gas saturation. Toksoz et al. (1976) observed the influence upon Vp and Vs velocities due to porosity. These observations show that Vp significantly decreases with increasing gas saturation and Vs remains relatively independent of pore fluid content.

The development of AVO methods has further encouraged the need for true-amplitude seismic processing. Of primary importance to the goal of true-amplitude processing is the use of true-amplitude seismic migration. Gray (1997) points out the interpretation of AVO using unmigrated records is commonly hindered by the effects of common-depth point smear, incorrectly specified geometrical spreading loss, source-receiver directivty as well as other factors. It should thus be possible to correct some of these problems by analysing common-reflection-point gathers after prestack migration assuming the migration being used is a true-amplitude method. A true-amplitude migration is thus a method of removing amplitude and phase distortions to produce angle-dependant reflection coefficients in a lossless, isotropic, elastic earth model. A number of authors have discussed these true-amplitude migration methods, (Bortfeld and Tan, 1984; Schneider and Krey, 1985; Krajewski et al., 1993). The use of 3D migration

in AVO is also desirable since using 2D migration on real seismic data introduces amplitude and phase errors into the reconstruction of a 3D earth.

Several authors have commented that more physical insight is provided by the rigidity modulus μ (Wright, 1986; Thomsen, 1990; Castagna et al., 1993). Stewart (1995) discusses the potential usefulness of the Lame parameters (λ-compressibility and μ-shear) to better differentiate rock properties. Goodway et al. (1997) applied this observation to show λ, μ and λ/μ are more sensitive to changes in rock properties than Vp, Vs and Vp/Vs.

1.2.2 P-wave AVO methods

With the development of multi-offset recording in the 1960's, lithological estimation methods finally became viable. Early techniques of lithology estimation were focussed on zero-offset or post-stack inversion methods (Lindseth, 1979). These methods along with "bright spot" analysis techniques gave a very simple model of the seismic response. Ostrander (1984) demonstrated that gas-sand reflection coefficients vary in an anomalous fashion with increasing offset and showed how to utilize this behavior as a direct hydrocarbon indicator. Ostrander (1982) further proposed using pre-stack seismic amplitudes to extract information about lithology and pore-fluids. Since then, AVO has been used with varied rates of success. New developments in seismic acquisition and processing in recent years have improved the promise of this method. The simplest methods of AVO analysis are the "Reconnaissance methods" (Hampson and Russell, 1990). These methods are simple to use and include methods such as partial stacking (limited-offset stacking) and gradient-intercept methods.

Shuey (1985) developed a gradient-intercept method that measures zero-offset reflectivity and changes in Poisson's ratio. This method, though useful, requires a fixed Vp/Vs ratio and thus may be invalid if a poor initial model is used. Smith and Gidlow (1987) developed a method using least-squares inversion to apply a set of model-based weights in an offset dependant manner, to form estimates of fractional Vp and Vs

velocities. This method does not assume a fixed background Vp/Vs, but does incorporate a smoothed background model independent of the estimates of fractional compressional and shear velocity, i.e. the difference between the velocities of two layers divided by the average velocity of the same two layers. Fatti et al. (1994), further improved upon the Smith-Gidlow or "Geo-stack" method by incorporating density changes instead of using an empirical relationship between Vp and density (Gardner et al., 1974). This method derives estimates of fractional compressional and shear impedance instead of Vp and Vs directly. Macdonald et al. (1987) and Russell (1988) discuss the Generalized Linear Inversion method (GLI) and apply it to directly invert the Zoeppritz equations (Aki and Richards, 1980). The GLI method, though less simple to use than those previously described, does not rely upon approximations to the Zoeppritz equations. Rijssen and Herman (1988), and de Haas and Berkhout (1989) show that the addition of multi-component reflection seismic data can significantly improve estimates of elastic parameters.

1.2.3 Converted-wave seismology

Ricker and Lynn (1950) first observed the potential benefits of converted wave seismology. In recent years, the use of P-S seismic data has increased as a result of new developments in acquisition and processing technology. Stewart (1994) observed the increasing use of converted wave seismic data in modern seismic exploration. It has been shown that supplementary P-S seismic data increases interpretation confidence, provides additional imaging constraints and is useful to provide rock property estimates. In addition, P-S seismic data can be obtained at relatively low cost from 3-component (3-C) seismic recordings since conventional sources and receiver geometries are employed.

Compressional waves incident upon an interface at non-zero offset are partitioned into transmitted and reflected P and S waves. Waters (1992) observes significant converted wave energy is available using standard acquisition techniques. Stewart (1996) observed the following benefits of incorporating P-S seismic data:

1. Provides another section with independent properties (e.g., velocity, multiples, tuning)

2. Imaging interfaces with low P-wave reflectivity contrast (e.g. imaging through gas chimneys)

3. Assist P-P interpretation via long wavelength Vp/Vs values and additional sections

4. Augmenting conventional AVO analysis

5. Investigating anisotropy and fractures

6. Calibrating P-wave bright spots

7. Vector filtering and side-scanning

8. Using Vp/Vs for lithology

9. Monitoring reservoir changes

Table 1.1: Advantages of incorporating P-S seismic data

1.3 Thesis objective

The goal of this thesis is to compute estimates of elastic parameters from the simultaneous inversion of P-P and P-S data. A theoretical development of the inversion equations used in this method is presented. These simultaneous inversion equations are then evaluated using synthetic and field seismic data. It is hoped this work will improve the signal-to-noise ratio, and thus the accuracy of pre-stack impedance inversion by incorporating a simultaneous inversion method rather than a P-P inversion method alone.

1.4 Data used

The simultaneous P-P and P-S weighted stack and inversion procedure was evaluated using the following datasets.

1.4.1 Blackfoot 3C-3D

The Blackfoot 3C-3D dataset was acquired over the Blackfoot field in October 1996. The field is owned and operated by PanCanadian Petroleum Ltd. and is located south-east of Strathmore, Alberta (Township 23, Range 23W4). The objectives of this survey were to demonstrate that 3C-3D seismic data could be used to improve conventional 3D P-wave data, provide additional stratigraphic and structural images,

discriminate lithology, and test for anisotropy (Lawton et al., 1996). The Blackfoot 3C-3D survey was recorded in two overlapping patches, the first designed to target the clastic Glauconitic channel, the second to target a deeper, reef-prone Beaverhill Lake carbonate prospect. In this study only the Glauconitic patch is considered. The acquisition parameters for the Blackfoot 3C-3D Glauconitic patch are summarized in table 1.2 below.

Source Parameters	
Line orientation:	North-south
Source interval:	60m
Source line interval:	210m
Number of source lines:	24
Total number of source points:	720
Source depth:	18m
Receiver parameters	
Line orientation:	East-west
Receiver interval:	60m
Receiver line interval:	255m
Number of receiver lines:	18
Total number of receivers:	690
Receiver depth:	0.5m

Table 1.2: Blackfoot 3C-3D acquisition parameters (Glauconitic patch)

1.4.2 Synthetic data

The synthetic P-P and P-S data of chapter 3 were generated using a multi-offset synthetic seismogram (Lawton and Howell, 1992; Margrave and Foltinek, 1995) and blocked models of depth vs. Vp, Vs and density. These models were then raytraced for P-P and P-S incidence angles, and amplitudes were calculated using the Zoeppritz equations. The resulting P-P and P-S offset gathers were then used to evaluate the performance of various simultaneous inversion methods under investigation.

The synthetic data of chapter 3 were generated using sonic and density logs from wells 09-08-023-23W4, 08-08-023-23W4 and 09-17-023-23W4. All logs were blocked by a median filtering process for each picked formation top interval. Well 08-08-023-23W4 is a multi-zone producer with gas from the Upper Channel and oil from the Lower

Glauconitic Channel interval. Well 09-17-023-23W4 is a non-producing well representing the regional position of the Blackfoot prospect. Well 09-08-023-23W4 contained dipole sonic and density data from the surface to the top of the Glauconitic channel. Logs 08-08-023-23W4 and 09-17-023-23W4 contain dipole sonic and density data from roughly the Mannville to Mississippian interval. These two logs were subsequently spliced below the regional coal_3 marker and added to the 09-08-023-23W4 well log at the same marker. Two modified logs of wells 08-08-023-23W4 and 09-17-023-23W4 were thus generated representing a producing Glauconitic well and a non-producing regional well. Raytracing of these modified wells logs was then performed to produce P-P and P-S incidence, reflection and transmission angles. Synthetic P-P and P-S gathers were then generated using these well logs and a set of pre-determined band-passed wavelets.

1.5 Hardware and software used

The work presented in this thesis was created on a SUN MICROSYSTEMS network operated by the CREWES Project of the Department of Geology and Geophysics at the University of Calgary. The majority of programming was done in the MATLAB programming language. This includes the weighted stack algorithm, well log smoothing and P-P and P-S event correlation modules. A number of other MATLAB-based programs coded by Dr. Gary Margrave of the University of Calgary were also utilized in this research. Synthetic data were generated using SYNTH, a seismic modeling package originally developed by Dr. Ed Krebes and Dr. Don Lawton of the University of Calgary, and later coded in MATLAB by Dr. Gary Margrave and Mr. Darren Foltinek also of the University of Calgary. The Blackfoot 3C-3D data were processed to limited-offset gathers on PROMAX by Ms. Han-Xing Lu and Dr. Gary Margrave of the CREWES Project. Seismic interpretation, event flattening and SEG-Y export was performed using SEIS-X interpretation software. All images in this thesis were screen captured using XV. Image processing was done on PC computers using PHOTOSHOP, CANVAS and MICROSOFT PHOTO EDITOR. Word processing and thesis assembly was done on a PC based computer using MICROSOFT WORD.

CHAPTER 2

Simultaneous P-P And P-S Inversion Theory

2.1 Introduction

A simultaneous P-P and P-S linearized AVO inversion method is presented. This method is based upon a previous weighted stacking method utilizing P-P seismic data only (Smith and Gidlow, 1987) and its extension by Stewart (1990). In the case of this study, this method will be further extended not only to the P-P and P-S cases, but also to the case incorporating all single reflected mode conversions at a given interface (P-P, P-S, S-P and S-S modes). This method utilizes normal moveout (NMO) corrected common mid point (CMP) (P-P case) and common conversion point (CCP) (P-S case) gathers into a weighted stack where the weights are derived from a smoothed background velocity model. The resulting sets of stacked sections can be thought of as normalized changes of P-wave impedance and S-wave impedance stacks. From these weighted stacks, a number of useful elastic parameters can be derived. The inversion of these weighted stacks can be performed in much the same way as for P-P inversion.

2.2 Zoeppritz equation approximations

The Zoeppritz equations fully describe the relationship between incident and reflection/transmission amplitudes for plane waves at a welded elastic interface. The

boundary conditions for these equations vary depending upon the elastic media on either side of the welded elastic interface. These boundary conditions for a solid-solid interface include continuity of tangential and normal displacement, as well as continuity of normal and tangential stress. The equations are fully described in matrix form by Aki and Richards (1980). These authors further simplified these equations into a series of first order Zoeppritz equation approximations for plane-wave reflection and transmission coefficients at a welded interface, between two solid half-spaces. These linearized approximations for P-P and P-S reflection coefficients, R_{PP} and R_{PS}, are

$$R_{PP}(\theta) \approx \frac{1}{2}\left(1 - 4\frac{\beta^2}{\alpha^2}\sin^2\theta\right)\frac{\Delta\rho}{\rho} + \frac{1}{2\cos^2\theta}\frac{\Delta\alpha}{\alpha} - \frac{4\beta^2}{\alpha^2}\sin^2\theta\frac{\Delta\beta}{\beta} \qquad (2.1)$$

$$R_{PS}(\theta,\varphi) \approx \frac{-\alpha\tan\varphi}{2\beta}\left[\left(1 - \frac{2\beta^2}{\alpha^2}\sin^2\theta + \frac{2\beta}{\alpha}\cos\theta\cos\varphi\right)\frac{\Delta\rho}{\rho} - \right.$$

$$\left. \left(\frac{4\beta^2}{\alpha^2}\sin^2\theta - \frac{4\beta}{\alpha}\cos\theta\cos\varphi\right)\frac{\Delta\beta}{\beta}\right] \qquad (2.2)$$

where α, β, ρ are the average P-wave, S-wave and density values across an interface, $\Delta\alpha$, $\Delta\beta$, $\Delta\rho$ are the P-wave, S-wave and density contrasts across an interface, θ is the average of the P-wave angle of incidence and transmission across the interface, and φ is the average of the shear wave angle of reflection and transmission across the interface. Equations 2.1 and 2.2 are derived assuming small relative changes in elastic parameters and for angles θ and φ that do not approach a critical angle or 90 degrees (Aki and Richards, 1980). These equations can be reformulated as functions of P-wave and S-wave impedance, i.e. $I = \alpha\rho$ ($\Delta I/I = \Delta\alpha/\alpha + \Delta\rho/\rho$) and $J = \beta\rho$ ($\Delta J/J = \Delta\beta/\beta + \Delta\rho/\rho$) as

$$R_{PP}(\theta) \approx \frac{\left(1 + \tan^2\theta\right)}{2}\frac{\Delta I}{I} - 4\frac{\beta^2}{\alpha^2}\sin^2\theta\frac{\Delta J}{J} - \left[\frac{1}{2}\tan^2\theta - 2\frac{\beta^2}{\alpha^2}\sin^2\theta\right]\frac{\Delta\rho}{\rho} \qquad (2.3)$$

$$R_{PS}(\theta,\varphi) \approx \frac{-\alpha\tan\varphi}{2\beta}\left[\left(1 + 2\sin^2\varphi - \frac{2\beta}{\alpha}\cos\theta\cos\varphi\right)\frac{\Delta\rho}{\rho} - \right.$$

$$\left. \left(4\sin^2\varphi - \frac{4\beta}{\alpha}\cos\theta\cos\varphi\right)\frac{\Delta J}{J}\right]. \qquad (2.4)$$

The density contrast term in equation 2.3 is small for angles of incidence θ less than 35 degrees and α/β velocity ratio between 1.5 and 2.0 (Gidlow et al., 1992). This term can be re-written using Gardner's relation (Gardner et al., 1974) as

$$\rho \approx a\alpha^{1/4}. \tag{2.5}$$

Equation 2.5 can be differentiated and both sides divided by equation 2.5 to give

$$\frac{\Delta\rho}{\rho} = \frac{1}{4}\frac{\Delta\alpha}{\alpha}. \tag{2.6}$$

Thus, fractional changes in density can be written as a function of P-wave impedance

$$\frac{\Delta\rho}{\rho} = \frac{1}{5}\left(\frac{4\Delta\rho}{\rho} + \frac{\Delta\rho}{\rho}\right) = \frac{1}{5}\left(\frac{\Delta\alpha}{\alpha} + \frac{\Delta\rho}{\rho}\right) = \frac{1}{5}\frac{\Delta I}{I}. \tag{2.7}$$

This method of treating the fractional density term in equations 2.3 and 2.4 as a P-wave impedance term is generally an improvement over simply neglecting this term since there is usually a linear dependence between compressional velocity and density.

2.2.1 P-S reflectivity approximation accuracy

A number of authors have discussed the relative accuracy of first and higher order P-S Zoeppritz equation approximations (eg. Xu and Bancroft, 1997). The equations of Aki and Richards were chosen because they incorporate all possible reflected modes at a given interface. For the simple case of a 3 layer earth model, summarized in table 2.1, the first order Aki and Richards approximations are calculated and compared to the exact solution in figure 2.1.

Layer	α (m/s)	Δα/α	β (m/s)	Δβ/β	ρ(g/cc)	Δρ/ρ	ΔI/I	ΔJ/J
1	4200	-0.1000	2120	0.0900	2.58	-0.0395	-0.1395	0.0505
2	3800		2320		2.48			
3	4200	0.1000	2120	-0.0900	2.58	0.0395	0.1395	-0.0505

Table 2.1: Simple three layered earth model.
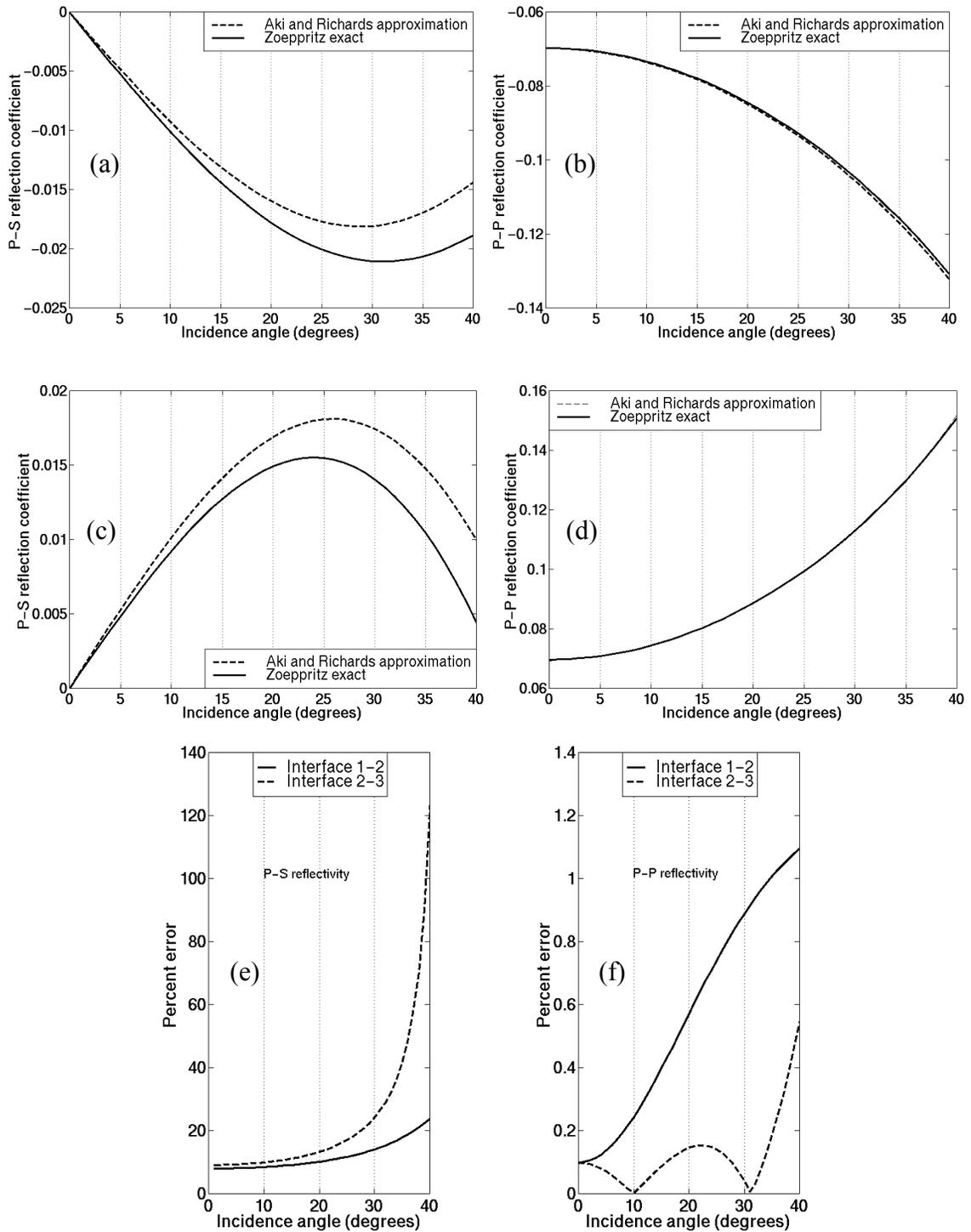
Figure 2.1: P-P (a) and P-S reflectivity (b) curves at the layer 1-2 boundary. P-c) and P-S reflectivity (d) curves at the layer 2-3 boundary. Percent error plots for P-S (e) and P-P (f) reflectivities.

Notice the P-P Zoeppritz equation approximation accuracy is significantly better than the P-S approximation. Higher order approximations may also be used to improve the accuracy of both P-P and P-S reflectivity. For instance the second order P-S reflectivity approximation (Xu and Bancroft, 1997) of equation 2.4 can be written as

$$R_{PS} \approx A\left[B_1\frac{\Delta\rho}{\rho}+B_2\frac{\Delta\beta}{\beta}+B_3\left(\frac{\Delta\rho}{\rho}\right)^2+B_4\left(\frac{\Delta\rho}{\rho}\frac{\Delta\alpha}{\alpha}\right)+B_5\left(\frac{\Delta\rho}{\rho}\frac{\Delta\beta}{\beta}\right)+B_6\left(\frac{\Delta\alpha}{\alpha}\frac{\Delta\beta}{\beta}\right)+B_7\left(\frac{\Delta\beta}{\beta}\right)^2\right] \qquad (2.8)$$

where A, B_1, B_2, B_3, B_4, B_5, B_6 and B_7 are functions of θ, φ, α and β.

Equation 2.8 will now result in a more accurate approximation to the P-S reflection coefficient, but is impractical due to the increased number of terms in the equation and the nonlinear dependence on the velocity and density contrasts.

2.2.2 Density-compressional impedance relation accuracy

The re-casting of equations 2.1 and 2.2 into functions of P-wave and S-wave impedance may introduce errors into the final inversion result. As shown by Gidlow et al. (1992), equation 2.3 can be considered accurate for values of α/β from 1.5 to 2.0 and for angles of incidence less than 35 degrees. From the assumption made in equation 2.7, equation 2.4 can be written as

$$R_{PS}(\theta,\varphi) = C(\theta,\varphi)\frac{\Delta\rho}{\rho} + D(\theta,\varphi)\frac{\Delta J}{J} \approx \frac{C(\theta,\varphi)}{5}\frac{\Delta I}{I} + D(\theta,\varphi)\frac{\Delta J}{J}. \qquad (2.9)$$

To test the accuracy of equation 2.9, a series of models were constructed representing a variety of lithological situations. The results of this test using elastic constants given in table 2.1 are summarized in figure 2.2.
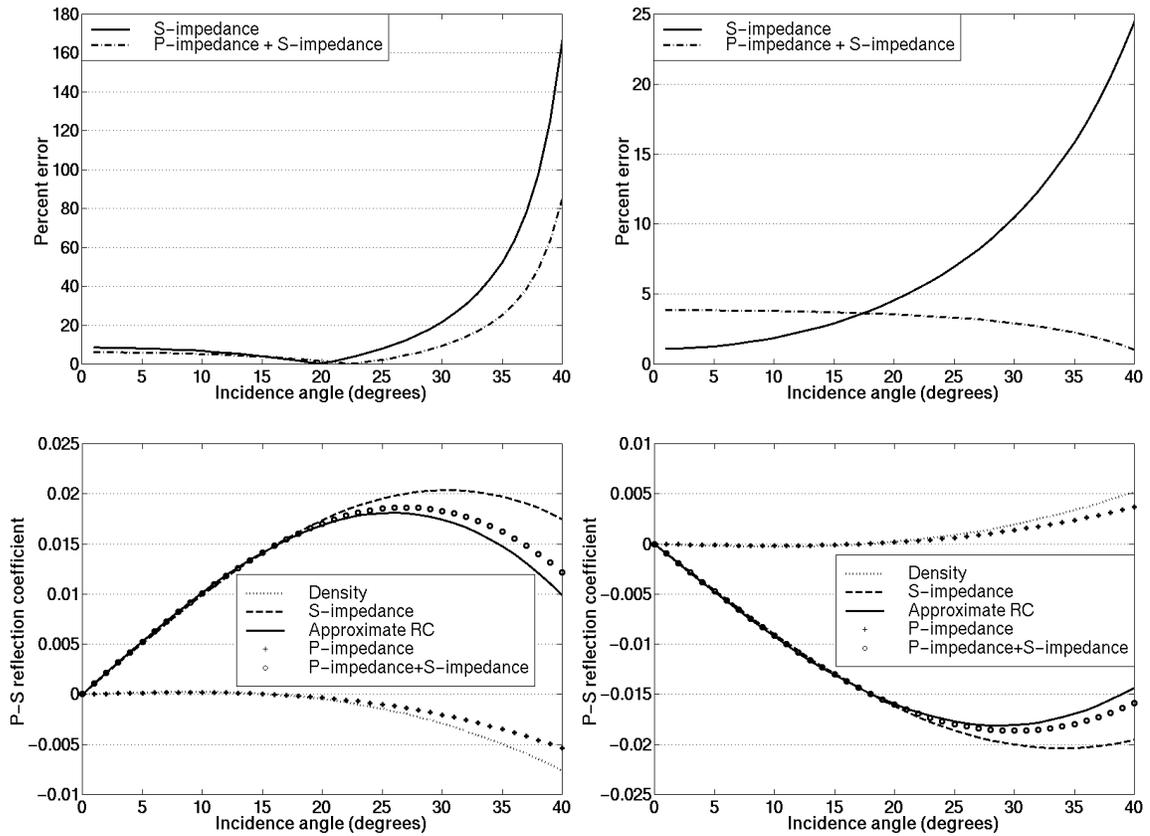
Figure 2.2: Accuracy tests for the case of the layer 1-2 interface (left) and the layer 2-3 interface (right) for equation 2.4. Notice the improvement using relationship between density and P-wave impedance in equation 2.7.

In figure 2.2 above, the density term represents the $C(\theta,\varphi)\cdot(\Delta\rho/\rho)$ contribution in equation 2.9, the S-impedance term equals $D(\theta,\varphi)\cdot(\Delta J/J)$, the approximate RC term equals $R_{PS}(\theta,\varphi)$ and the P-impedance term equals $(1/5)\cdot C(\theta,\varphi)\cdot(\Delta I/I)$. Notice the strong dependence the P-S reflection coefficient has with S-wave impedance. Density becomes a more significant factor with increasing offset. This simple three layer model incorporates a significant $\Delta\rho/\rho$ ratio of 0.0395 and a $\Delta\alpha/\alpha$ ratio of 0.1. Thus, this model incorporates a reasonable deviation from the assumption made in equation 2.7. The accuracy of equation 2.4 will improve with values closer to the assumption that $\Delta\rho/\rho=(1/4)\Delta\alpha/\alpha$. A similar result can be obtained for equation 2.3, but is generally not necessary unless the assumptions made by Gidlow et al. (1992) do not hold.

2.3 Simultaneous linearized P-P and P-S inversion

Smith and Gidlow (1987) outline a least-squares, weighted-stacking procedure incorporating P-P seismic data to extract compressional and shear velocities. This method utilizes NMO corrected pre-stack P-P seismic data. Ferguson (1996) describes a similar method to derive estimates of shear velocity directly from an NMO corrected CCP gather. Both methods utilize a background velocity-depth model to compute incidence, reflection and transmission angles. The primary disadvantage of the P-S method is the need for an additional background $\Delta\rho/\rho$ density model. A true simultaneous method first given by Stewart (1990) outlines a procedure that incorporates both P-P and P-S seismic gathers in a joint P-P and P-S inversion. This method contains several inherent advantages over either the P-P or P-S stand-alone methods. These advantages are summarized below.

1. A larger amount of data (i.e. P-P and P-S datasets) is incorporated into each estimate of $\Delta I/I$ and $\Delta J/J$. This has the potential to improve signal-to-noise and thus accuracy for each estimate.

2. Shear impedance estimates are improved, since P-S reflectivity is generally more dependent upon shear impedance contrast compared with P-P reflectivity.

3. A joint interpretation of P-P and P-S seismic data is required and thus has other benefits such as long-wavelength estimates of Vp/Vs from Ts/Tp ratios.

4. Elastic parameter estimates are improved in areas where P-P reflectivity contrasts are weak or noisy due to acquisition or geological conditions.

5. A simultaneous inversion results in a different set of weights for the P-P dataset, which may be beneficial for signal-to-noise considerations.

2.3.1 Derivation of linearized simultaneous inversion equations

At a given welded solid-solid interface, 4 possible reflection mode conversions may take place. These are commonly referred to as the P-P, P-S, S-P and S-S reflected modes. Aki and Richards give the S-P and S-S Zoeppritz equation approximations as

$$R_{SP}(\theta,\varphi) = -\tan\theta\frac{\beta}{\alpha}\left[\left(1-2\sin^2\varphi+\frac{2\beta}{\alpha}\cos\theta\cos\varphi\right)\frac{\Delta\rho}{\rho}-\right.$$

$$\left.\left(4\sin^2\varphi-\frac{4\beta}{\alpha}\cos\theta\cos\varphi\right)\frac{\Delta\beta}{\beta}\right] \tag{2.10}$$

$$R_{SS}(\varphi) = -\frac{1}{2}\left(1-4\sin^2\varphi\right)\frac{\Delta\rho}{\rho}-\left(\frac{1}{2\cos^2\varphi}-4\sin^2\varphi\right)\frac{\Delta\beta}{\beta}. \tag{2.11}$$

After applying the assumption in equation 2.7, equations 2.10 and 2.11 can be written as

$$R_{SP}(\theta,\varphi) = -\tan\theta\frac{\beta}{\alpha}\left[\frac{1}{5}\left(1+2\sin^2\varphi-\frac{2\beta}{\alpha}\cos\theta\cos\varphi\right)\frac{\Delta I}{I}-\right.$$

$$\left.\left(4\sin^2\varphi-\frac{4\beta}{\alpha}\cos\theta\cos\varphi\right)\frac{\Delta J}{J}\right] \tag{2.12}$$

$$R_{SS}(\varphi) = -\frac{1}{10}\left(1+4\sin^2\varphi-\frac{1}{\cos^2\varphi}\right)\frac{\Delta I}{I}-\left(\frac{1}{2\cos^2\varphi}-4\sin^2\varphi\right)\frac{\Delta J}{J}. \tag{2.13}$$

Equations 2.3 (after neglecting the $\Delta\rho/\rho$ term), 2.9, 2.12 and 2,13 can now be written as

$$R_{PP}(\theta) = A(\theta)\frac{\Delta I}{I}+B(\theta)\frac{\Delta J}{J} \tag{2.14}$$

$$R_{PS}(\theta,\varphi) = C(\theta,\varphi)\frac{\Delta I}{I}+D(\theta,\varphi)\frac{\Delta J}{J} \tag{2.15}$$

$$R_{SP}(\theta,\varphi) = E(\theta,\varphi)\frac{\Delta I}{I}+F(\theta,\varphi)\frac{\Delta J}{J} \tag{2.16}$$

$$R_{SS}(\varphi) = G(\varphi)\frac{\Delta I}{I}+H(\varphi)\frac{\Delta J}{J}. \tag{2.17}$$

where

$$A(\theta) = \frac{\left(1+\tan^2\theta\right)}{2} \tag{2.18}$$

$$B(\theta) = -4\frac{\beta^2}{\alpha^2}\sin^2\theta \tag{2.19}$$

$$C(\theta,\varphi) = \frac{-\alpha\tan\varphi}{10\beta}\left(1+2\sin^2\varphi-2\frac{\beta}{\alpha}\cos\theta\cos\varphi\right) \tag{2.20}$$

$$D(\theta, \varphi) = \frac{\alpha \tan \varphi}{\beta}\left(2\sin^2 \varphi - 2\frac{\beta}{\alpha}\cos \theta \cos \varphi\right) \qquad (2.21)$$

$$E(\theta, \varphi) = \frac{-\sin \varphi}{10\cos \theta}\left(1 + 2\sin^2 \varphi - 2\frac{\beta}{\alpha}\cos \theta \cos \varphi\right) \qquad (2.22)$$

$$F(\theta, \varphi) = \frac{\sin \varphi}{\cos \theta}\left(2\sin^2 \varphi - 2\frac{\beta}{\alpha}\cos \theta \cos \varphi\right) \qquad (2.23)$$

$$G(\varphi) = -\frac{1}{10}\left(1 - 4\sin^2 \varphi\right) \qquad (2.24)$$

$$H(\varphi) = 4\sin^2 \varphi - \frac{1}{2\cos^2 \varphi} \qquad (2.25)$$

Assume that the background velocities are described by a smoothly varying P-wave velocity-depth model and an equally smoothed β/α model. Raytracing can be performed on these smooth background models to determine the incidence, reflection and transmission angles. The weights A, B, C, D, E, F, G and H are functions of only the P-wave velocity-depth model and the β/α model, and not of the data itself. Let N be the number of offsets contributing to each NMO corrected CMP or CCP gather at a particular time sample under consideration. If the actual amplitude of a given event in each offset gather is given by R_{PP}, R_{PS}, R_{SP} and R_{SS}, the mean square error of all amplitudes compared with the model curve is given by

$$\varepsilon = \sum_{i=1}^{N}\left[\left(R_{PPi} - A_i\frac{\Delta I}{I} - B_i\frac{\Delta J}{J}\right)^2 + \left(R_{PSi} - C_i\frac{\Delta I}{I} - D_i\frac{\Delta J}{J}\right)^2 + \right.$$

$$\left. \left(R_{SPi} - E_i\frac{\Delta I}{I} - F_i\frac{\Delta J}{J}\right)^2 + \left(R_{SSi} - G_i\frac{\Delta I}{I} - H_i\frac{\Delta J}{J}\right)^2\right]. \qquad (2.26)$$

Expanding the squared terms in 2.26 and distributing the same, results in

$$\varepsilon = \left[\left(\frac{\Delta I}{I}\right)^2\sum_{i=1}^{N}A_i^2 + \left(\frac{\Delta J}{J}\right)^2\sum_{i=1}^{N}B_i^2 + \sum_{i=1}^{N}R_{PPi}^2 + 2\frac{\Delta I}{I}\frac{\Delta J}{J}\sum_{i=1}^{N}(A_iB_i) - 2\frac{\Delta I}{I}\sum_{i=1}^{N}(A_iR_{PPi}) - \right.$$

$$2\frac{\Delta J}{J}\sum_{i=1}^{N}(B_iR_{PPi}) + \left(\frac{\Delta I}{I}\right)^2\sum_{i=1}^{N}C_i^2 + \left(\frac{\Delta J}{J}\right)^2\sum_{i=1}^{N}D_i^2 + \sum_{i=1}^{N}R_{PSi}^2 + 2\frac{\Delta I}{I}\frac{\Delta J}{J}\sum_{i=1}^{N}(C_iD_i) -$$

$$2\frac{\Delta I}{I}\sum_{i=1}^{N}(C_iR_{PSi})-2\frac{\Delta J}{J}\sum_{i=1}^{N}(D_iR_{PSi})+\left(\frac{\Delta I}{I}\right)^2\sum_{i=1}^{N}E_i^2+\left(\frac{\Delta J}{J}\right)^2\sum_{i=1}^{N}F_i^2+\sum_{i=1}^{N}R_{SPi}^2+$$

$$2\frac{\Delta I}{I}\frac{\Delta J}{J}\sum_{i=1}^{N}(E_iF_i)-2\frac{\Delta I}{I}\sum_{i=1}^{N}(E_iR_{SPi})-2\frac{\Delta J}{J}\sum_{i=1}^{N}(F_iR_{SPi})+\left(\frac{\Delta I}{I}\right)^2\sum_{i=1}^{N}G_i^2+\left(\frac{\Delta J}{J}\right)^2\sum_{i=1}^{N}H_i^2+$$

$$\sum_{i=1}^{N}R_{SSi}^2+2\frac{\Delta I}{I}\frac{\Delta J}{J}\sum_{i=1}^{N}(G_iH_i)-2\frac{\Delta I}{I}\sum_{i=1}^{N}(G_iR_{SSi})-2\frac{\Delta J}{J}\sum_{i=1}^{N}(H_iR_{SSi})\bigg]. \tag{2.27}$$

Next, the mean-square error ε must be minimized, this is done by taking the partial derivative of ε with respect to ΔI/I and ΔJ/J and setting the result equal to zero

$$\frac{\partial\varepsilon}{\partial\left(\frac{\Delta I}{I}\right)}=\bigg[2\frac{\Delta I}{I}\sum_{i=1}^{N}A_i^2+2\frac{\Delta J}{J}\sum_{i=1}^{N}A_iB_i-2\sum_{i=1}^{N}A_iR_{PPi}+2\frac{\Delta I}{I}\sum_{i=1}^{N}C_i^2+2\frac{\Delta J}{J}\sum_{i=1}^{N}C_iD_i-$$

$$2\sum_{i=1}^{N}C_iR_{PSi}+2\frac{\Delta I}{I}\sum_{i=1}^{N}E_i^2+2\frac{\Delta J}{J}\sum_{i=1}^{N}E_iF_i-2\sum_{i=1}^{N}E_iR_{SPi}+2\frac{\Delta I}{I}\sum_{i=1}^{N}G_i^2+$$

$$2\frac{\Delta J}{J}\sum_{i=1}^{N}G_iH_i-2\sum_{i=1}^{N}G_iR_{SSi}\bigg]=0 \tag{2.28}$$

$$\frac{\partial\varepsilon}{\partial\left(\frac{\Delta J}{J}\right)}=\bigg[2\frac{\Delta I}{I}\sum_{i=1}^{N}A_iB_i+2\frac{\Delta J}{J}\sum_{i=1}^{N}B_i^2-2\sum_{i=1}^{N}B_iR_{PPi}+2\frac{\Delta I}{I}\sum_{i=1}^{N}C_iD_i+2\frac{\Delta J}{J}\sum_{i=1}^{N}D_i^2-$$

$$2\sum_{i=1}^{N}D_iR_{PSi}+2\frac{\Delta I}{I}\sum_{i=1}^{N}E_iF_i+2\frac{\Delta J}{J}\sum_{i=1}^{N}F_i^2-2\sum_{i=1}^{N}F_iR_{SPi}+2\frac{\Delta I}{I}\sum_{i=1}^{N}G_iH_i+$$

$$2\frac{\Delta J}{J}\sum_{i=1}^{N}H_i^2-2\sum_{i=1}^{N}H_iR_{SSi}\bigg]=0. \tag{2.29}$$

These equations can be re-arranged in matrix form to give

$$\begin{pmatrix}\sum_{i=1}^{N}\left(A_i^2+C_i^2+E_i^2+G_i^2\right) & \sum_{i=1}^{N}(A_iB_i+C_iD_i+E_iF_i+G_iH_i)\\\sum_{i=1}^{N}(A_iB_i+C_iD_i+E_iF_i+G_iH_i) & \sum_{i=1}^{N}\left(B_i^2+D_i^2+F_i^2+H_i^2\right)\end{pmatrix}\begin{pmatrix}\frac{\Delta I}{I}\\\frac{\Delta J}{J}\end{pmatrix}=$$

$$\left(\begin{array}{c} \sum_{i=1}^{N}\left(A_i R_{pp_i} + C_i R_{PSi} + E_i R_{SPi} + G_i R_{SSi}\right) \\ \sum_{i=1}^{N}\left(B_i R_{ppi} + D_i R_{PSi} + F_i R_{SPi} + H_i R_{SSi}\right) \end{array}\right). \tag{2.30}$$

Taking the inverse of equation 2.30 is relatively simple and gives the result

$$\left(\begin{array}{c} \dfrac{\Delta I}{I} \\[4pt] \dfrac{\Delta J}{J} \end{array}\right) = \Omega \left(\begin{array}{c} \sum_{i=1}^{N}\left(B_i^2 + D_i^2 + F_i^2 + H_i^2\right)\sum_{i=1}^{N}\left(A_i R_{PPi} + C_i R_{PSi} + E_i R_{SPi} + G_i R_{SSi}\right) - \\ \sum_{i=1}^{N}\left(A_i^2 + C_i^2 + E_i^2 + G_i^2\right)\sum_{i=1}^{N}\left(B_i R_{PPi} + D_i R_{PSi} + F_i R_{SPi} + H_i R_{SSi}\right) - \\[10pt] \sum_{i=1}^{N}\left(A_i B_i + C_i D_i + E_i F_i + G_i H_i\right)\sum_{i=1}^{N}\left(B_i R_{PPi} + D_i R_{PSi} + F_i R_{SPi} + H_i R_{SSi}\right) \\ \sum_{i=1}^{N}\left(A_i B_i + C_i D_i + E_i F_i + G_i H_i\right)\sum_{i=1}^{N}\left(A_i R_{PPi} + C_i R_{PSi} + E_i R_{SPi} + G_i R_{SSi}\right) \end{array} \right) \tag{2.31}$$

where

$$\Omega = \dfrac{1}{\sum_{i=1}^{N}\left(A_i^2 + C_i^2 + E_i^2 + G_i^2\right)\sum_{i=1}^{N}\left(B_i^2 + D_i^2 + F_i^2 + H_i^2\right) - \left[\sum_{i=1}^{N}\left(A_i B_i + C_i D_i + E_i F_i + G_i H_i\right)\right]^2}. \tag{2.32}$$

Therefore, to simply examine the case of a P-P reflection, set all weights and reflectivities except A, B and R_{PP} to zero. Thus,

$$\frac{\Delta I}{I} = \frac{\sum_{i=1}^{N}B_i^2 \sum_{i=1}^{N}A_i R_{PP} - \sum_{i=1}^{N}A_i B_i \sum_{i=1}^{N}B_i R_{PPi}}{\sum_{i=1}^{N}A_i^2 \sum_{i=1}^{N}B_i^2 - \left[\sum_{i=1}^{N}A_i B_i\right]^2} \tag{2.33}$$

$$\frac{\Delta J}{J} = \frac{\sum_{i=1}^{N}A_i^2 \sum_{i=1}^{N}B_i R_{PP} - \sum_{i=1}^{N}A_i B_i \sum_{i=1}^{N}A_i R_{PPi}}{\sum_{i=1}^{N}A_i^2 \sum_{i=1}^{N}B_i^2 - \left[\sum_{i=1}^{N}A_i B_i\right]^2} \tag{2.34}$$

is equivalent to the form of Smith and Gidlow (1987). The summation of the weighted P-P reflectivity are simply weighted stacks which estimate $\Delta I/I$ and $\Delta J/J$.

In this study the focus is upon a method incorporating both P-P and P-S seismic data. Since the goal is to examine the effect each set of weights has upon each of the P-P

and P-S datasets it is reasonable to arrange the results as follows (after setting R_{SP} and R_{SS} and associated weights to zero)

$$\frac{\Delta I}{I} = \left(\frac{\sum\limits_{i=1}^{N} R_{PPi} A_i \sum\limits_{i=1}^{N}\left(B_i^2 + D_i^2\right) - \sum\limits_{i=1}^{N} R_{PPi} B_i \sum\limits_{i=1}^{N}\left(A_i B_i + C_i D_i\right)}{\sum\limits_{i=1}^{N}\left(A_i^2 + C_i^2\right)\sum\limits_{i=1}^{N}\left(B_i^2 + D_i^2\right) - \left[\sum\limits_{i=1}^{N}\left(A_i B_i + C_i D_i\right)\right]^2} + \right.$$

$$\left. \frac{\sum\limits_{i=1}^{N} R_{PSi} C_i \sum\limits_{i=1}^{N}\left(B_i^2 + D_i^2\right) - \sum\limits_{i=1}^{N} R_{PSi} D_i \sum\limits_{i=1}^{N}\left(A_i B_i + C_i D_i\right)}{\sum\limits_{i=1}^{N}\left(A_i^2 + C_i^2\right)\sum\limits_{i=1}^{N}\left(B_i^2 + D_i^2\right) - \left[\sum\limits_{i=1}^{N}\left(A_i B_i + C_i D_i\right)\right]^2} \right) \tag{2.35}$$

and

$$\frac{\Delta J}{J} = \left(\frac{\sum\limits_{i=1}^{N} R_{PPi} B_i \sum\limits_{i=1}^{N}\left(A_i^2 + C_i^2\right) - \sum\limits_{i=1}^{N} R_{PPi} A_i \sum\limits_{i=1}^{N}\left(A_i B_i + C_i D_i\right)}{\sum\limits_{i=1}^{N}\left(A_i^2 + C_i^2\right)\sum\limits_{i=1}^{N}\left(B_i^2 + D_i^2\right) - \left[\sum\limits_{i=1}^{N}\left(A_i B_i + C_i D_i\right)\right]^2} + \right.$$

$$\left. \frac{\sum\limits_{i=1}^{N} R_{PSi} D_i \sum\limits_{i=1}^{N}\left(A_i^2 + C_i^2\right) - \sum\limits_{i=1}^{N} R_{PSi} C_i \sum\limits_{i=1}^{N}\left(A_i B_i + C_i D_i\right)}{\sum\limits_{i=1}^{N}\left(A_i^2 + C_i^2\right)\sum\limits_{i=1}^{N}\left(B_i^2 + D_i^2\right) - \left[\sum\limits_{i=1}^{N}\left(A_i B_i + C_i D_i\right)\right]^2} \right). \tag{2.36}$$

The form of equations 2.35 and 2.36 are similar to the equations given by Stewart (1990) for $\Delta\alpha/\alpha$ and $\Delta\beta/\beta$.

It is possible to examine the weighting behavior for each of the P-P and P-S datasets as a function of offset. Notice the similarity in form of equations 2.35 and 2.36 with equations 2.33 and 2.34. Also notice the difference in the weighting of the P-P datasets in these same equations.

2.3.2 3-parameter P-P and P-S inversion

A number of authors have pointed out the potential benefit in deriving 3-parameter elastic estimates (e.g. Smith, 1996; Lines, 1998). These 3-parameter estimates

would represent either $\Delta\alpha/\alpha$, $\Delta\beta/\beta$ and $\Delta\rho/\rho$ or $\Delta I/I$, $\Delta J/J$ or $\Delta\rho/\rho$ elastic parameters. Drufuca and Mazzotti (1995) and Debski and Tarantola (1995) show the potential ambiguities inherent with the 3-parameter inversion of equation 2.3. Lines (1998) further shows that density determination is difficult for limited apertures (limited incidence angles) and typical seismic velocities. The application of P-S seismic data to this problem should further constrain the 3-parameter solution and thus allow for more reasonable acquisition parameters to be used.

The derivation of the 3-parameter inversion scheme is similar to that discussed in the previous section for the 2-parameter case. From equations 2.1, 2.2, 2.10 and 2.11 the following set of equations describe the first order Zoeppritz equation approximations of P-P, P-S, S-P and S-S reflectivity respectively.

$$R_{PP}(\theta) = a(\theta)\frac{\Delta\alpha}{\alpha} + b(\theta)\frac{\Delta\beta}{\beta} + c(\theta)\frac{\Delta\rho}{\rho} \tag{2.37}$$

$$R_{PS}(\theta,\varphi) = d(\theta,\varphi)\frac{\Delta\rho}{\rho} + e(\theta,\varphi)\frac{\Delta\beta}{\beta} \tag{2.38}$$

$$R_{SP}(\theta,\varphi) = f(\theta,\varphi)\frac{\Delta\rho}{\rho} + g(\theta,\varphi)\frac{\Delta\beta}{\beta} \tag{2.39}$$

$$R_{SS}(\varphi) = h(\varphi)\frac{\Delta\rho}{\rho} + i(\varphi)\frac{\Delta\beta}{\beta} \tag{2.40}$$

where

$$a(\theta) = \frac{1}{2\cos^2\theta} \tag{2.41}$$

$$b(\theta) = -4\frac{\beta^2}{\alpha^2}\sin^2\theta \tag{2.42}$$

$$c(\theta) = \frac{1}{2}\left(1 - 4\frac{\beta^2}{\alpha^2}\sin^2\theta\right) \tag{2.43}$$

$$d(\theta,\varphi) = \frac{-\alpha\tan\varphi}{2\beta}\left(1 - 2\sin^2\varphi + \frac{2\beta}{\alpha}\cos\theta\cos\varphi\right) \tag{2.44}$$

$$e(\theta,\varphi) = \frac{\alpha\tan\varphi}{\beta}\left(2\sin^2\varphi - \frac{2\beta}{\alpha}\cos\theta\cos\varphi\right) \tag{2.45}$$

$$f(\theta,\varphi) = \frac{-\sin\varphi}{2\cos\theta}\left(1 - 2\sin^2\varphi + 2\frac{\beta}{\alpha}\cos\theta\cos\varphi\right) \tag{2.46}$$

$$g(\theta,\varphi) = \frac{\sin\varphi}{\cos\theta}\left(2\sin^2\varphi - 2\frac{\beta}{\alpha}\cos\theta\cos\varphi\right) \tag{2.47}$$

$$h(\varphi) = -\frac{1}{10}\left(1 - 4\sin^2\varphi\right) \tag{2.48}$$

$$i(\varphi) = 4\sin^2\varphi - \frac{1}{2\cos^2\varphi} \tag{2.49}$$

Note the offset dependant weighting functions a through i are different than those described in equations 2.14, 2.15, 2.16 and 2.17.

Similar to equation 2.26, a mean-square error function ε, can be used to describe the error between observed reflectivity amplitude and the model curve. The function ε has the form:

$$\varepsilon = \sum_{i=1}^{N}\left[\left(R_{PPi} - a_i\frac{\Delta\alpha}{\alpha} - b_i\frac{\Delta\beta}{\beta} - c_i\frac{\Delta\rho}{\rho}\right)^2 + \left(R_{PSi} - d_i\frac{\Delta\rho}{\rho} - e_i\frac{\Delta\beta}{\beta}\right)^2 + \right.$$

$$\left. \left(R_{SPi} - f_i\frac{\Delta\rho}{\rho} - g_i\frac{\Delta\beta}{\beta}\right)^2 + \left(R_{SSi} - h_i\frac{\Delta\rho}{\rho} - i_i\frac{\Delta\beta}{\beta}\right)^2\right] \tag{2.50}$$

where N is the total number of offsets observed. Note ε will equal zero for an exact fit between the observed data and the derived model.

Now, taking the partial derivative of ε with respect to each of the elastic parameters $\Delta\alpha/\alpha$, $\Delta\beta/\beta$ and $\Delta\rho/\rho$ and setting the result equal to zero results in the following matrix equation.

$$\begin{pmatrix} \sum_{i=1}^{N} a_i^2 & \sum_{i=1}^{N} a_i b_i & \sum_{i=1}^{N} a_i c_i \\ \sum_{i=1}^{N} a_i b_i & \sum_{i=1}^{N}\left(b_i^2 + e_i^2 + g_i^2 + i_i^2\right) & \sum_{i=1}^{N}\left(b_i c_i + d_i e_i + f_i g_i + h_i i_i\right) \\ \sum_{i=1}^{N} a_i c_i & \sum_{i=1}^{N}\left(b_i c_i + d_i e_i + f_i g_i + h_i i_i\right) & \sum_{i=1}^{N}\left(c_i^2 + d_i^2 + f_i^2 + h_i^2\right) \end{pmatrix}\begin{pmatrix}\Delta\alpha/\alpha \\ \Delta\beta/\beta \\ \Delta\rho/\rho\end{pmatrix} =$$

$$\begin{pmatrix} \sum\limits_{i=1}^{N} a_i R_{PPi} \\ \sum\limits_{i=1}^{N} \left(b_i R_{PPi} + e_i R_{PSi} + g_i R_{SPi} + i_i R_{SSi} \right) \\ \sum\limits_{i=1}^{N} \left(c_i R_{PPi} + d_i R_{PSi} + f_i R_{SPi} + h_i R_{SSi} \right) \end{pmatrix} \tag{2.51}$$

The solution to equation 2.51 can be solved analytically in the same manner as equations 2.30 and 2.31 or can be solved numerically in matrix form. Equation 2.51 can be solved in matrix form using a method discussed in section 2.4.2. To analytically solve equation 2.51, a simple relation can be used to invert the weighting matrix. Let equation 2.51 be written as

$$Ax = b, \ x = A^{-1}b. \tag{2.52}$$

Solving for x in equation 2.52 gives

$$x = \frac{1}{|A|} \begin{pmatrix} \begin{vmatrix} a_{22} & a_{23} \\ a_{32} & a_{33} \end{vmatrix} & \begin{vmatrix} a_{13} & a_{12} \\ a_{33} & a_{32} \end{vmatrix} & \begin{vmatrix} a_{12} & a_{13} \\ a_{22} & a_{23} \end{vmatrix} \\ \begin{vmatrix} a_{23} & a_{21} \\ a_{33} & a_{31} \end{vmatrix} & \begin{vmatrix} a_{11} & a_{13} \\ a_{31} & a_{33} \end{vmatrix} & \begin{vmatrix} a_{13} & a_{11} \\ a_{23} & a_{21} \end{vmatrix} \\ \begin{vmatrix} a_{21} & a_{22} \\ a_{31} & a_{32} \end{vmatrix} & \begin{vmatrix} a_{12} & a_{11} \\ a_{32} & a_{31} \end{vmatrix} & \begin{vmatrix} a_{11} & a_{12} \\ a_{21} & a_{22} \end{vmatrix} \end{pmatrix} b \tag{2.53}$$

$$\text{where, } |A| = a_{11} \begin{vmatrix} a_{22} & a_{23} \\ a_{32} & a_{33} \end{vmatrix} - a_{12} \begin{vmatrix} a_{21} & a_{23} \\ a_{31} & a_{33} \end{vmatrix} + a_{13} \begin{vmatrix} a_{21} & a_{22} \\ a_{31} & a_{32} \end{vmatrix} =$$

$$a_{11}(a_{22}a_{33} - a_{32}a_{23}) - a_{12}(a_{21}a_{33} - a_{31}a_{23}) + a_{13}(a_{21}a_{32} - a_{21}a_{32}) \tag{2.54}$$

which is valid for all cases where the determinant of A is non-zero. The full solution to equation 2.53 in terms of the coefficients in equation 2.51 is algebraically complex and unstable, therefore will not be included in this study.

In order to examine the case of a simultaneous P-P and P-S inversion, set the weights f, g, h, i, R_{SPi} and R_{SSi} in equation 2.51 to zero. Thus, for the case of a 3-parameter, simultaneous P-P and P-S inversion, the solution to equation 2.53 can be written as

$$\frac{\Delta\alpha}{\alpha} = \frac{\begin{vmatrix} a_{22} & a_{23} \\ a_{32} & a_{33} \end{vmatrix} \sum_{i=1}^{N} a_i R_{PPi} + \begin{vmatrix} a_{13} & a_{12} \\ a_{33} & a_{32} \end{vmatrix} \sum_{i=1}^{N} (b_i R_{PPi} + e_i R_{PSi}) + \begin{vmatrix} a_{12} & a_{13} \\ a_{22} & a_{23} \end{vmatrix} \sum_{i=1}^{N} (c_i R_{PPi} + d_i R_{PSi})}{|A|}$$

(2.55)

$$\frac{\Delta\beta}{\beta} = \frac{\begin{vmatrix} a_{23} & a_{21} \\ a_{33} & a_{31} \end{vmatrix} \sum_{i=1}^{N} a_i R_{PPi} + \begin{vmatrix} a_{11} & a_{13} \\ a_{31} & a_{33} \end{vmatrix} \sum_{i=1}^{N} (b_i R_{PPi} + e_i R_{PSi}) + \begin{vmatrix} a_{13} & a_{11} \\ a_{23} & a_{21} \end{vmatrix} \sum_{i=1}^{N} (c_i R_{PPi} + d_i R_{PSi})}{|A|}$$

(2.56)

$$\frac{\Delta\rho}{\rho} = \frac{\begin{vmatrix} a_{21} & a_{22} \\ a_{31} & a_{32} \end{vmatrix} \sum_{i=1}^{N} a_i R_{PPi} + \begin{vmatrix} a_{12} & a_{11} \\ a_{32} & a_{31} \end{vmatrix} \sum_{i=1}^{N} (b_i R_{PPi} + e_i R_{PSi}) + \begin{vmatrix} a_{11} & a_{12} \\ a_{21} & a_{22} \end{vmatrix} \sum_{i=1}^{N} (c_i R_{PPi} + d_i R_{PSi})}{|A|}$$

(2.57)

where

$$\begin{vmatrix} a_{22} & a_{23} \\ a_{32} & a_{33} \end{vmatrix} = \sum_{i=1}^{N} (b_i^2 + e_i^2) \sum_{i=1}^{N} (c_i^2 + d_i^2) - \left[\sum_{i=1}^{N} (b_i c_i + d_i e_i) \right]^2$$

(2.58)

$$\begin{vmatrix} a_{13} & a_{12} \\ a_{33} & a_{32} \end{vmatrix} = \begin{vmatrix} a_{23} & a_{21} \\ a_{33} & a_{31} \end{vmatrix} = \sum_{i=1}^{N} a_i c_i \sum_{i=1}^{N} (b_i c_i + d_i e_i) - \sum_{i=1}^{N} a_i b_i \sum_{i=1}^{N} (c_i^2 + d_i^2)$$

(2.59)

$$\begin{vmatrix} a_{12} & a_{13} \\ a_{22} & a_{23} \end{vmatrix} = \begin{vmatrix} a_{21} & a_{22} \\ a_{31} & a_{32} \end{vmatrix} = \sum_{i=1}^{N} a_i b_i \sum_{i=1}^{N} (b_i c_i + d_i e_i) - \sum_{i=1}^{N} a_i c_i \sum_{i=1}^{N} (b_i^2 + e_i^2)$$

(2.60)

$$\begin{vmatrix} a_{11} & a_{13} \\ a_{31} & a_{33} \end{vmatrix} = \sum_{i=1}^{N} a_i^2 \sum_{i=1}^{N} (c_i^2 + d_i^2) - \left[\sum_{i=1}^{N} a_i c_i \right]^2$$

(2.61)

$$\begin{vmatrix} a_{13} & a_{11} \\ a_{23} & a_{21} \end{vmatrix} = \begin{vmatrix} a_{12} & a_{11} \\ a_{32} & a_{31} \end{vmatrix} = \sum_{i=1}^{N} a_i c_i \sum_{i=1}^{N} a_i b_i - \sum_{i=1}^{N} a_i^2 \sum_{i=1}^{N} (b_i c_i + d_i e_i)$$

(2.62)

$$\begin{vmatrix} a_{11} & a_{12} \\ a_{21} & a_{22} \end{vmatrix} = \sum_{i=1}^{N} a_i^2 \sum_{i=1}^{N} (b_i c_i + d_i e_i) - \left[\sum_{i=1}^{N} a_i b_i \right]^2$$

(2.63)

$$|A| = \sum_{i=1}^{N} a_i^2 \begin{vmatrix} a_{22} & a_{23} \\ a_{32} & a_{33} \end{vmatrix} + \sum_{i=1}^{N} a_i b_i \begin{vmatrix} a_{23} & a_{21} \\ a_{33} & a_{31} \end{vmatrix} + \sum_{i=1}^{N} a_i c_i \begin{vmatrix} a_{21} & a_{22} \\ a_{31} & a_{32} \end{vmatrix}.$$

(2.64)

This method can also be modified for the case where R_{PP} is a function of I, J and ρ, and R_{PS}, R_{SP} and R_{SS} are functions of J and ρ. Note this method does not assume an empirical

relationship between density and P-wave velocity and thus, has the potential to improve inversion accuracy. The incorporation of P-S seismic data should provide a more stable inverse of equation 2.51 since a second set of independent observations (P-S reflectivities) is included in the inversion.

2.3.3 Improving petrophysical discrimination

A number of derived attributes may be used to highlight changes in lithology and pore fluid content. Smith and Gidlow (1987) discuss two possibilities, the pseudo-Poisson's ratio reflectivity and the fluid factor reflectivity. These attributes can be directly calculated from estimates of $\Delta\alpha/\alpha$ and $\Delta\beta/\beta$, or $\Delta I/I$ and $\Delta J/J$. The pseudo-Poisson's ratio reflectivity or fractional Vp/Vs ratio is given by

$$\frac{\Delta q}{q} \equiv \frac{\Delta(\alpha/\beta)}{\alpha/\beta} = \frac{\Delta(I/J)}{I/J} = \frac{\Delta\alpha}{\alpha} - \frac{\Delta\beta}{\beta} = \frac{\Delta I}{I} - \frac{\Delta J}{J}. \tag{2.65}$$

Equation 2.65 allows the calculation of normalized changes in Vp/Vs ratios, which can be directly correlated to lithological and/or pore fluid content changes.

The fluid factor reflectivity is highly dependent upon local geology and measures deviations from the 'mudrock line' of Castagna et al. (1985). The fluid factor is generally considered accurate for water saturated clastic sedimentary rocks, but deviates significantly for gas-saturated clastics, carbonates and igneous rocks. The 'mudrock line' is an empirical relation between α and β thought to typify shales. It is given by Castagna et al. (1985) as

$$\alpha \approx a + b\beta = 1360 + 1.16\beta \text{ (velocities in m/s)}. \tag{2.66}$$

For a given locality, a and b should be derived from well-constrained, dipole sonic log information. The derivation of the 'fluid factor reflectivity' from equation 2.66 is straightforward, if we let g equal the deviation from the mudrock line

$$\text{i.e. } g = \alpha - a - b\beta. \tag{2.67}$$

Note the parameter g will be zero for exact adherence to the 'mudrock line' of equation 2.66. Now, the finite difference of equation (2.67),

$$\Delta g = \Delta\alpha - b\Delta\beta \tag{2.68}$$

and define the fluid factor Δf, as

$$\Delta f = \frac{\Delta g}{\alpha} = \left(\frac{\Delta \alpha}{\alpha} - b\frac{\Delta \beta}{\alpha} \right) = \left(\frac{\Delta \alpha}{\alpha} - b\frac{\beta}{\alpha}\frac{\Delta \beta}{\beta} \right) = \left[\frac{\Delta I}{I} - b\frac{\beta}{\alpha}\frac{\Delta J}{J} - \frac{\Delta \rho}{\rho}\left(1 - b\frac{\beta}{\alpha} \right) \right]. \quad (2.69)$$

Therefore any deviations from the fluid factor indicate a deviation from the 'mudrock line' (equation 2.68). The potentially awkward step of calculating estimates of $\Delta \rho / \rho$ in equation 2.69 above generally limits the use of the fluid factor reflectivity when inverting for compressional and shear impedance.

Several authors have alluded to the need for greater physical insight into the underlying physical rock properties contained in compressional and shear velocities (Wright 1984, Thomsen, 1990, Castagna et al., 1993). From these observations it is sensible to conclude the possible utility of extracting rigidity and shear modulus rock properties directly from AVO analysis. Stewart (1995) provides a method for directly extracting elastic modulus parameters from the Zoeppritz equation approximations of Aki and Richards (1980). Stewart further advised that λ / μ may be used to highlight pore-fluid contrasts rather than changes in lithology. This concept was successfully tested by Goodway et al. (1997) to show the potential of improved petrophysical discrimination using Lame parameters ($\lambda \rho$, $\mu \rho$ and λ / μ). This method is summarized by the following set of equations:

$$\frac{\Delta(\lambda \rho)}{\lambda \rho} = \frac{2}{\alpha^2 - 2\beta^2}\left(\alpha^2 \frac{\Delta I}{I} - 2\beta^2 \frac{\Delta J}{J} \right) \quad (2.70)$$

$$\frac{\Delta(\mu \rho)}{\mu \rho} = 2\frac{\Delta J}{J} \quad (2.71)$$

$$\frac{\Delta(\lambda / \mu)}{(\lambda / \mu)} = \frac{2\alpha^2}{\alpha^2 - 2\beta^2}\left(\frac{\Delta I}{I} - \frac{\Delta J}{J} \right) = \frac{2\alpha^2}{\alpha^2 - 2\beta^2}\frac{\Delta q}{q} \quad (2.72)$$

For completeness, the fractional Poisson ratio and bulk modulus ratios can also be defined:

$$\frac{\Delta \sigma}{\sigma} = \frac{2\alpha^2 \beta^2}{(\alpha^2 - \beta^2)(\alpha^2 - 2\beta^2)}\left(\frac{\Delta I}{I} - \frac{\Delta J}{J} \right) = \frac{2\alpha^2 \beta^2}{(\alpha^2 - \beta^2)(\alpha^2 - 2\beta^2)}\frac{\Delta q}{q} \quad (2.73)$$

$$\frac{\Delta(\kappa\rho)}{\kappa\rho} = \frac{2}{\alpha^2 - (4/3)\beta^2}\left(\alpha^2\frac{\Delta I}{I} - \frac{4}{3}\beta^2\frac{\Delta J}{J}\right)$$ (2.74)

Note equations 2.70, 2.71, 2.72, 2.73 and 2.74 represent weighted functions of the previously derived estimates of $\Delta I/I$ and $\Delta J/J$. In practice, the smoothed background model provides the weights.

Alternatively, equations 2.3 and 2.4 can be re-defined in terms of $\lambda\rho$ and $\mu\rho$:

$$R_{PP}(\theta) \approx \left[\frac{(\alpha^2 - 2\beta^2)}{4\alpha^2\cos^2\theta}\right]\frac{\Delta(\lambda\rho)}{\lambda\rho} - \frac{\beta^2}{\alpha^2}\left(\frac{1}{4\cos^2\theta} - 2\sin^2\theta\right)\frac{\Delta(\mu\rho)}{\mu\rho} -$$

$$\left[\frac{1}{2}\tan^2\theta - 2\frac{\beta^2}{\alpha^2}\sin^2\theta\right]\frac{\Delta\rho}{\rho}$$ (2.75)

$$R_{PS}(\theta) \approx \frac{-\alpha\tan\varphi}{2\beta}\left[\left(1 + \frac{2\beta^2}{\alpha^2}\sin^2\theta - \frac{2\beta}{\alpha}\cos\theta\cos\varphi\right)\frac{\Delta\rho}{\rho} - \right.$$

$$\left.\left(\frac{2\beta^2}{\alpha^2}\sin^2\theta - \frac{2\beta}{\alpha}\cos\theta\cos\varphi\right)\frac{\Delta(\mu\rho)}{\mu\rho}\right]$$ (2.76)

For the 3-parameter inversion case, equations 2.75 and 2.76 can be used as-is. Again, the $\Delta\rho/\rho$ term in equation 2.75 can be neglected for limited offset apertures. The $\Delta\rho/\rho$ term in equation 2.76 can either be neglected (valid for small incidence angles and β/α of 0.5), or can be written as a function of $\Delta\lambda\rho/\lambda\rho$ and $\Delta\mu\rho/\mu\rho$ using equation 2.7:

$$\frac{\Delta\rho}{\rho} = \frac{1}{5}\frac{(\alpha^2 - 2\beta^2)}{2\alpha^2}\frac{\Delta(\lambda\rho)}{\lambda\rho} + \frac{1}{5}\frac{\beta^2}{\alpha^2}\frac{\Delta(\mu\rho)}{\mu\rho}$$ (2.77)

2.4 Simultaneous non-linear P-P and P-S inversion

The ultimate goal of an AVO inversion method is to find the elastic parameters input to the Zoeppritz equations. To attain this goal in all settings, it is necessary to use non-linear inversion methods. For completeness, these non-linear methods are briefly discussed, but will not be investigated further in this study. A number of authors have discussed the use of these non-linear inversion methods for pre-stack P-wave seismic data (e.g. Macdonald et al., 1987; Russell, 1988). The goal in this study is to apply these P-wave methods to a simultaneous P-P and P-S non-linear inversion technique and compare

the result with the linearized case. The application of non-linear methods is more difficult due to the non-linear dependence between elastic parameter contrasts and reflectivity compared with the linearized case. In order to justify these non-linear methods, it is necessary to investigate both the linearity and the uniqueness of the inversion method in question. If it is found that both the linearity and uniqueness of the inversion method are sufficient, a simultaneous non-linear P-P and P-S method may be considered possible.

2.4.1 Simultaneous P-P and P-S inversion using the GLI method

Generalized Linear Inversion (GLI) has been applied extensively in the solution of AVO inversion problems, i.e. Macdonald et al. (1987), Russell (1988), De Haas and Berkhout (1988) and Demirbag and Çoruh (1988). Since the Zoeppritz equations are non-linear functions with respect to the input parameters, the linearization (or approximation) of the Zoeppritz equations introduces error. As a result, the linearity and uniqueness of a solution to a given inverse problem is dependent upon the selection of the parameters to be inverted. The selection of these invertable parameters (the model parameter vector), as well as the suitability of the nonlinear function for linearization must be examined prior to applying an inversion method (Demirbag et al., 1993). In the case of AVO inversion, the inverse problem is to find the elastic parameters given source-receiver offsets, zero-offset two-way traveltime and the pre-stack seismic gathers. Since densities in the Zoeppritz equations appear in the form of ratios, the following parameter vector was chosen:

$$P = (\alpha_1, \beta_1, \alpha_2, \beta_2, \rho_2/\rho_1).$$
(2.78)

Following Macdonald et al. (1987) and Menke (1989) the linearity and uniqueness of the inversion of the Zoeppritz equations by the GLI method is tested using Residual Function Maps (RFMs). The residual error function is given as follows:

$$\varepsilon_1(x, y) = \sum_{i=1}^{N} \left[R_{PPi} - R_{PPi}^*(x, y)\right]^2$$
(2.79)

where R_{PPi} is the forward model response for a given set of elastic parameters (the P-P reflection coefficient Zoeppritz equation solution), and $R_{PPi}^*(x,y)$ is the response of the same function to different values of the chosen input parameter pair (x,y). Equation 2.79

is evaluated for all offsets from 1 to N, where N is the total number offsets. This method was tested and compared using P-P, and both P-P and P-S reflectivities. Thus for the case of a simultaneous analysis of P-P and P-S reflectivity, equation 2.79 becomes:

$$\varepsilon_2(x,y) = \sum_{i=1}^{N}\left[R_{PPi} - R_{PPi}^*(x,y)\right]^2 + \sum_{i=1}^{N}\left[R_{PSi} - R_{PSi}^*(x,y)\right]^2 \qquad (2.80)$$

where R_{PSi} is the forward model response for a given set of elastic parameters (the P-S Zoeppritz equations solution), and $R_{PSi}^*(x,y)$ is the response of the same function to different values of the chosen input parameter pair (x,y).

As observed by Demirbag et al. (1993), RFMs are used to investigate the degree of linearity in non-linear functions around a large neighborhood of chosen model parameters. A linear function results in RFMs that show closed contours around their true parameters. In the non-linear case, if the RFMs show closed contours with a single minima, then the non-linear function can be successfully inverted using the GLI scheme with a two-term Taylor series expansion (Lines and Treitel, 1984). The following set of model parameters was used to test the appropriateness of this simultaneous inversion scheme:

Layer	α (m/s)	β (m/s)	ρ (g/cc)
1	3000	1500	2.294
2	4000	2000	2.465

Table 2.2: Sample elastic parameters used to construct the Residual Function Maps in figure 2.3.

Incidence angles for P-P and P-S reflections were calculated assuming an interface at 2000m depth. Offsets in this test were calculated in intervals of 100m from a minimum of 0 to a maximum of 4000m. Thus for the case of a P-P reflection, the maximum angle of incidence equals 45 degrees, while for a P-S reflection the maximum angle of incidence equals 57 degrees. The results of these RFMs are given in figure 2.3.
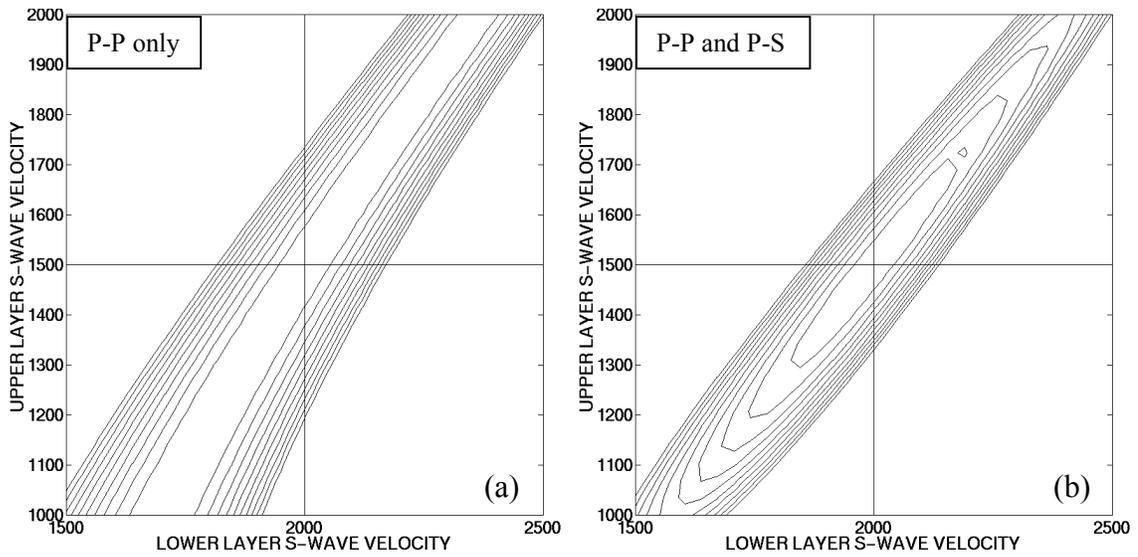
Figure 2.3 (a,b): Residual function maps for P-P (left) and both P-P and P-S reflectivity (right) investigating the linear dependence between upper layer shear velocity and lower layer shear velocity. Exact values denoted by crossing hair. Contour values range from 0.005 to 0.05 in steps of .005.
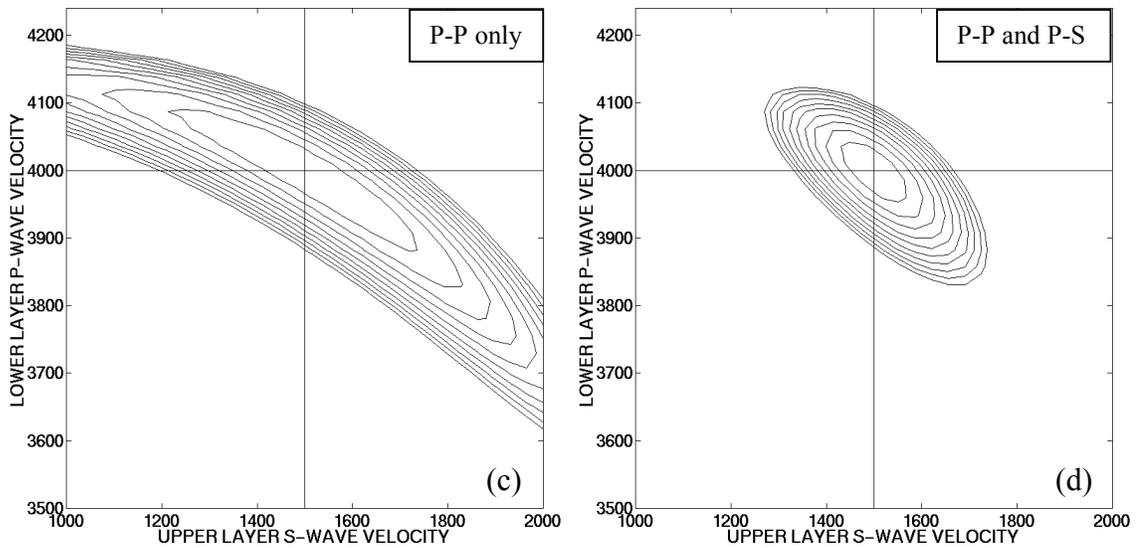
Figure 2.3 (c,d): Residual function maps for P-P (left) and both P-P and P-S reflectivity (right) investigating the linear dependence between lower layer compressional velocity and upper layer shear velocity. Exact values denoted by crossing hair. Contour values range from 0.005 to 0.05 in steps of .005.
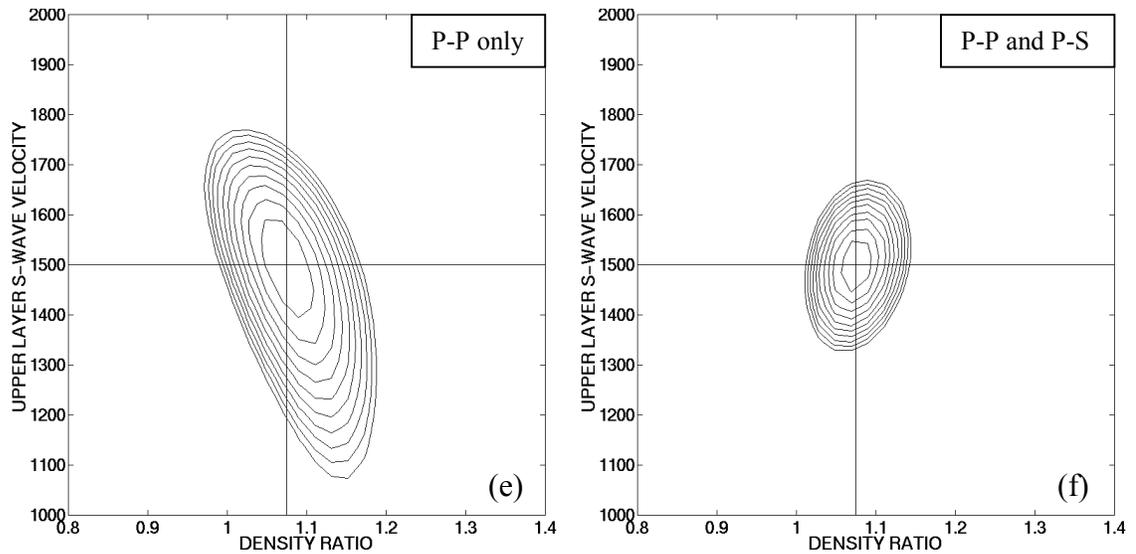
Figure 2.3 (e,f): Residual function maps for P-P (left) and both P-P and P-S reflectivity (right) investigating the linear dependence between upper layer shear velocity and the ratio of lower layer density and upper layer density. Exact values denoted by crossing hair. Contour values range from 0.005 to 0.05 in steps of .005.
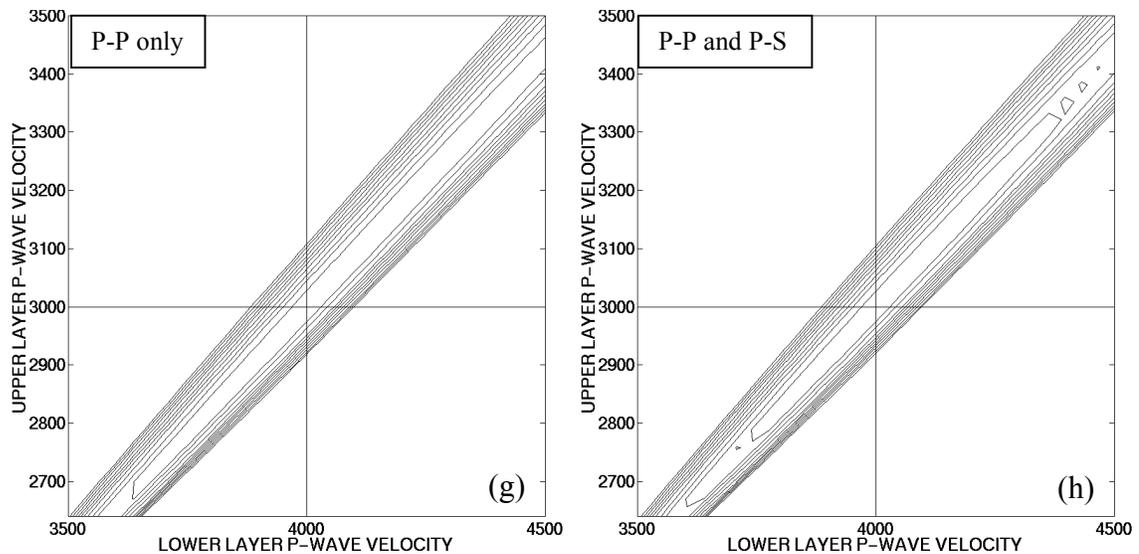
Figure 2.3 (g,h): Residual function maps for P-P (left) and both P-P and P-S reflectivity (right) investigating the linear dependence between upper layer compressional velocity and lower layer compressional velocity. Exact values denoted by crossing hair. Contour values range from 0.005 to 0.05 in steps of .005.
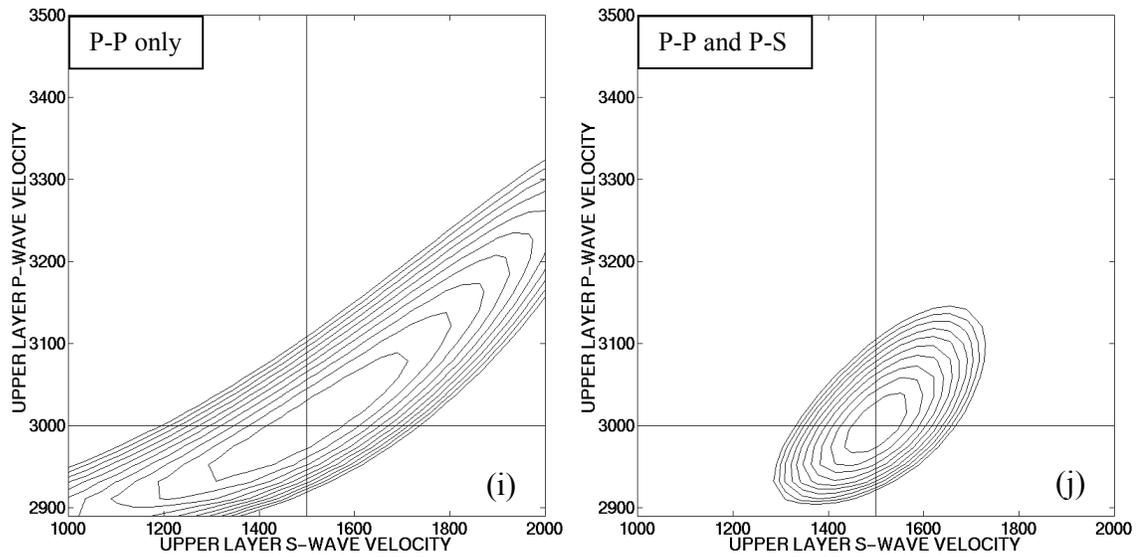
Figure 2.3 (i,j): Residual function maps for P-P (left) and both P-P and P-S reflectivity (right) investigating the linear dependence between upper layer compressional velocity and upper layer shear velocity. Exact values denoted by crossing hair. Contour values range from 0.005 to 0.05 in steps of .005.
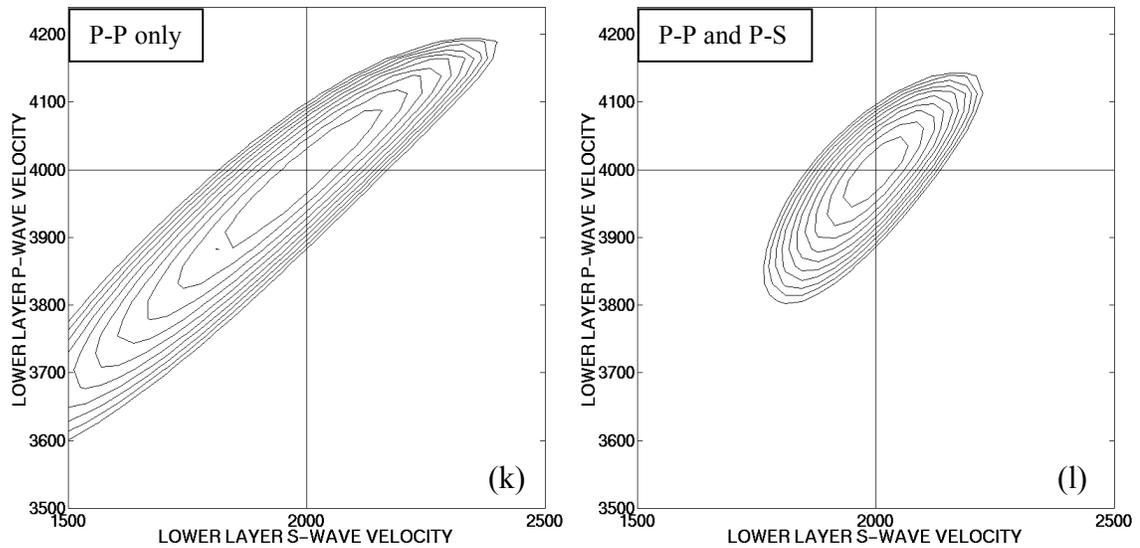
Figure 2.3 (k,l): Residual function maps for P-P (left) and both P-P and P-S reflectivity (right) investigating the linear dependence between lower layer compressional velocity and lower layer shear velocity. Exact values denoted by crossing hair. Contour values range from 0.005 to 0.05 in steps of .005.
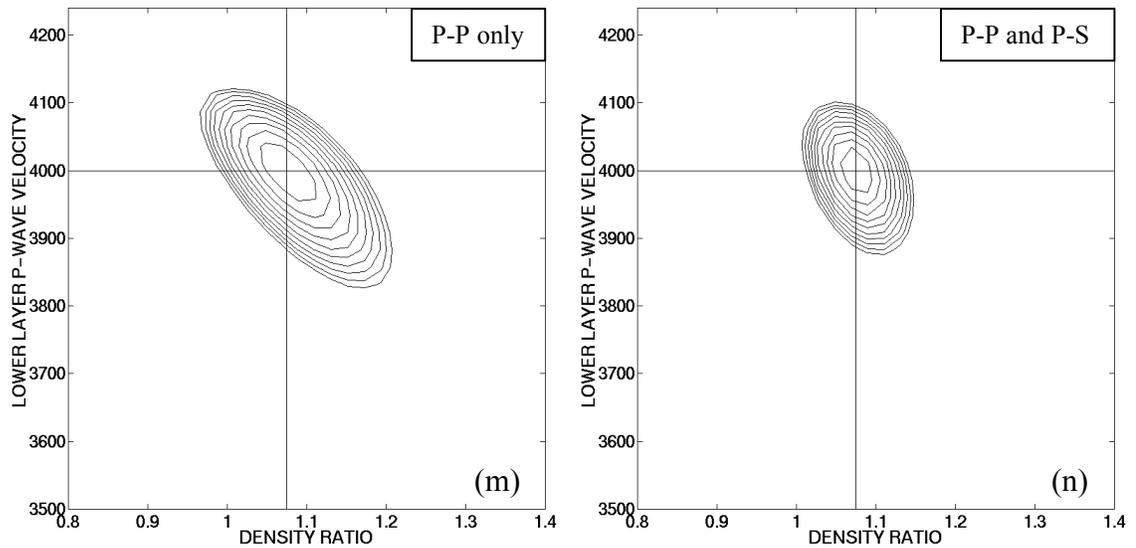
Figure 2.3 (m,n): Residual function maps for P-P (left) and both P-P and P-S reflectivity (right) investigating the linear dependence between lower layer compressional velocity and the ratio of lower layer density and upper layer density . Exact values denoted by crossing hair. Contour values range from 0.005 to 0.05 in steps of .005.
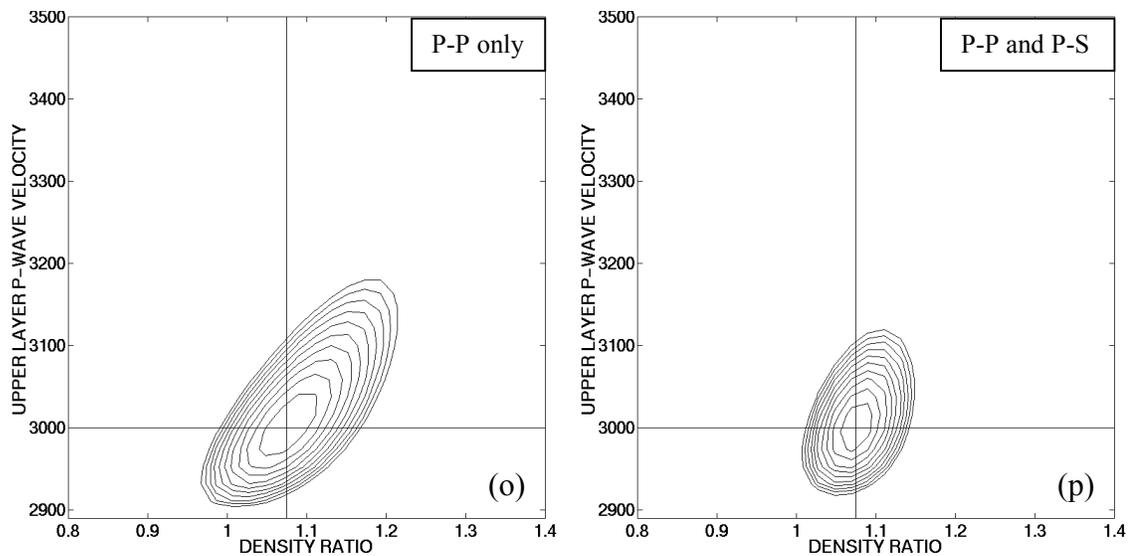

Figure 2.3 (o,p): Residual function maps for P-P (left) and both P-P and P-S reflectivity (right) investigating the linear dependence between lower layer compressional velocity and the ratio of lower layer density and upper layer density . Exact values denoted by crossing hair. Contour values range from 0.005 to 0.05 in steps of .005.
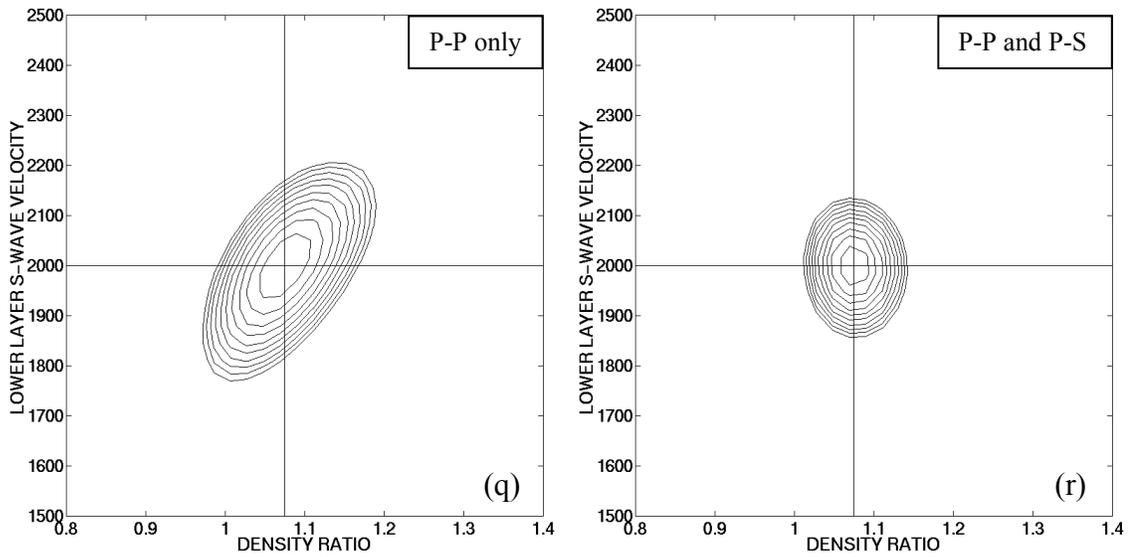
Figure 2.3 (q,r): Residual function maps for P-P (left) and both P-P and P-S reflectivity (right) investigating the linear dependence between lower layer shear velocity and the ratio of lower layer density and upper layer density . Exact values denoted by crossing hair. Contour values range from 0.005 to 0.05 in steps of .005.
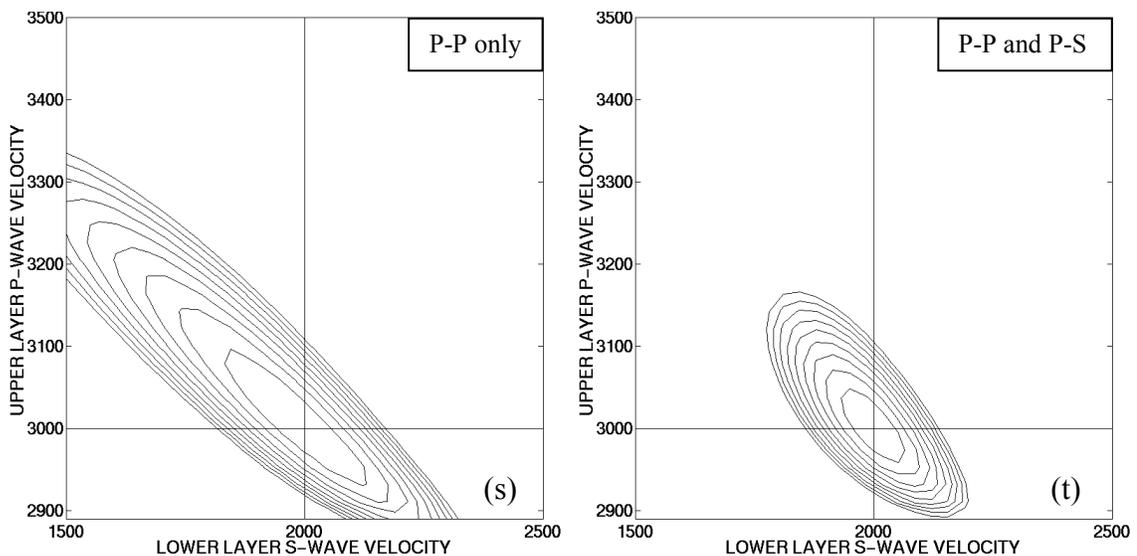
Figure 2.3 (s,t): Residual function maps for P-P (left) and both P-P and P-S reflectivity (right) investigating the linear dependence between upper layer compressional velocity and lower layer shear velocity. Exact values denoted by crossing hair. Contour values range from 0.005 to 0.05 in steps of .005.

Notice in the case of the S-wave velocity pair in figure 2.3(a) a poorly defined minima is observed. This indicates a poor degree of linearity between β_1 and β_2, thus a potentially poor result if the GLI method is used. Using both P-P and P-S seismic data for the same S-wave velocity pair (figure 2.3b) indicates a local minima with closed contours and thus, a well constrained, linear solution. For all cases examined, the inclusion of P-S reflectivities decreases the size of the contours and thus decreases the ambiguity of the inversion result. From these observations, it may be concluded that the GLI method is valid for the simultaneous P-P and P-S inversion case using the numerical values given in table 2.2.

2.4.2 Derivation of non-linear simultaneous inversion equations

Given a forward model represented by a function f, Lines and Treitel (1984) show this function can be expanded into a truncated Taylor series expansion around $P = P_o$, where P_o is the initial parameter vector. This expanded Taylor series has the form

$$f(P,X) = f(P_o,X) + (P - P_o)\frac{\partial f(P,X)}{\partial P}\bigg|_{Po,X} \qquad (2.81)$$

where X is an unchanged set of parameters input into the function f.

This concept can be applied in an iterative sense to create updates for a given model compared to the observed data $f(P_o,X)$. In this way a model perturbation can be obtained given a set of observed data and an intial model. In the case of inverting the Zoeppritz equations, equation 2.81 can be written as a multi-dimensional truncated Taylor series of the form

$$R_M(\alpha + \Delta\alpha, \beta + \Delta\beta, \rho + \Delta\rho) = R_M(\alpha,\beta,\rho) + \frac{\partial R_M(\alpha,\beta,\rho)}{\partial\alpha}\Delta\alpha + \frac{\partial R_M(\alpha,\beta,\rho)}{\partial\beta}\Delta\beta +$$

$$+ \frac{\partial R_M(\alpha,\beta,\rho)}{\partial\rho}\Delta\rho + ... \qquad (2.82)$$

where $R_M(\alpha+d\alpha,\beta+d\beta,\rho+d\rho)$ is the measured data, $R_M(\alpha,\beta,\rho)$ is the computed reflection coefficient from the current model.

$\frac{\partial R_M(\alpha,\beta,\rho)}{\partial\alpha}$, $\frac{\partial R_M(\alpha,\beta,\rho)}{\partial\beta}$ and $\frac{\partial R_M(\alpha,\beta,\rho)}{\partial\rho}$ are the partial derivatives of the model

with respect to α, β, ρ. The parameters $\Delta\alpha$, $\Delta\beta$ and $\Delta\rho$ are the desired updates of the current model. R_M can represent R_{PP}, R_{PS} or any other mode at a given interface. For the case of a simultaneous P-P and P-S inversion equation 2.82 can be written in matrix form as:

$$Ax = R \ or \ \begin{pmatrix} {}_1R_{PP,\alpha} & {}_1R_{PP,\beta} & {}_1R_{PP,\rho} \\ {}_2R_{PP,\alpha} & {}_2R_{PP,\beta} & {}_2R_{PP,\rho} \\ \vdots & \vdots & \vdots \\ {}_NR_{PP,\alpha} & {}_NR_{PP,\beta} & {}_NR_{PP,\rho} \\ {}_1R_{PS,\alpha} & {}_1R_{PS,\beta} & {}_1R_{PS,\rho} \\ {}_2R_{PS,\alpha} & {}_2R_{PS,\beta} & {}_2R_{PS,\rho} \\ \vdots & \vdots & \vdots \\ {}_NR_{PS,\alpha} & {}_NR_{PS,\beta} & {}_NR_{PS,\rho} \end{pmatrix}_{2Nx3} \begin{pmatrix} \Delta\alpha \\ \Delta\beta \\ \Delta\rho \end{pmatrix}_{3x1} = \begin{pmatrix} \delta R_{PP(1)} \\ \delta R_{PP(2)} \\ \vdots \\ \delta R_{PP(N)} \\ \delta R_{PS(1)} \\ \delta R_{PS(2)} \\ \vdots \\ \delta R_{PS(N)} \end{pmatrix}_{2Nx1} . \qquad (2.83)$$

Where δR_{PP} and δR_{PS} represent the difference between the computed and observed values of Rpp and Rps respectively. N represents the total number of offsets in each of the P-P and P-S offset gathers. The least squares inverse of equation 2.82 is

$$x = \left(A^T A\right)^{-1} A^T R . \qquad (2.83)$$

Here matrix x represents the desired updates of the model, matrix A represents the Jacobian matrix of the partial derivatives of the Zoeppritz equations with respect to the initial model and R represents the difference between the observed and calculated model. The values in matrix A can either be calculated numerically or can be obtained analytically by differentiating the Zoeppritz equations directly. Computing these derivatives analytically is difficult due to the algebraically complex nature of the Zoeppritz equations. The primary difficulty with equation 2.83 is the possibility of an unstable inverse. This degree of instability or singularity can be examined using a Singular Value Decomposition (SVD) of the matrix A (Lines and Treitel, 1984). The SVD allows a stable, generalized inverse to be formed which estimates only those parameters that are well constrained by the data. A second method of increasing the stability of the inverse is to apply a damped least-squares minimization method, the Levenberg-Marquardt method. Equation 2.84 can be modified as the following

$$x = \left(A^T A + \eta I\right)^{-1} A^T R . \tag{2.85}$$

Where η is a Lagrange multiplier and I is a 3x3 identity matrix.

It should be now possible to create an iterative procedure to minimize the set of updates calculated in matrix x. This procedure will start with an initial guess model provided by the user. At each iteration, smaller values for each of the updates in matrix x should be obtained. Once a convergent solution is obtained to within a given set of tolerances, the model data should approximately equal the observed data. Once the model and the observed data are equal, the input elastic parameters of the model are known. Since the input parameters of the forward model can be non-unique (i.e. one set of input elastic parameters can give the exact same solution as a completely different set of elastic parameters), the solution should be subject to some user-defined constraints. These constraints should represent an acceptable range of density, P-wave and S-wave velocities for input to the forward model (Zoeppritz equations).

2.5 Chapter Summary

A basic error analysis for the P-P and P-S Zoeppritz equation approximations of Aki and Richards was constructed. It was shown the P-S reflectivity approximation is generally less accurate than the P-P approximation. The Zoeppritz equation approximations for P-P and P-S reflectivity were then modified to appear as functions of compressional and shear impedance values. This modification it has been shown results in relatively small error. Next, a method for the simultaneous 2-parameter least-squares inversion of P-P, P-S, S-P and S-S reflectivity was constructed. This method was extended to the case of a 3-parameter inversion. Several methods for improving the discrimination of lithology and pore fluid content were then discussed by modifying these elastic parameter estimates obtained by inversion. Next, a Generalized Linear Inversion method was constructed to simultaneously invert the exact Zoeppritz equation solution for P-P and P-S reflectivity.

CHAPTER 3

Simultaneous inversion testing

3.1 Introduction

The performance of the linearized, simultaneous inversion algorithm for P-P and P-S data as described in chapter 2, is tested for both a single layer and a multi-layer 1-D elastic model, and compared to a standard method utilizing P-P seismic data only. As shown in chapter 2, the equations describing the weighted stacks for the P-P and the simultaneous P-P and P-S inversion methods result in very different weighting behaviors. The difference between these weighting methods is analyzed in some detail for a simple single layer case. Several tests are then performed to measure the accuracy of assumptions made in applying the simultaneous inversion method. Next, a simple test is performed to compare the performance of the simultaneous inversion method to a standard P-P method in the presence of noisy data. Finally, the simultaneous inversion method is compared to a standard P-P inversion method using both noise-free and noisy synthetic, multi-offset seismic data.

3.2 Weighting behavior as a function of offset

A comparison can be made between the offset-dependant weights applied in the case of a P-P and a simultaneous P-P and P-S weighted stack. This comparison will show

a significant difference between these methods and describe the potential benefit of incorporating a simultaneous inversion method. In this study, a simple four-layered earth model is constructed with the same set of incidence angles for each layer. This study is performed using the direct Zoeppritz equation reflectivity solutions, and does not take into account effects such as frequency bandwidth or wavelet effects such as tuning. The density, compressional and shear velocities are summarized in figure 3.1. For each layer, weights were calculated assuming a range of incidence angles from 0 to 40 degrees (all incidence angles are less than critical incidence). Note: for the case of a P-S reflection, the incidence angles are greater than for the P-P case given the same source-receiver offsets. P-P and P-S reflectivity curves are given for each interface in figures 3.2, 3.3 and 3.4.

$$\frac{\Delta I}{I} = -0.0639, \frac{\Delta J}{J} = 0.0362, \frac{\Delta q}{q} = -0.1001$$

$$\frac{\Delta I}{I} = 0.1250, \frac{\Delta J}{J} = 0.1159, \frac{\Delta q}{q} = 0.0091$$

$$\frac{\Delta I}{I} = 0.3779, \frac{\Delta J}{J} = 0.6449, \frac{\Delta q}{q} = -0.1867$$
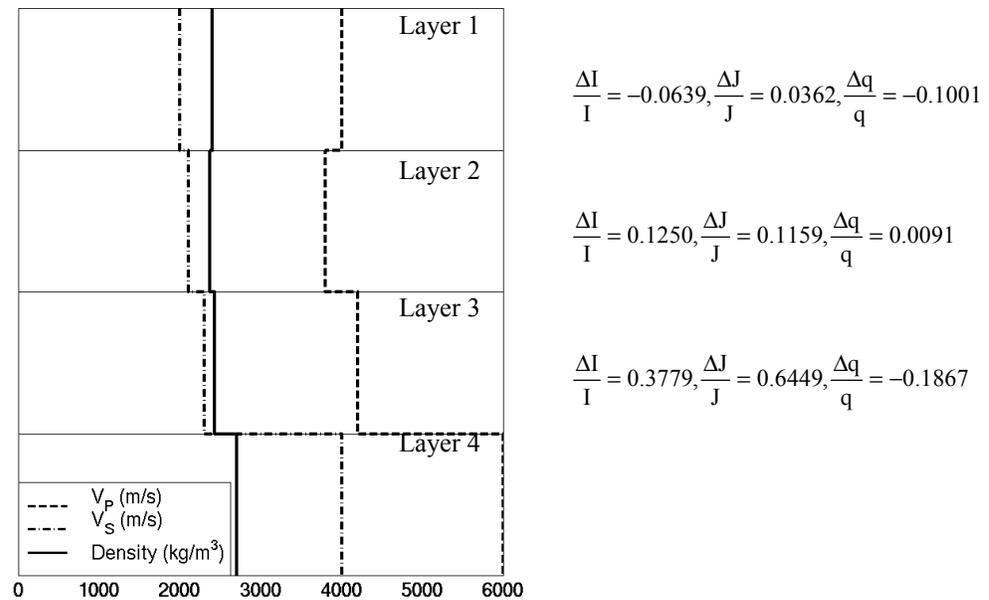
Figure 3.1: V_P, V_S and density values for a 4-layered earth model. Depths are not included since a full range of incidence angles is assumed at each interface.
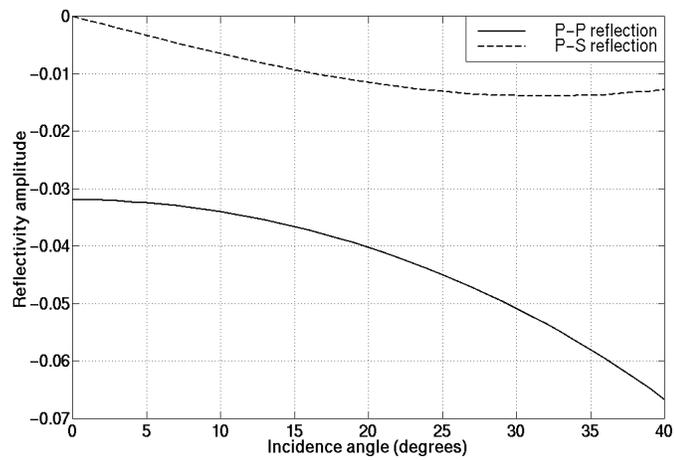
Figure 3.2: P-P and P-S reflectivity amplitudes at the layer 1-2 interface for a range of incidence angles from 0 to 40 degrees.
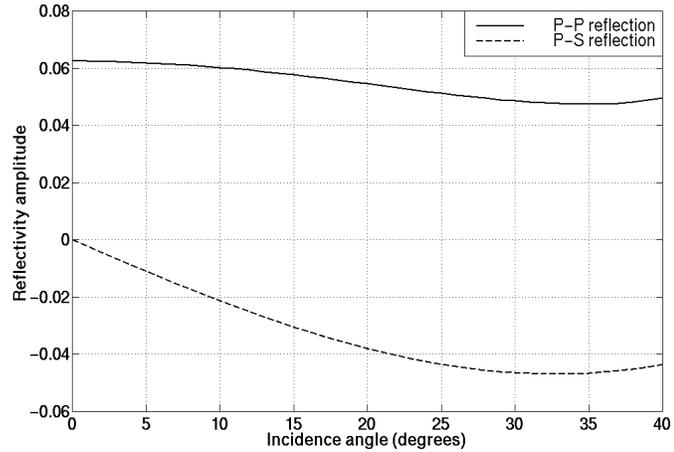
Figure 3.3: P-P and P-S reflectivity amplitudes at the layer 2-3 interface for a range of incidence angles from 0 to 40 degrees.
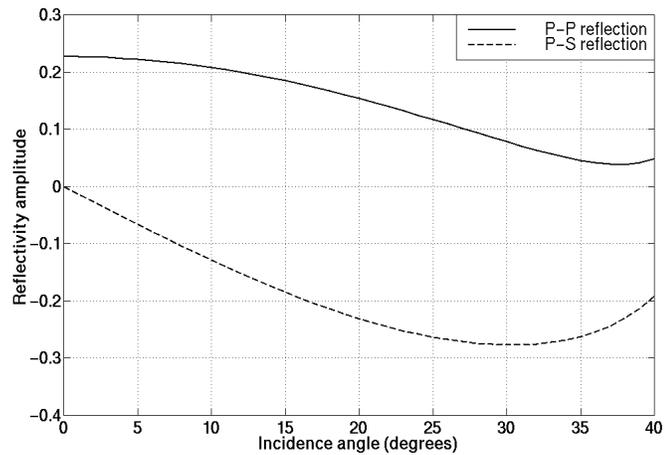
Figure 3.4: P-P and P-S reflectivity amplitudes at the layer 3-4 interface for a range of incidence angles from 0 to 40 degrees.

3.2.1 2-parameter inversion for compressional and shear impedance

The inversion of equations 2.27 and 2.28 is relatively straightforward. Given a known set of incidence angles and highly smoothed values of V_P and V_S on either side of a welded elastic interface, a set of offset-dependant weights can be generated. In order to generate these weights, average values of V_P and V_S were calculated for each interface. Next, average angles of reflection-transmission (θ, P-P reflection) and reflection-transmission (φ, P-S reflection) are calculated using Snell's law. The values of $A(\theta)$, $B(\theta)$, $C(\theta,\varphi)$ and $D(\theta,\varphi)$ in equations 2.14 and 2.15 can now be obtained and applied to equations 2.27 and 2.28. It is now possible to examine the effect each of these sets of weights has on the P-P and P-S datasets for each method in question. These weights appear as follows for the simultaneous inversion case

$$\frac{\Delta I}{I} = W_{PP\frac{\Delta I}{I}}(\theta_{PP},\varphi_{PP})R_{PP}(\theta_{PP}) + W_{PS\frac{\Delta I}{I}}(\theta_{PS},\varphi_{PS})R_{PS}(\theta_{PS}), \qquad (3.1)$$

$$\frac{\Delta J}{J} = W_{PP\frac{\Delta J}{J}}(\theta_{PP},\varphi_{PP})R_{PP}(\theta_{PP}) + W_{PS\frac{\Delta J}{j}}(\theta_{PS},\varphi_{PS})R_{PS}(\theta_{PS}). \qquad (3.2)$$

Where W_{PP} and W_{PS} represents the weights in equations 2.27 and 2.28, R_{PP} and R_{PS} represent the observed reflectivity and $\Delta I/I$ and $\Delta J/J$ represent the desired elastic parameters to be inverted. Note the angles θ and φ are different for P-P and P-S reflections given the same set of source-receiver offsets.

For the case of a P-P inversion only, W_{PS} and R_{PS} are zero and W_{PP} is calculated according to either equation 2.25 or 2.26 for $\Delta I/I$ or $\Delta J/J$ respectively. In the case of this study each set of weights was calculated assuming a range of offsets from 0 to 2000m in intervals of 40m with a reflector depth at 1500m. The behavior of these weights for P-P alone and P-P and P-S simultaneous as a function of offset is shown in figures 3.5 to 3.7 for the elastic constants given in figure 3.1.
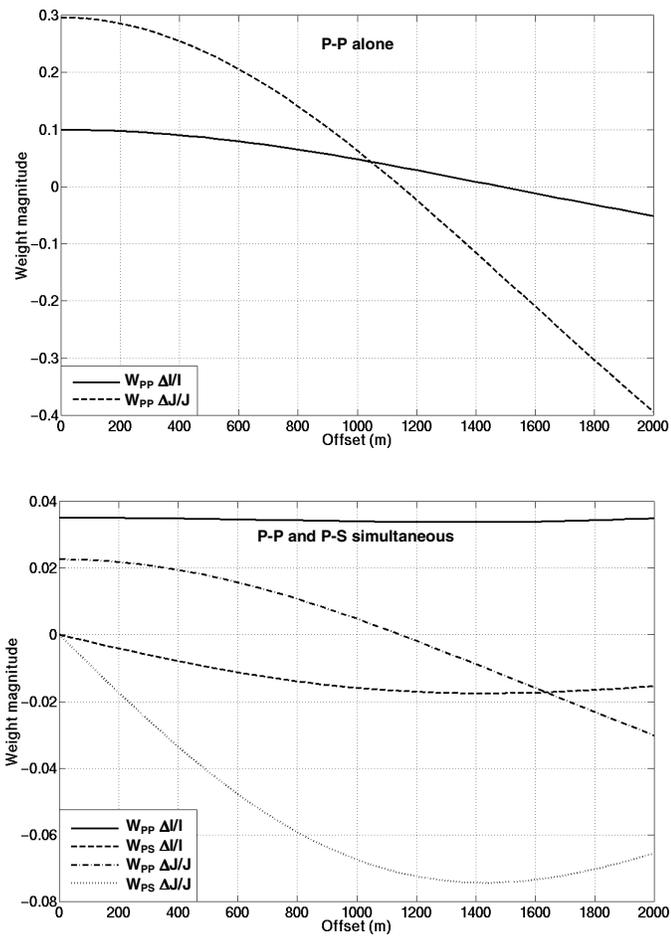
Figure 3.5: Weights applied to R_{PP} at the layer 1-2 interface using equations 2.25 and 2.26 (upper). Weights applied to R_{PP} and R_{PS} at the layer 1-2 interface using equations 2.27 and 2.28 (lower).
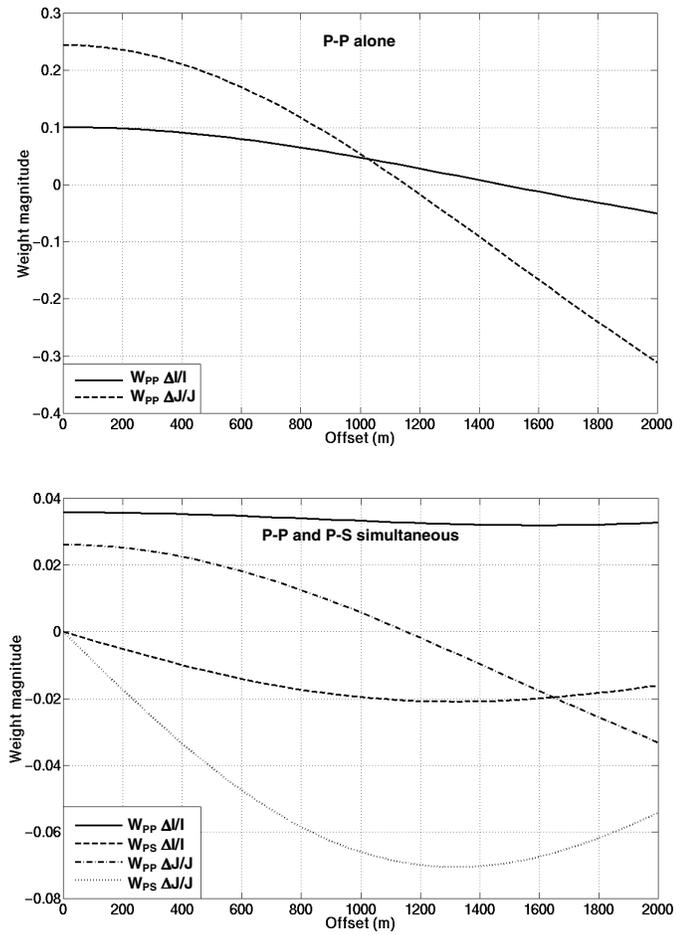
Figure 3.6: Weights applied to R_{PP} at the layer 2-3 interface using equations 2.25 and 2.26 (upper). Weights applied to R_{PP} and R_{PS} at the layer 2-3 interface using equations 2.27 and 2.28 (lower).
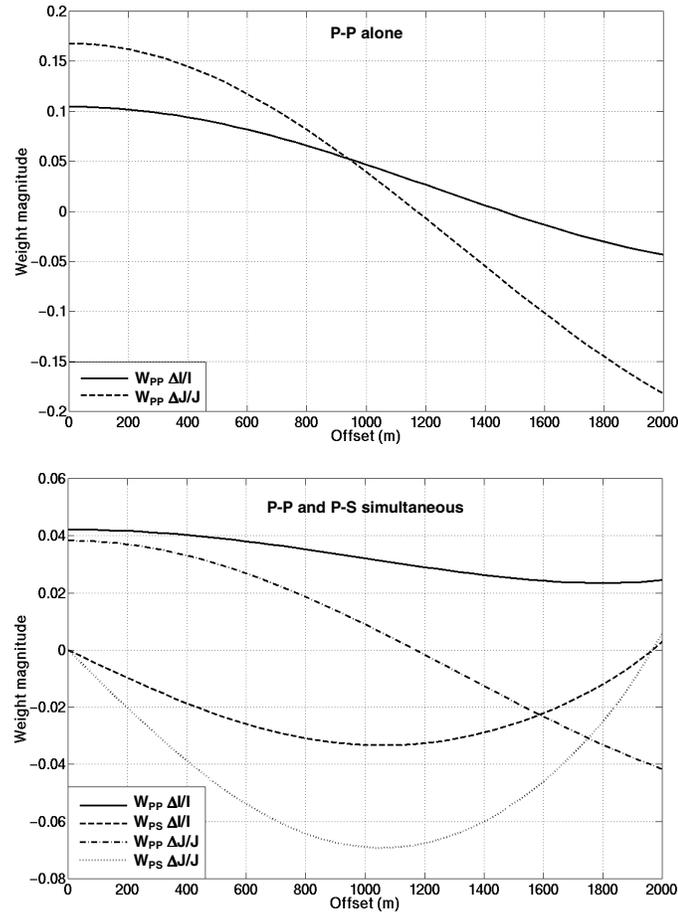
Figure 3.7: Weights applied to R_{PP} at the layer 3-4 interface using equations 2.25 and 2.26 (upper). Weights applied to R_{PP} and R_{PS} at the layer 3-4 interface using equations 2.27 and 2.28 (lower).

Note in figures 3.5 to 3.7, W_{PP} $\Delta I/I$ represents the R_{PP} weight resulting in $\Delta I/I$, W_{PS} $\Delta I/I$ represents the R_{PS} weight resulting in $\Delta I/I$, W_{PP} $\Delta J/J$ represents the R_{PP} weight resulting in $\Delta J/J$ and W_{PS} $\Delta J/J$ represents the R_{PS} weight resulting in the estimate of $\Delta J/J$.

Several key observations can be made from these figures. The magnitude of the weights for the P-P only inversion is higher than for the simultaneous P-P and P-S inversion method. This is likely due to the increased data fold and more even weighting behavior observed using the simultaneous inversion method. The weights for the P-S datasets are zero at zero offset as expected. The P-P inversion weights for $\Delta I/I$ and $\Delta J/J$

often change sign with increasing offset. This effect tends to cancel middle offsets and weight the far and near offsets more heavily. This explains the common practice of differencing the far and near offsets of a given P-P offset gather as an indicator of an AVO anomaly. Since only the near and far offsets are included in the weighted stack, the fold of the overall $\Delta I/I$ section is lower. This worsens the signal-to-noise ratio of the $\Delta I/I$ and $\Delta J/J$ stacks using the P-P weighted stacking method.

The weighting of the P-P dataset for the $\Delta I/I$ stack using the simultaneous inversion method tends to apply each offset more evenly. This effect in addition to doubling the data fold of each $\Delta I/I$ stack results in an improvement in the signal-to-noise of the $\Delta I/I$ inversion result. Figures 3.5 to 3.7 show the W_{PS} $\Delta I/I$ weight is generally smaller than the W_{PP} $\Delta I/I$ weight. Since R_{PP} is larger in magnitude than R_{PS} and the R_{PP} weight is generally larger than the I-R_{PP} weight, the effect the W_{PS} $\Delta I/I$ weight has on the estimate of $\Delta I/I$ is relatively small.

The W_{PS} $\Delta J/J$ weights are generally larger than the W_{PP} $\Delta J/J$ weights. This effect highlights the greater dependance changes in $\Delta J/J$ have on R_{PS} compared with R_{PP}. Again, it can be observed that W_{PP} $\Delta J/J$ tends to change sign with increasing offset using the P-P weighted stacking method. It can also be observed the W_{PP} $\Delta J/J$ weight tends to change sign with increasing offset using the simultaneous inversion method. The W_{PS} $\Delta J/J$ weights generally are at maximum magnitude at middle offset and thus weight the middle offset of the R_{PS} dataset more heavily. This compensates for the low W_{PP} $\Delta J/J$ weights in the middle.

3.3 Simultaneous inversion accuracy

As noted in section 2.2, the linearization of the Zoeppritz equations (Zoeppritz equation approximations) introduces error into the final inversion result. It was shown that these errors may be significant, especially in the case of the P-S reflection coefficient. However, these approximations were shown to be relatively accurate for small elastic parameter contrasts and small incidence angles. In an effort to examine the

effect of this error on the inversion result, several simple two-layer earth models were constructed. In this case, 3 different, 2-layer models were examined using the elastic parameters in figure 3.1. P-P and P-S reflection events were raytraced assuming a single source and multiple receivers located at the surface, with a reflector depth at 1500m. Incidence angles were calculated for surface offsets from 0 to 2000m at intervals of 40m for a total of 51 possible incidence angles for each of the P-P and P-S reflections. Incidence angles for each 2-layered earth model ranged from approximately 0 to 34 degrees for the P-P reflection event and from 0 to 44 degrees for the P-S reflection event. In the next set of accuracy tests, error was calculated using both a Zoeppritz equation approximation and a true Zoeppritz equation solution to calculate the forward set of P-P and P-S reflection coefficients. This error function is written as follows:

$$\% \text{ error} = \frac{\left.\dfrac{\Delta(I, J \text{ or } q)}{(I, J \text{ or } q)}\right|_{\text{CALCULATED}} - \left.\dfrac{\Delta(I, J \text{ or } q)}{(I, J \text{ or } q)}\right|_{\text{TRUE}}}{\left.\dfrac{\Delta(I, J \text{ or } q)}{(I, J \text{ or } q)}\right|_{\text{TRUE}}} \times 100 \tag{3.3}$$

where $\dfrac{\Delta(I, J \text{ or } q)}{(I, J \text{ or } q)}$ represents estimates of $\dfrac{\Delta I}{I}, \dfrac{\Delta J}{J}$ or $\dfrac{\Delta q}{q}$ using the P-P or the simultaneous P-P and P-S inversion methods.

3.3.1 Matrix inversion error

Ideally, using the Zoeppritz equation approximations for the forward model should enable the approximate inversion to exactly recover estimates of $\Delta I/I$, $\Delta J/J$ and $\Delta q/q$. Error in this case is due to the inversion of the weighting-matrix in equation 2.22. To examine this error, the Singular Value Decomposition (SVD) of the matrix to be inverted can be obtained (Lines and Treitel, 1984). In the case of a square matrix, the SVD of matrix A^{-1} can be written as:

$$A^{-1} = V \cdot \left[\text{diag}(1/w_j)\right] \cdot U^T \tag{3.4}$$

where U and V are square, orthogonal matrices such that their inverses are equal to their transposes, and the $(1/w_j)$ term is a square, diagonal matrix with elements represented by $1/w_j$, where w_j are the singular values of A. If any value of w_j equals zero, the inverse of matrix A can be said to be singular or unstable. The degree of instability for the inverse

of martix A can be examined using the condition number of matrix A^{-1}. The condition number of matrix A^{-1} is defined as the ratio of the largest (in magnitude) of the w_j's to the smallest of the w_j's. In all cases tested, the condition number of the weighting-matrix in equation 2.22 was smaller for the simultaneous P-P and P-S inversion method than for the P-P inversion method. This should result in more accurate inversion results using the simultaneous inversion method. Table 3.1 shows the condition number obtained from the inversion of the forward model using the elastic parameters given in figure 3.1.

	Condition number	
	P-P inversion method	Simultaneous inversion
Layer 1-2 interface	47.09	3.75
Layer 2-3 interface	34.97	3.96
Layer 3-4 interface	22.81	5.68

Table 3.1: Condition numbers obtained from the inversion of a forward model using the elastic parameters given in figure 3.1. In all cases the condition number of matrix A^{-1} is smaller using the simultaneous inversion method indicating a more stable inverse.

Several two-layered earth models were constructed to test the errors caused by matrix instability. This error was calculated for each interface by comparing inversion accuracy using the Zoeppritz equation approximations as the forward model and comparing the inversion results using this forward model with the exact fractional elastic parameters at each interface. The inversion accuracy for these models is summarized in figures 3.8, 3.9 and 3.10.
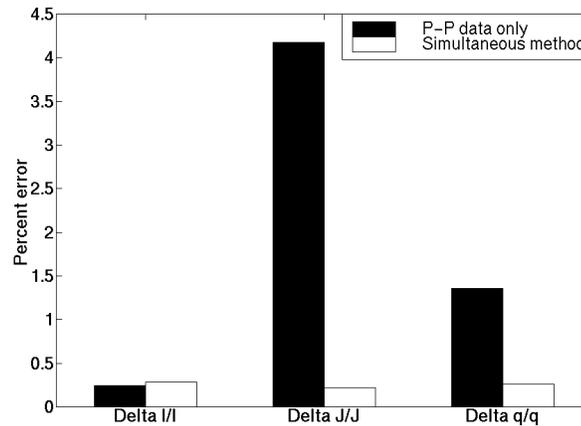
Figure 3.8: Percent error between the inversion result using the Zoeppritz equation approximations and the true fractional elastic parameters ($\Delta I/I$, $\Delta J/J$ and $\Delta q/q$) at the layer 1-2 interface. Notice the more accurate results obtained using the simultaneous inversion method. The larger error in the $\Delta I/I$ estimate for the simultaneous inversion method is due to a deviation in the relationship between density and compressional impedance given in equation 2.7.
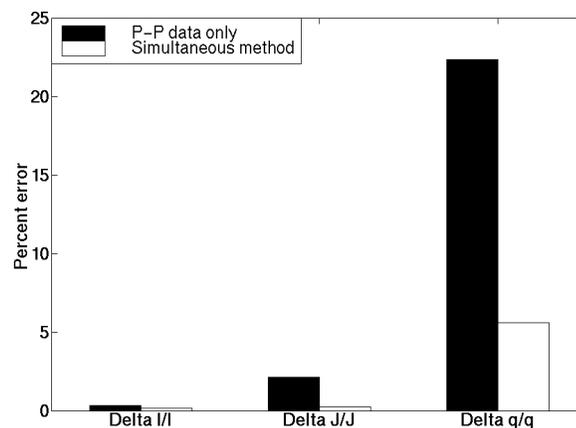
Figure 3.9: Percent error between the inversion result using the Zoeppritz equation approximations and the true fractional elastic parameters ($\Delta I/I$, $\Delta J/J$ and $\Delta q/q$) at the layer 2-3 interface. The large error observed in the $\Delta q/q$ estimate is due to the large effect that small changes have on percent error calculations for small magnitudes of the inversion result and the exact solution. In this case density and compressional impedance are related by the equation given in equation 2.7.
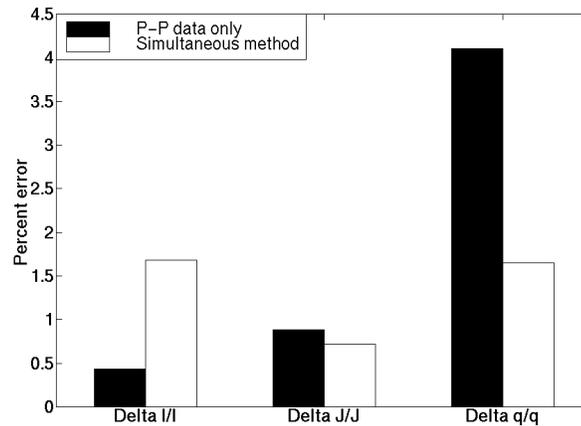
Figure 3.10: Percent error between the inversion result using the Zoeppritz equation approximations and the true fractional elastic parameters ($\Delta I/I$, $\Delta J/J$ and $\Delta q/q$) at the layer 3-4 interface. The larger error in the $\Delta I/I$ estimate for the simultaneous inversion method is due to a deviation in the relationship between density and compressional impedance given in equation 2.7.

The simultaneous inversion method shows improved inversion accuracy in most cases. The larger error in the $\Delta I/I$ estimate in figures 3.8 and 3.10 is due to a deviation in the relation between $\Delta\rho/\rho$ and $\Delta I/I$ given in equation 2.7, i.e. in each case $\Delta I/I$ does not equal $4\Delta\rho/\rho$. The simultaneous inversion method is more sensitive to a poor fit between P-wave velocity and density resulting in the larger error for the $\Delta I/I$ estimate in figure 3.10. This effect is due to the greater dependence upon the $\Delta\rho/\rho$ vs. $\Delta I/I$ relation for the P-S reflection coefficient in the simultaneous inversion method. The elastic parameters in figure 3.9 exactly correspond to the relation given in equation 2.7. The large error in the $\Delta q/q$ estimates in figure 3.9 is due to the relatively small value of $\Delta q/q$ calculated and the subsequent large effect small changes have on equation 3.3.

3.3.2 Zoeppritz equation approximation error

A second set of tests was conducted to examine the effect of the Zoeppritz equation approximations on the inversion result. In this case, the forward P-P and P-S reflection coefficients were calculated using the true Zoeppritz equations. Since both P-P

and simultaneous inversion methods utilize the Zoeppritz equation approximations for the inversion, there should be a discrepancy between the forward model and the inversion result. Testing the discrepancy between the forward model and the inversion result also must contain similar matrix inversion errors as discussed in the previous section.

The same two-layer earth models were used as in the previous section to test the accuracy of the Zoeppritz equation approximations. The inversion accuracy for these models are summarized in figures 3.11, 3.12 and 3.13 below.
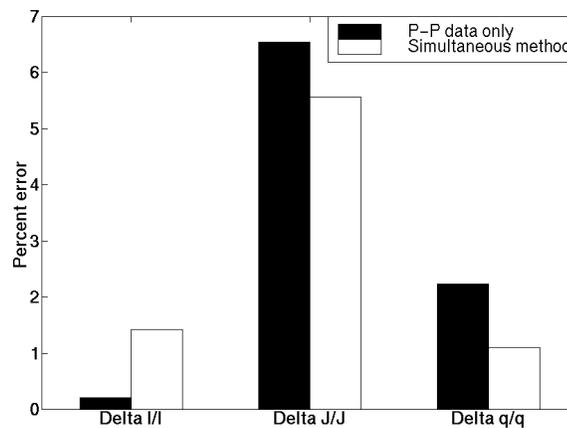
Figure 3.11: Percent error between the inversion result using the Zoeppritz equations for the forward model and the true fractional elastic parameters ($\Delta I/I$, $\Delta J/J$ and $\Delta q/q$) at the layer 1-2 interface.
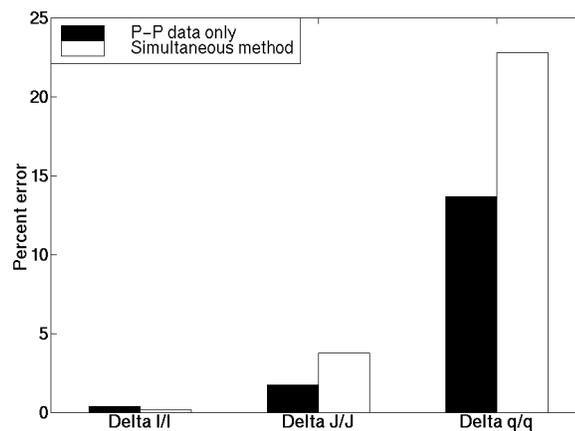
Figure 3.12: Percent error between the inversion result using the Zoeppritz equations for the forward model and the true fractional elastic parameters ($\Delta I/I$, $\Delta J/J$ and $\Delta q/q$) at the

layer 2-3 interface. The large error observed in the $\Delta q/q$ estimate is due to the small magnitude of the forward model and the inversion result for the $\Delta q/q$ parameter.
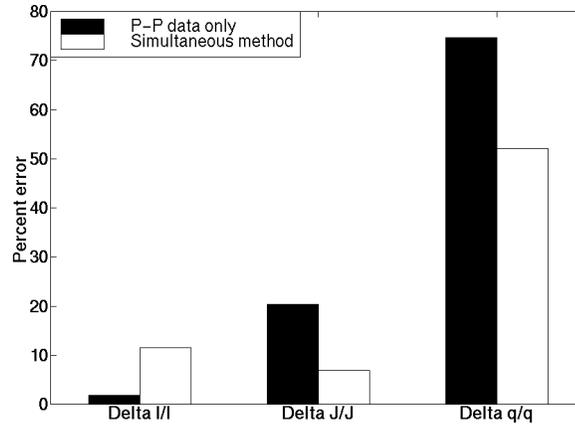

Figure 3.13: Percent error between the inversion result using the Zoeppritz equations for the forward model and the true fractional elastic parameters ($\Delta I/I$, $\Delta J/J$ and $\Delta q/q$) at the layer 3-4 interface. The increase in error of the $\Delta I/I$ estimate using the simultaneous inversion method is due to error in the relation between $\Delta \rho/\rho$ and $\Delta I/I$ given in equation 2.7.

Figure 3.11 generally shows an accuracy improvement using the simultaneous inversion method. Both methods give comparable results for the same set of observed elastic parameter contrasts. Figure 3.12 gives comparably accurate results for both methods. Since $\Delta q/q$ is nearly zero, small changes in $\Delta q/q$ give rise to large error percentages. Figure 3.13 represents an earth model with relatively large elastic contrasts, thus violating the assumptions made in both the P-P and P-S Zoeppritz equation approximations. Errors are subsequently quite large for the inversion results at the layer 3-4 interface. These results show that some care must be taken while applying inversion methods utilizing the Zoeppritz equation approximations. As a result, both inversion methods should be used with caution where large incidence angles and large changes in elastic parameters are expected.

3.4 Simultaneous inversion accuracy in the presence of noise

Any given seismic recording will contain some amount of noise in relation to the desired signal. Inversion accuracy is highly dependent upon the amount of noise present. A number of seismic processing techniques have been developed to suppress noise. Among the most effective to date has been the process of stacking or averaging seismic traces over a range of offsets. In a standard stacking procedure, each offset in a given NMO corrected CMP or CCP gather is equally weighted then averaged resulting in a 'zero offset section'. A general rule for noise suppression is that the signal-to-noise ratio improves by a factor approximately equal to the square root of the data fold (number of source-receiver offsets). Since a simultaneous P-P and P-S inversion method includes twice as many reflectivity observations, it is reasonable to assume a corresponding improvement in signal-to-noise should be obtained. The weights applied to each offset also greatly affect the ability of a weighted stacking method to suppress noise. As shown in section 3.2 the simultaneous inversion method generally applies weights more evenly with offset. In the case of the P-P inversion method, weights from a given offset gather tend to remove middle offsets and only weight near and far offsets resulting in relatively poor noise suppression.

In order to examine the effect noise has upon inversion accuracy, several models were constructed using the elastic parameters in figure 3.1. The forward model signal was calculated using the exact Zoeppritz equations and a user-input level of noise was then added to the result (signal). This noise was generated in the time-domain using a zero-mean algorithm with noise values distributed normally about the input signal (reflection coefficient series). This algorithm bases the noise level upon a user input signal-to-noise ratio and the root mean squared (RMS) power of the input signal (P-P or P-S reflection coefficient series). In the case of this study, 51 offsets contribute to each of the P-P and P-S offset gathers. The results of these tests are given below in figures 3.14, 3.15, 3.16, 3.17 and 3.18.
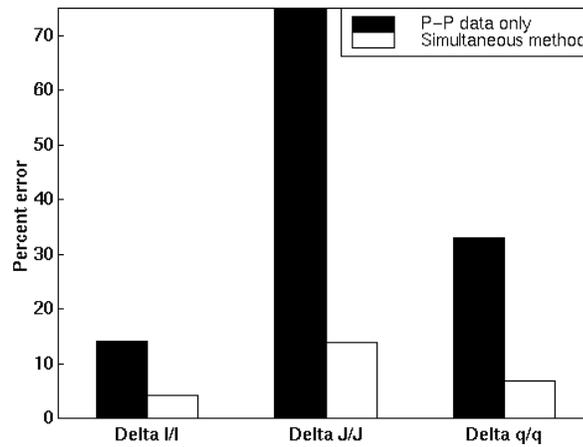
Figure 3.14: Inversion accuracy using the Zoeppritz equations as the forward model at the layer 1-2 interface. Signal-to-noise ratio equals 4 for both the P-P and P-S reflection coefficients. Note the extremely large errors obtained using the P-P inversion method.
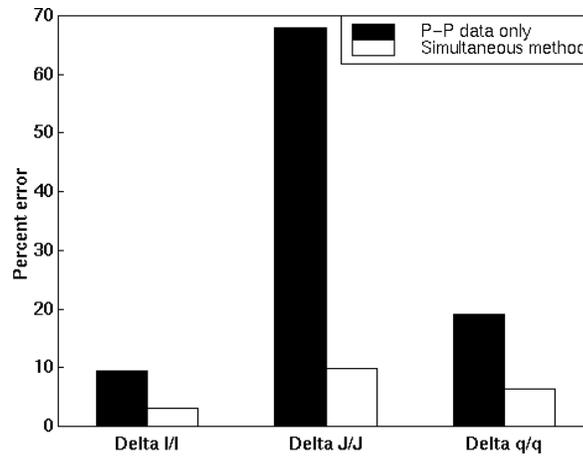
Figure 3.15: Inversion accuracy using the Zoeppritz equations as the forward model at the layer 1-2 interface. Signal-to-noise ratio equals 6 for both the P-P and P-S reflection coefficients.
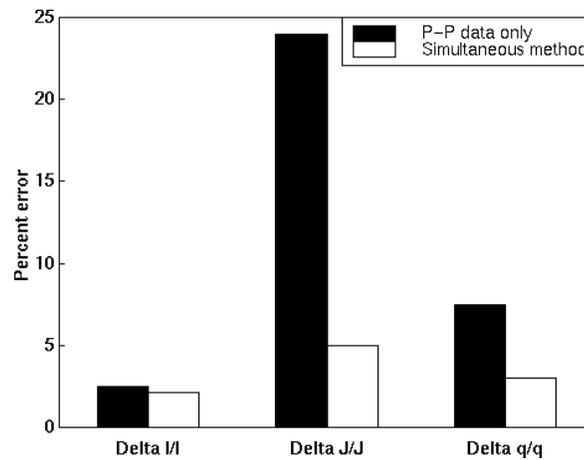
Figure 3.16: Inversion accuracy using the Zoeppritz equations as the forward model at the layer 1-2 interface. Signal-to-noise ratio equals 8 for both the P-P and P-S reflection coefficients.
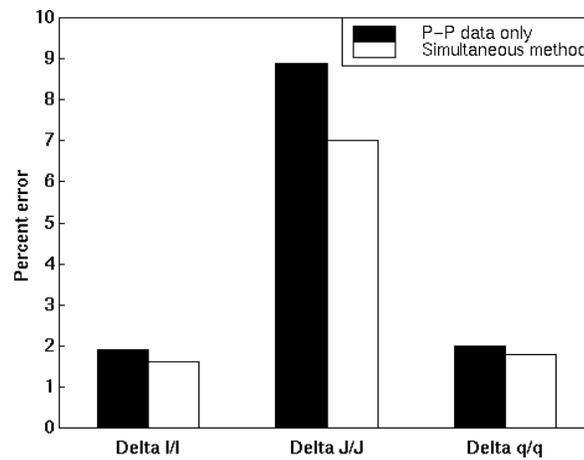
Figure 3.17: Inversion accuracy using the Zoeppritz equations as the forward model at the layer 1-2 interface. Signal-to-noise ratio equals 10 for both the P-P and P-S reflection coefficients.
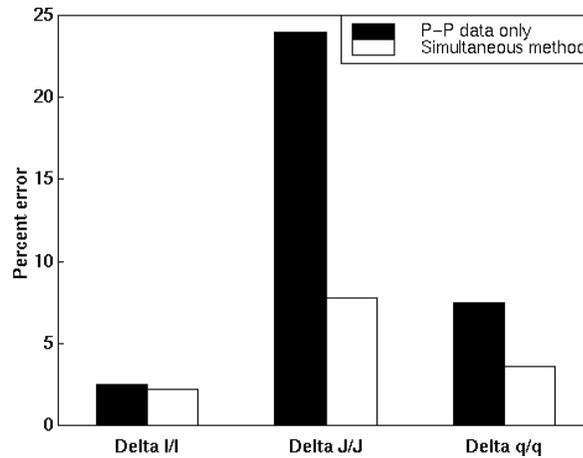
Figure 3.18: Inversion accuracy using the Zoeppritz equations as the forward model at the layer 1-2 interface. Signal-to-noise ratio equals 8 for the P-P and 4 for the P-S reflection coefficients.

For all cases tested, the simultaneous inversion method is more accurate in the presence of noise than the P-P inversion method. This difference is most noticeable where signal-to-noise is at a minimum. It should therefore be reasonable to conclude that the simultaneous inversion method will improve the quality of $\Delta I/I$ and $\Delta J/J$ estimates in realistic cases. The percent error using the simultaneous inversion method remains relatively constant for the signal-to-noise levels tested as shown in figure 3.19. Figure 3.18 shows the results when P-P and P-S reflectivities have different levels of noise. In this case, the P-S reflection coefficients contain a lower signal-to-noise ratio, which is usually observed in real data. Even with this larger amount of noise in the P-S dataset, all estimates of $\Delta I/I$, $\Delta J/J$ and $\Delta q/q$ are more accurate using the simultaneous inversion method. The larger error in the $\Delta J/J$ estimates for both inversion methods tested is due to the increase in error of the Zoeppritz equation approximations with increasing offset. Since shear impedance affects P-P and P-S reflection amplitude most strongly at far offsets, the inversion for the $\Delta J/J$ stack relies most heavily upon far offset contributions. By contrast, compressional impedance affects the P-P reflection amplitude most strongly at near offsets and thus is more accurate since it is more con sistent with the assumptions made in the Zoeppritz equation approximations.
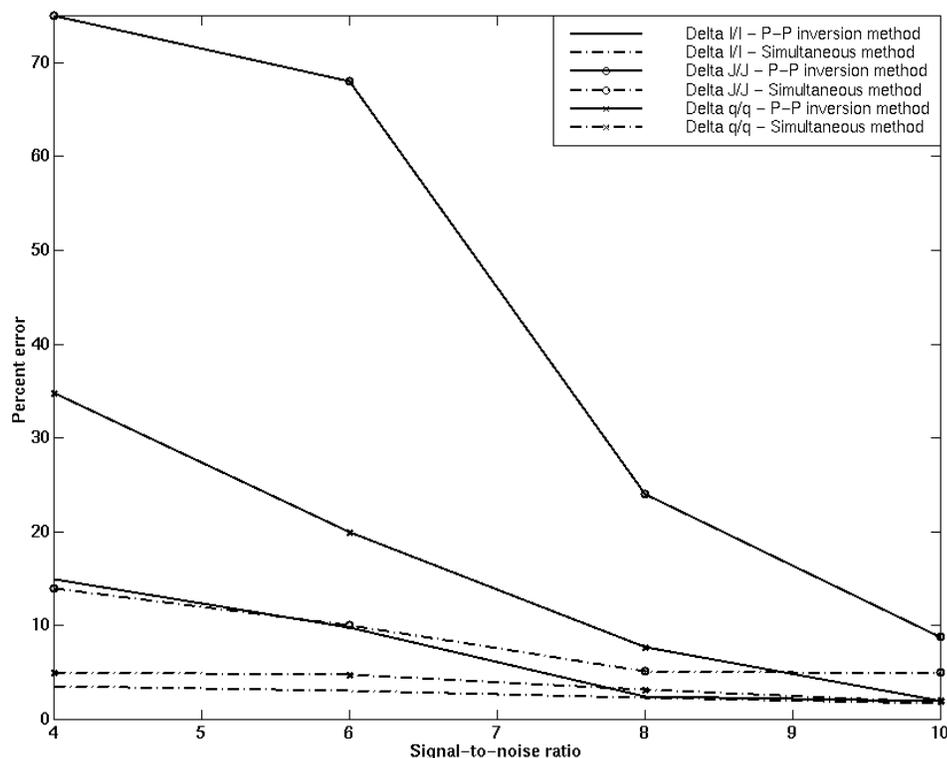
Figure 3.19: Summary of results from the inversion at the layer 1-2 interface for varying levels of noise. Signal-to-noise levels are defined for both the P-P and P-S reflectivities.

3.5 Effect of limited offset stacking

The common practice of performing AVO analyses on unmigrated CMP gathers incorporates amplitude errors due to diffracted arrivals and reflector mis-positioning. Since it is desirable to obtain high quality data for input to an AVO analysis, it is necessary to use some from of true-amplitude, pre-stack migration to properly account for these geometrical effects. The use of a full pre-stack migration is the theoretically preferred way in which to remove these geometrical effects. Since a full pre-stack migration results in a large output data volume and can be computationally challenging, a limited-offset pre-stack migration method was used in this study to reduce the size of the output data volume.

A simple procedure may be used to reduce the amount of data input to AVO analysis. This procedure, called limited-offset stacking, takes the mean of the reflectivity

samples over a given range of offsets and outputs a correspondingly lower number of offset ranges. For instance, if a given offset gather contains 100 offsets, 50 offsets may be generated by averaging every second offset pair. This procedure, if accurate, can reduce the amount of data needed as input to AVO analysis. This method of producing a limited number of common-offset gathers can also be used in conjunction with post-stack migration algorithms as a fast pre-stack migration method (Deregowski, 1990). This procedure, if successful, should allow a post-stack migration algorithm to be used on pre-stack data to create a set of pre-stack migrated offset gathers.

In this study a simple procedure was used to test the accuracy of limited offset stacking compared with using a suite consisting of the full offset range. A similar elastic earth-model to the cases previously tested was used, i.e. elastic parameters given in figure 3.1 for the layer 1-2 interface. The target reflector is located at 1500m depth and the source-receiver orientation consists of offsets ranging from 0m to 2000m in intervals of approximately 20m for a total of 100 offsets. Velocity and density values are given in figure 3.1 for the two-layer model tested. Percent error plots were calculated between the inversion estimates using the full range of offsets and compared to a subset of limited-offset reflectivity samples. For each set of input reflectivity samples, two cases are tested where the first incorporates a noise-free set of reflectivities and the second includes pseudo-random noise with an RMS signal-to-noise ratio of 6 for P-P and P-S reflectivities. The results of these tests are given in figures 3.20, 3.21, 3.22, 3.23 and 3.24.
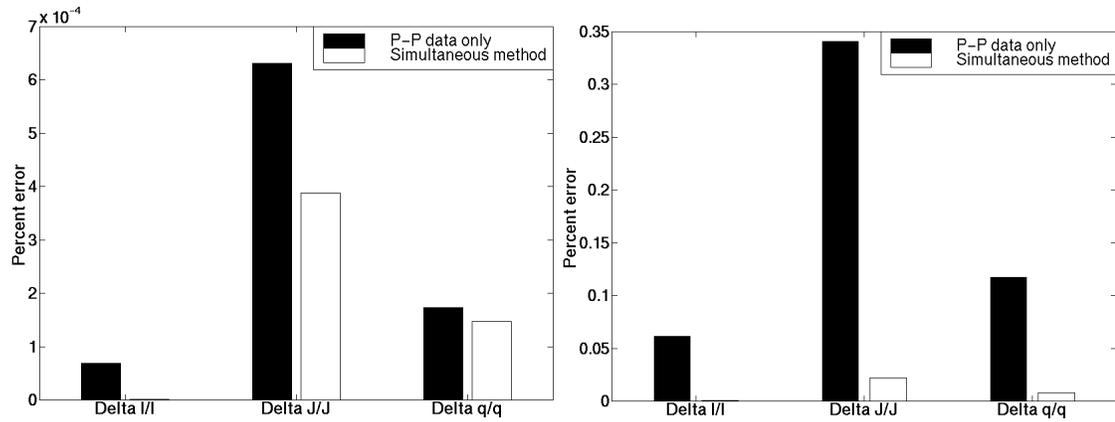
Figure 3.20: Percent error between inversion estimates (ΔI/I, ΔJ/J and Δq/q) consisting of the full offset range of 100 offsets and a limited-offset range consisting of 50 offsets in the noise-free case (left) and the case where the P-P and P-S reflectivities have a signal-to-noise ratio of 6 (right).
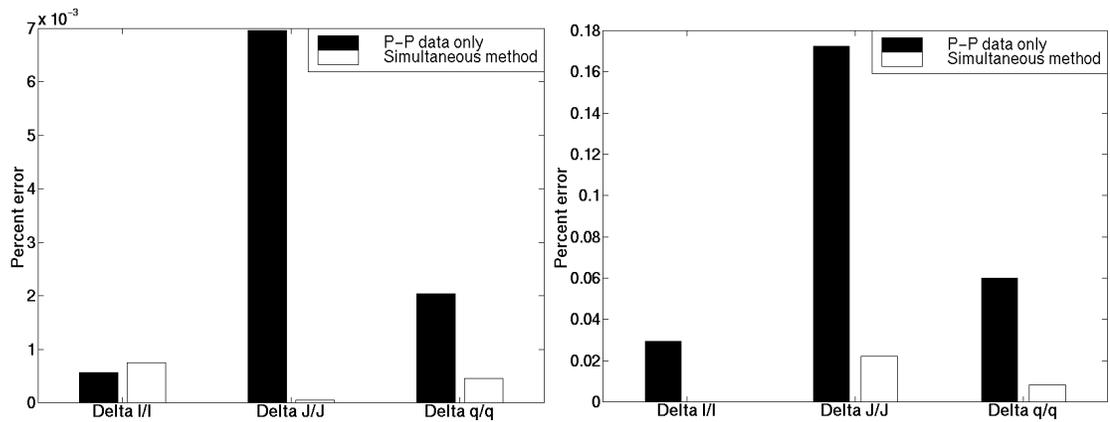
Figure 3.21: Percent error between inversion estimates (ΔI/I, ΔJ/J and Δq/q) consisting of the full offset range of 100 offsets and a limited-offset range consisting of 25 offsets in the noise-free case (left) and the case where the P-P and P-S reflectivities have a signal-to-noise ratio of 6 (right).
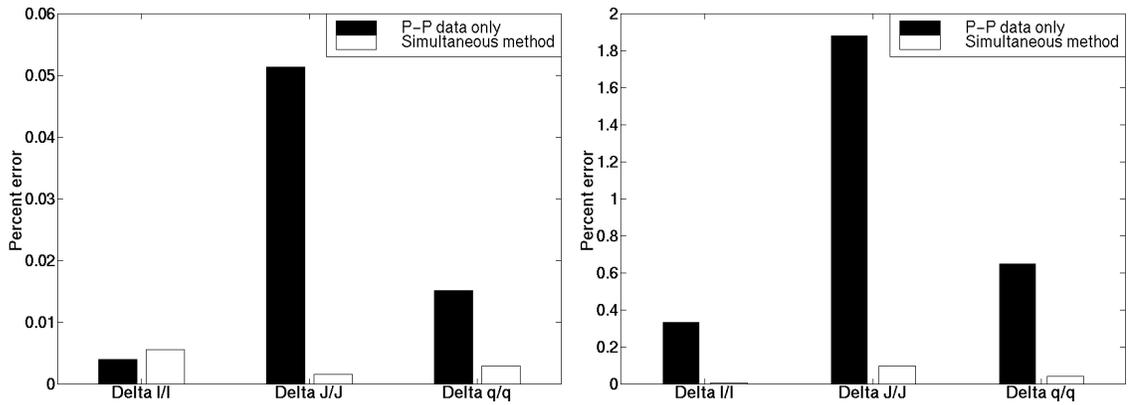
Figure 3.22: Percent error between inversion estimates ($\Delta I/I$, $\Delta J/J$ and $\Delta q/q$) consisting of the full offset range of 100 offsets and a limited-offset range consisting of 10 offsets in the noise-free case (left) and the case where the P-P and P-S reflectivities have a signal-to-noise ratio of 6 (right).
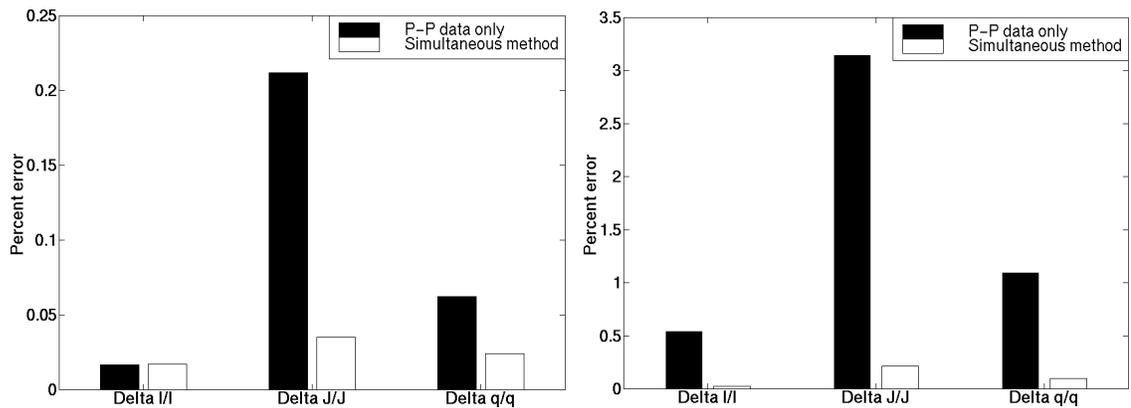
Figure 3.23: Percent error between inversion estimates ($\Delta I/I$, $\Delta J/J$ and $\Delta q/q$) consisting of the full offset range of 100 offsets and a limited-offset range consisting of 5 offsets in the noise-free case (left) and the case where the P-P and P-S reflectivities have a signal-to-noise ratio of 6 (right).
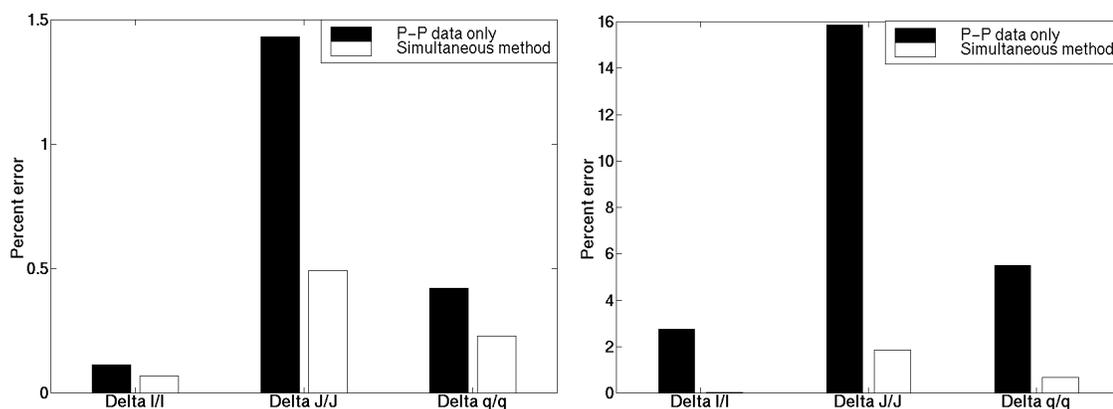
Figure 3.24: Percent error between inversion estimates ($\Delta I/I$, $\Delta J/J$ and $\Delta q/q$) consisting of the full offset range of 100 offsets and a limited-offset range consisting of 2 offsets in the noise-free case (left) and the case where the P-P and P-S reflectivities have a signal-to-noise ratio of 6 (right).

Inversion accuracy was generally found to be adequate for all cases tested. In other cases tested, inversion accuracy was found to be comparable except for cases where there are large changes in reflectivity behavior such as near critical angles. The accuracy of these inversion results is both a function of reflectivity behavior with offset and of weighting behavior with offset. For instance, if reflectivity behavior is constant or linear with increasing offset, averaging over a limited offset range and inverting the result will not significantly affect the accuracy of the inversion estimate. For most cases tested, accuracy was improved using the simultaneous inversion method. Both methods are sufficiently accurate even in the case where only two offsets were used (figure 3.24).

3.6 Synthetic data testing

In order to evaluate the simultaneous inversion method in a multi-layer, band-limited situation, a series of synthetic seismic datasets were constructed. These datasets were constructed from well logs containing bulk density, compressional and shear velocity logs from the surface to just below the target zone. These well logs were subsequently blocked or averaged using a median algorithm over each picked formation

top, then output. Since a velocity/density-depth model is now available, testing of the simultaneous inversion method should now be straightforward.

3.6.1 Blackfoot geological overview

A number of authors have described the geology in the Blackfoot area in detail, Layer et al. (1949), Wood and Hopkins (1992), Leckie et al. (1994). The Blackfoot field is located approximately 15km southwest of the town of Strathmore Alberta in Township 23, Range 23, West of the 4th Meridian. Figure 3.25 shows the general stratigraphic sequence in the area of study. The primary target of interest in this area is the Lower Cretaceous age, incised valley fill sediments of the Glauconitic formation. These incised valley deposits generally trend north-south with some degree of local variation in the study area. The base of the Glauconitic channel system represents an unconformity surface cutting through the underlying primarily shale Ostracod and Sunburst members. Underlying the Glauconitic Valley fill sediments are the Detrital and Mississippian formations. Significant incision into the underlying Mississippian Shunda formation has been observed in the study area. The incised valley sediments of the Glauconitic member can be further subdivided into three phases of deposition, though all three phases may not be present everywhere (Miller, 1996). The lower and upper members consist primarily of quartz sandstones with local variations in clay content resulting in an average porosity of approximately 18%. The middle member is a relatively thin, non-porous lithic sandstone layer. The individual thickness of each member varies from 0 to 20m while the whole channel system generally never exceeds 35m in thickness. Hydrocarbon reservoirs are found in both the upper and lower members. Hydrocarbon accumulations are trapped as stratigraphic pinch-outs against non-porous regional strata or low porosity channel sediments. The primary hydrocarbon at the Blackfoot field is oil, though significant gas may be present in the upper channel member. This upper channel is of most interest in this study since it gives the most distinctive amplitude variation with offset response due to the presence of reservoir gas (Simin et al., 1996, Dufour et al., 1998).
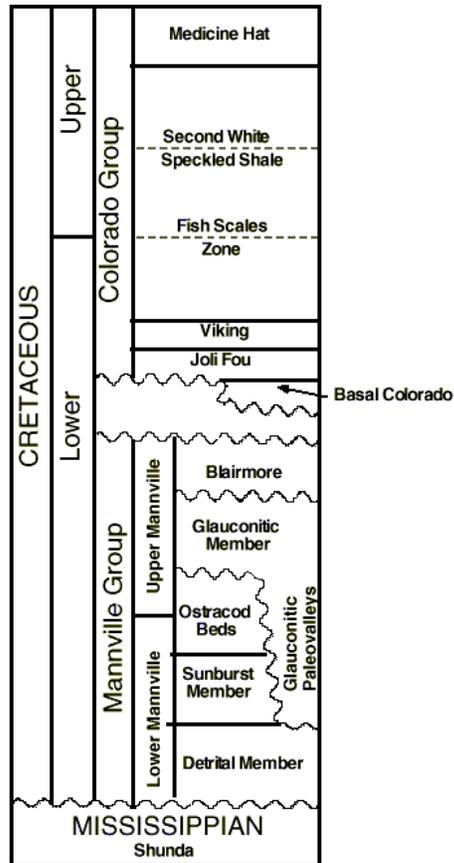
Figure 3.25: Statigraphic sequence in the Blackfoot area. (Modified from Wood and Hopkins, 1992).

3.6.2 Blackfoot synthetic study

To test the performance of the simultaneous P-P and P-S inversion method in the presence of more realistic data, two models, based on blocked sonic and density logs were constructed. These models are represented by a set of well logs over a producing gas reservoir (the Upper Glauconitic channel) and a non-producing regional zone. Both logs were spliced from a common upper section consisting of compressional and shear wave sonic logs and a bulk density log from well 09-08-023-23W4. Next, well 08-08-023-23W4 was spliced below a common picked horizon, the GLCZ marker, just above the channel zone and added to the 09-08 well log below the GLCZ marker. The same procedure was used to obtain a non-producing, regional well log corresponding to well location 09-17-023-23W4 in figure 3.26.
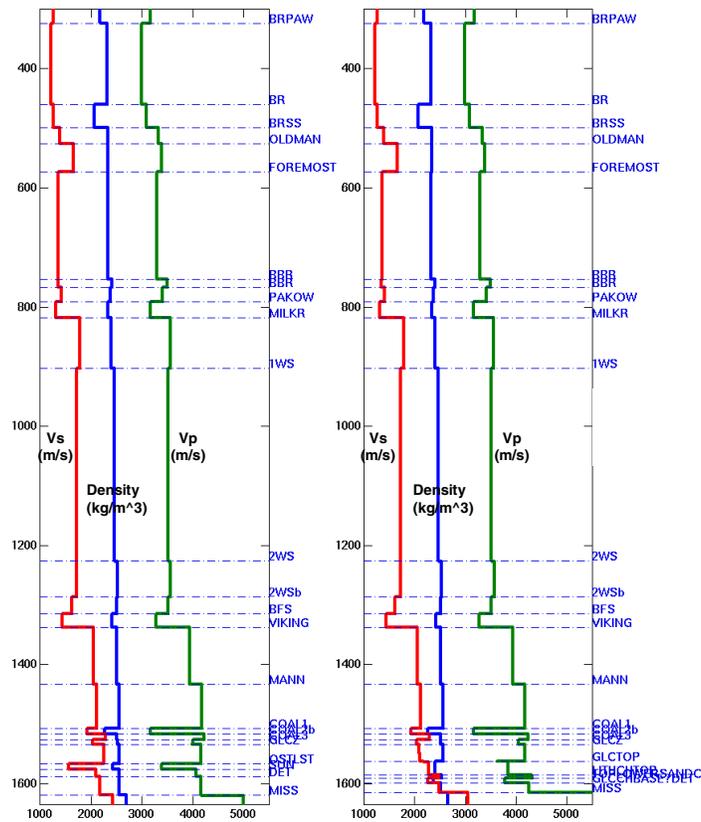
Figure 3.26: Composite well logs obtained by splicing logs from the 09-17 regional (left) and 08-08 producing channel (right) well locations below the GLCZ marker to the 09-08 well log. Notice both logs contain a common velocity-density model from the begining of the log to the GLCZ marker.
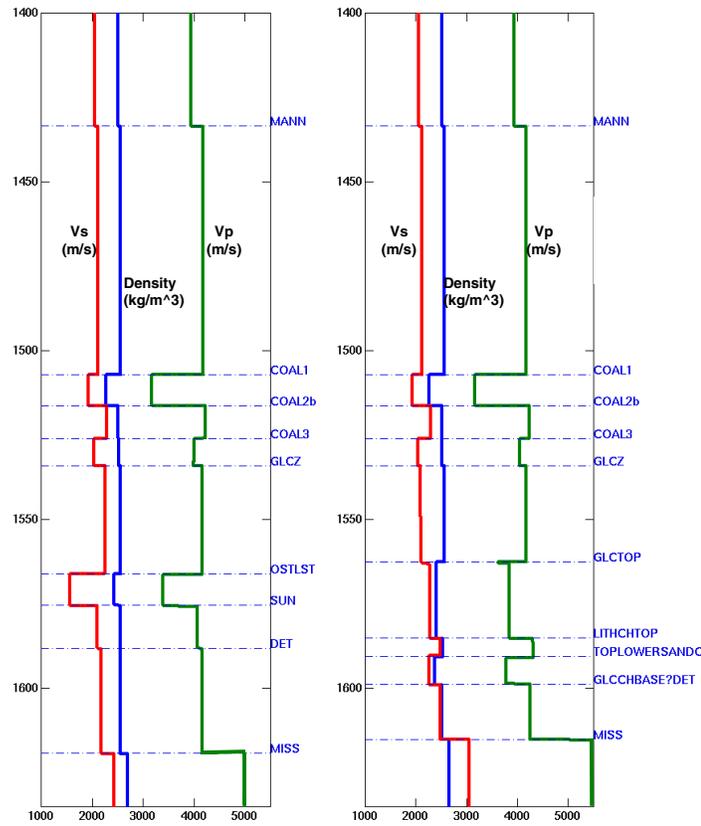
Figure 3.27: Detailed view of the non-producing 09-17 (left) and producing 08-08 (right) channel zone well locations.

From these well logs, a highly smoothed velocity-depth model was obtained in order to calculate reflection-transmission angles for both a P-P and a P-S reflection using standard acquisition geometry. This smoothed velocity-depth model was obtained by fitting a straight line in a least-squares sense to the velocity logs in figure 3.26. Figure 3.28 below summarizes the results of this smoothing procedure for the compressional and shear velocity logs. From the smoothed velocity logs obtained in figure 3.28, a simple raytracing procedure was undertaken to calculate angles of incidence, reflection and transmission for each reflector interface. For this procedure the source and receivers are assumed to be located at 0m depth. Incidence angles were thus calculated assuming receivers located from 0 to 2000m offsets in intervals of 40m relative to the source position. The results of this raytracing procedure for the P-P and P-S reflection are shown

in figure 3.29. Notice the greater range of incidence angles for the P-S reflection compared to the P-P reflection.
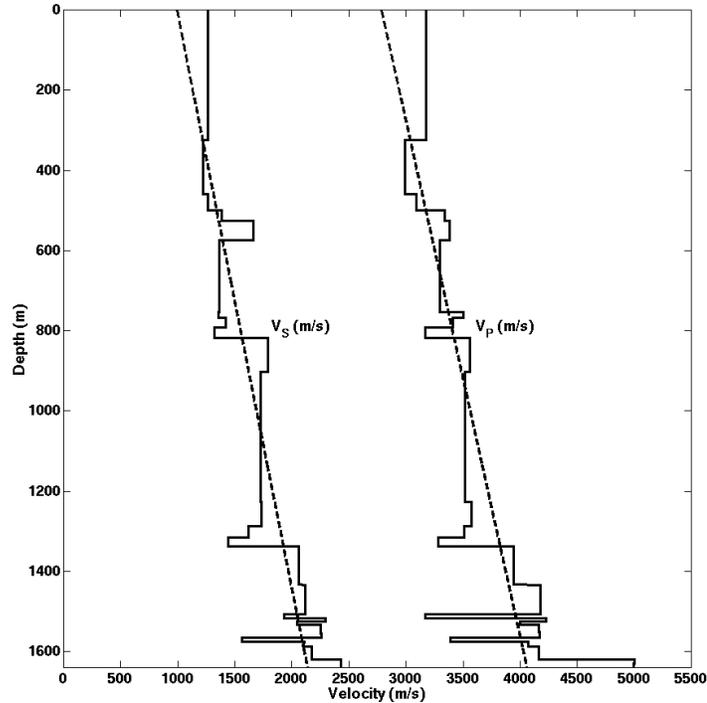
Figure 3.28: Blackfoot regional velocity-depth model obtained from the composite well log at the 09-17-23-23W4 location. Dashed lines are the smoothed velocity functions used in the calculation of the weights.

Since both the stand-alone P-P and the simultaneous inversion procedures outlined in chapter 2 required averaged angles of reflection-transmission for a P-P and a P-S reflection event (average values of θ_{PP}, φ_{PP}, θ_{PS} and φ_{PS} for each interface), it is necessary to also compute angles of reflection and transmission for each reflection case. For the P-P reflection case, the average angles of reflection-transmission are approximately equal to the incidence angles for the smoothed velocity model, i.e. $\theta_1 \approx \theta_2 \approx \theta_{PP}$ across a given interface. In the P-S reflection case, θ_{PS} corresponds to the average between a reflected P and a transmitted P-wave angle given the incidence angles in figure 3.29 (right). Again, θ_{PS} approximately equals the set of incidence angles given in figure 3.29 for the P-S reflection case. By contrast, φ_{PS} corresponds to the average between a

reflected S and a transmitted S-wave angle given the same set of P-S incidence angles in figure 3.29. Figure 3.30 shows the raytraced estimate for the average between the reflected and transmitted shear angle for the P-S reflection case, φ_{PS}.
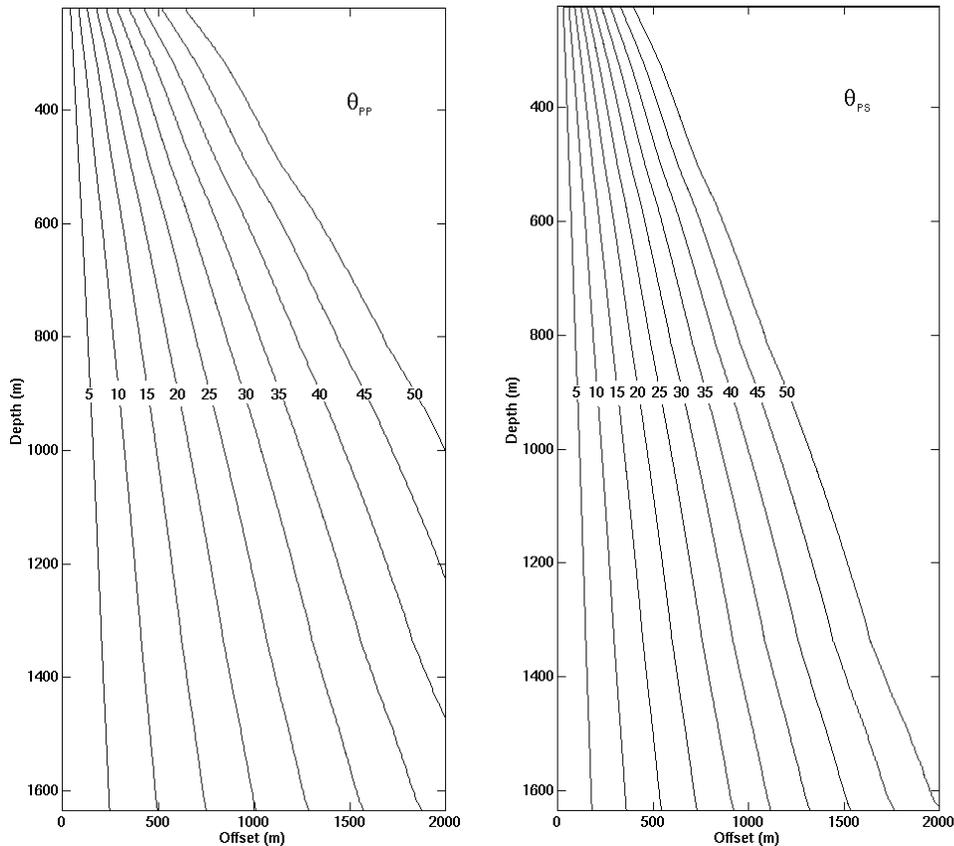
Figure 3.29: Raytraced incidence angles for a P-P (left) and P-S (right) offset gather using the smoothed velocity-depth model in figure 3.27 and the source-receiver geometry described previously. The larger incidence angles of the P-S offset gather are due to the movement of the point of reflection towards the receiver in the case of a P-S reflection.

Notice the angle of shear reflection-transmission for the P-S case is much less than for the case of a P-P reflection. Also notice the contours generally are a maximum at small depths and far offsets thus requiring some type of muting procedure at these locations.

Since the smoothed values of α, β, θ and φ are now available for each case of a P-P and a P-S reflection event, it is possible to calculate the weights for each inversion

method in question. For the stand-alone P-wave weighted stacking method, the weights applied to the P-P dataset are given in equations 2.25 and 2.26. These weights when multiplied by a corresponding offset-dependent reflectity sample and summed will form estimates of $\Delta I/I$ and $\Delta J/J$. Figure 3.31 summarizes the weights applied to the P-P dataset to extract estimates of $\Delta I/I$ and $\Delta J/J$.
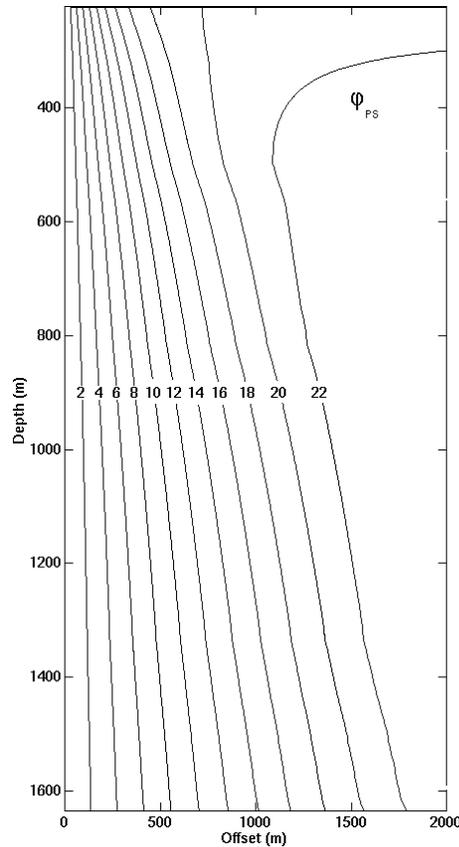
Figure 3.30: Average angles of reflection-transmission for a mode-converted shear wave in the case of a P-S reflection using the smoothed velocity-depth model in figure 3.27.

These weights are very similar to those given by Smith and Gidlow, 1987. These values differ somewhat as they represent weights for $\Delta I/I$ and $\Delta J/J$, not $\Delta\alpha/\alpha$ and $\Delta\beta/\beta$ and represent a different velocity-depth model. Generally, these weights change sign with increasing offset. Again as shown previously, this effect tends to cancel the signal contribution of middle offsets and thus is not desirable. Also notice the weights for the $\Delta I/I$ estimates are generally smaller than for the case of the $\Delta J/J$ weights. These weights

tend to vary less with offset as depth increases due to the decrease in variation with incidence angle.
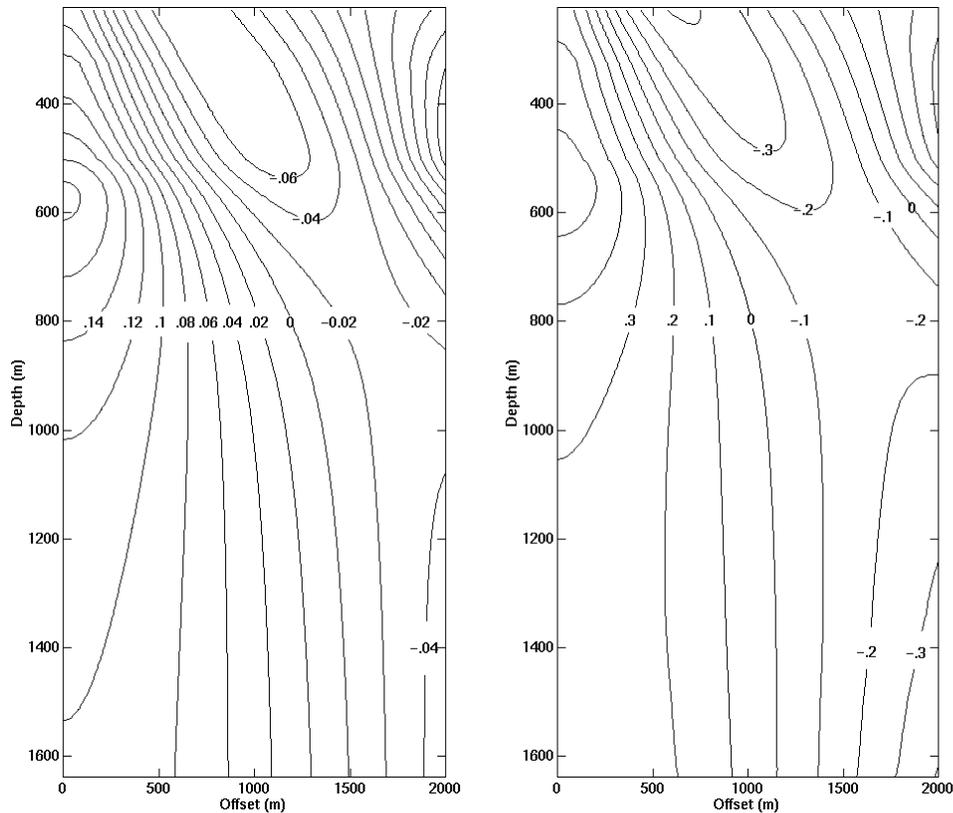
Figure 3.31: Offset-dependant weights calculated from the smoothed background velocity model (figure 3.27) and raytraced average angles of reflection-transmission (figure 3.28-3.29) applied to the P-P dataset for the ΔI/I (left) and ΔJ/J (right) reflectivities. Note in both cases the difference between the positive near and negative far-offset weights.

Weights for the Pseudo-Poisson's ratio reflectivity, Δq/q can be calculated by simply subtracting the ΔJ/J weights from the ΔI/I weights shown in figure 3.31. As shown in section 2.3.2, a number of other petrophysical parameters can be estimated from the weights of ΔI/I and ΔJ/J. Figure 3.32 shows the weights which when applied to the corresponding P-P offset gather will result in a single Δq/q reflectivity trace. Notice again the greater difference between the weights at a shallower depth compared to deeper levels due to the greater range of incidence angles at shallower depths. This observation also

implies the inversion results at shallower depths are more sensitive to the accuracy of the smoothed background velocity model in figure 3.27.
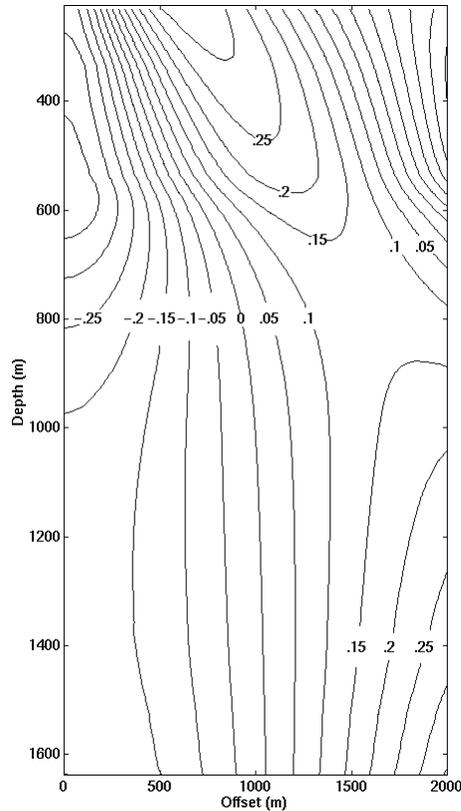
Figure 3.32: Offset-dependant weights calculated from the smoothed background velocity model (figure 3.27) and raytraced average angles of reflection-transmission (figure 3.28-3.29) applied to the P-P dataset for the $\Delta q/q$ reflectivities.

In a similar manner, the weights which when applied to the P-P and P-S synthetic offset gathers using the simultaneous inversion method to extract estimates of $\Delta I/I$ and $\Delta J/J$ can be plotted. Figure 3.33 shows these weights for the P-P and P-S offset gathers which will extract estimates of $\Delta I/I$. These weights are applied to the P-P dataset very differently from those in figure 3.31. The weights in figure 3.33 (left) generally tend to vary less with offset compared to figure 3.31. In the case of the P-S $\Delta I/I$ weights there appears to be a more significant variation in weight magnitude with offset. Since the P-S reflection coefficients are smaller than the same corresponding P-P reflectivity, the $\Delta I/I$ weights for the P-S dataset have a smaller effect upon the estimate of $\Delta I/I$.
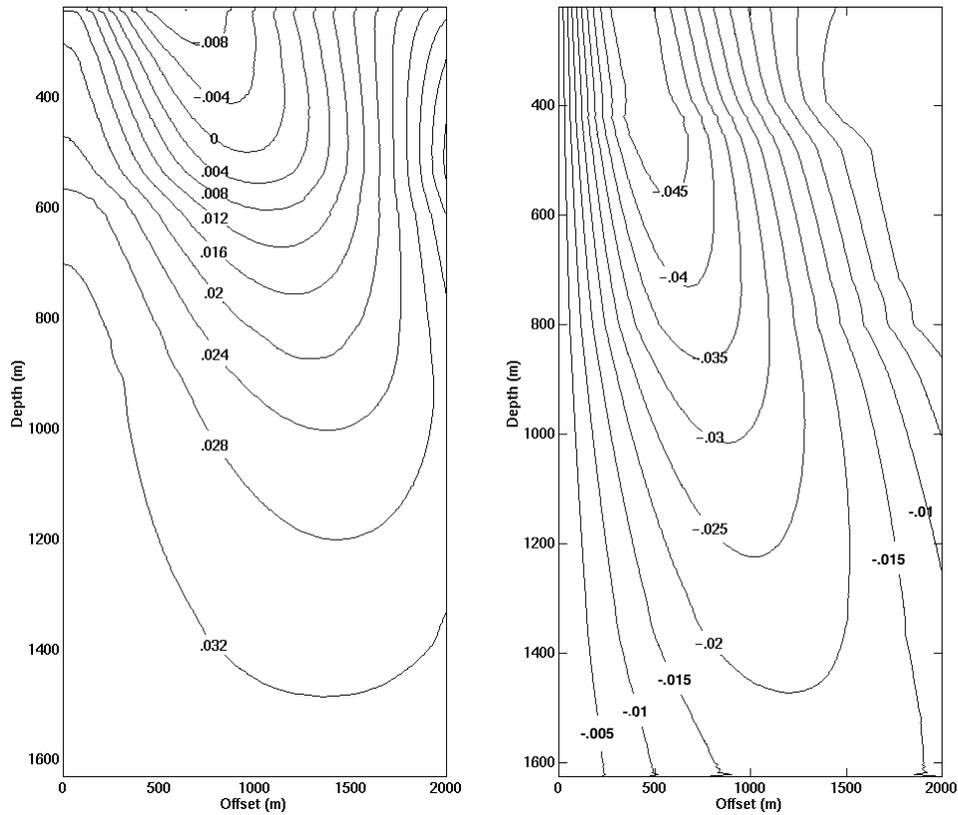
Figure 3.33: Offset-dependant, $\Delta I/I$ weights calculated from the smoothed background velocity-depth model applied to the P-P (left) and P-S (right) datasets using the simultaneous inversion method. Notice the weighting behavior with offset for the P-P dataset is generally more constant with offset using the simultaneous inversion method compared to figure 3.31 (left).

The $\Delta J/J$ weights applied to the P-P and P-S offset synthetic data are shown in figure 3.34. The weights in figure 3.34 (left) and figure 3.31 (right) show similar behavior with offset, but differ significantly in magnitude. Again, the P-S reflection coefficient is generally more dependant on changes in shear impedance than the P-P reflection coefficient. As a result, the weights applied to the P-S section to extract the estimate of $\Delta J/J$ are larger in magnitude than for the corresponding P-P section. Again, this effect can be noticed in figure 3.34 by examining the magnitudes of the weights applied to the P-P and P-S datasets. Similarly to the cases previously examined, these weights change more rapidly nearer to the surface and as such are subject to greater error.
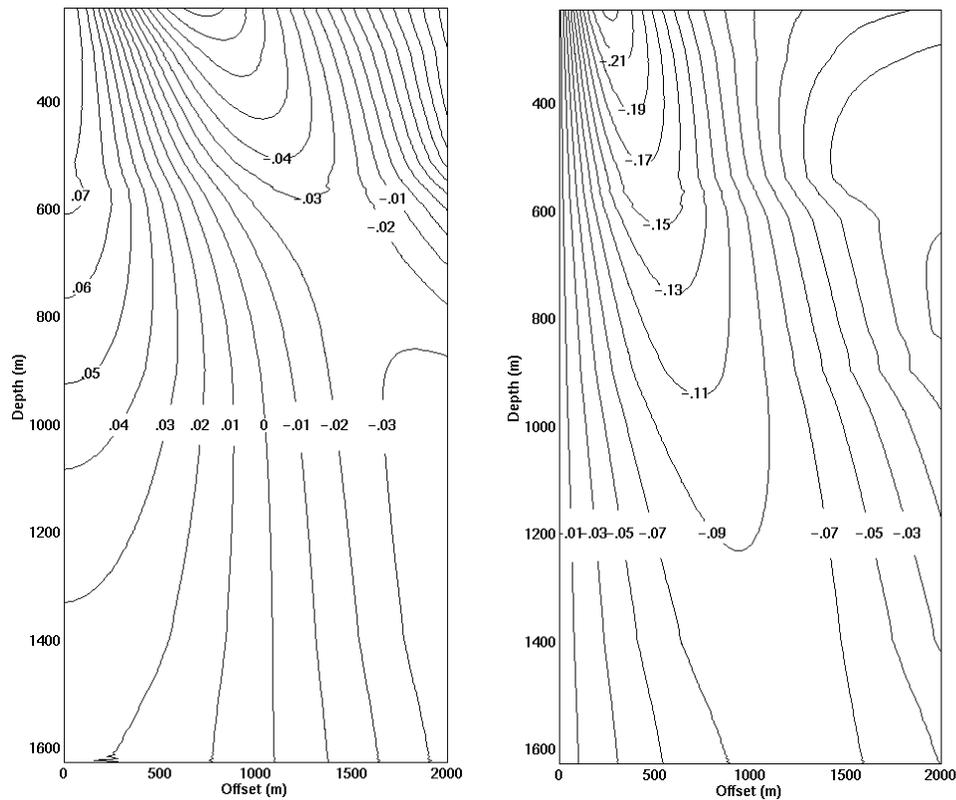
Figure 3.34: Offset-dependant, ΔJ/J weights calculated from the smoothed background velocity-depth model applied to the P-P (left) and P-S (right) datasets using the simultaneous inversion method.

Figure 3.35 shows the Δq/q weights applied to each of the P-P and P-S datasets. In the case of the P-P inversion, Δq/q weights, the magnitude of these weights increases with increasing offset. In most P-P AVO anomalies, the P-P reflection coefficient increases in magnitude with increasing offset. This means that the Δq/q anomaly is most dependent upon the contribution from far offset traces. In the case of the P-S, Δq/q weights, the magnitude of these weights generally reaches a maximum at middle offsets. It can further be shown in most P-S AVO anomalies, the P-S reflection coefficient reaches a maximum magnitude at middle offsets. This shows that fractional changes in the Vp/Vs ratio (Δq/q) most strongly affect the middle offsets on a P-S offset gather.
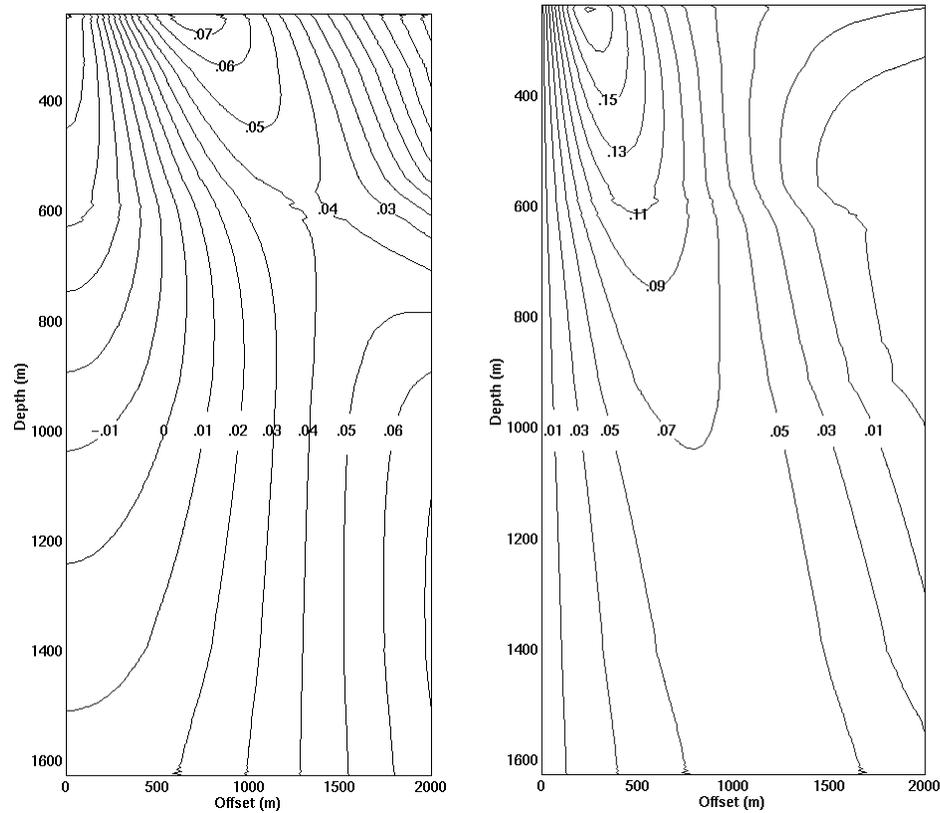
Figure 3.35: Offset-dependant, Δq/q weights calculated from the smoothed background velocity-depth model applied to the P-P (left) and P-S (right) datasets using the simultaneous inversion method.

In order to test the simultaneous inversion algorithm, a set of four different offset gathers, two each for P-P and P-S reflectivity, were constructed from the two composite wells logs obtained previously in figure 3.36. In the case of this study, NMO stretch factors were included in these synthetic datasets. For both the non-producing regional well 09-17, and the Glauconitic channel well 08-08, a P-P offset gather was constructed. For each case, a zero-phase wavelet was used with a bandpass filter at 5-10-60-75Hz. These offset gathers are shown in figures 3.36 and 3.37 for wells 09-17 and 08-08 respectively. Similarly, for the same two wells, a P-S offset gather was constructed for each. Figures 3.38 and 3.39 show these offset gathers for the 09-17 and 08-08 wells respectively. These P-S offset gathers were constructed using a zero-phase wavelet and a bandpass filter at 5-10-40-55Hz. Prior to output, all offset gathers were converted to

depth. This depth conversion is necessary since an exact correlation must be made between the P-P and P-S events on the two sections. Since both the offset-dependant weights and the offset synthetic data are now in depth, the weighted stacking procedure may now be performed.
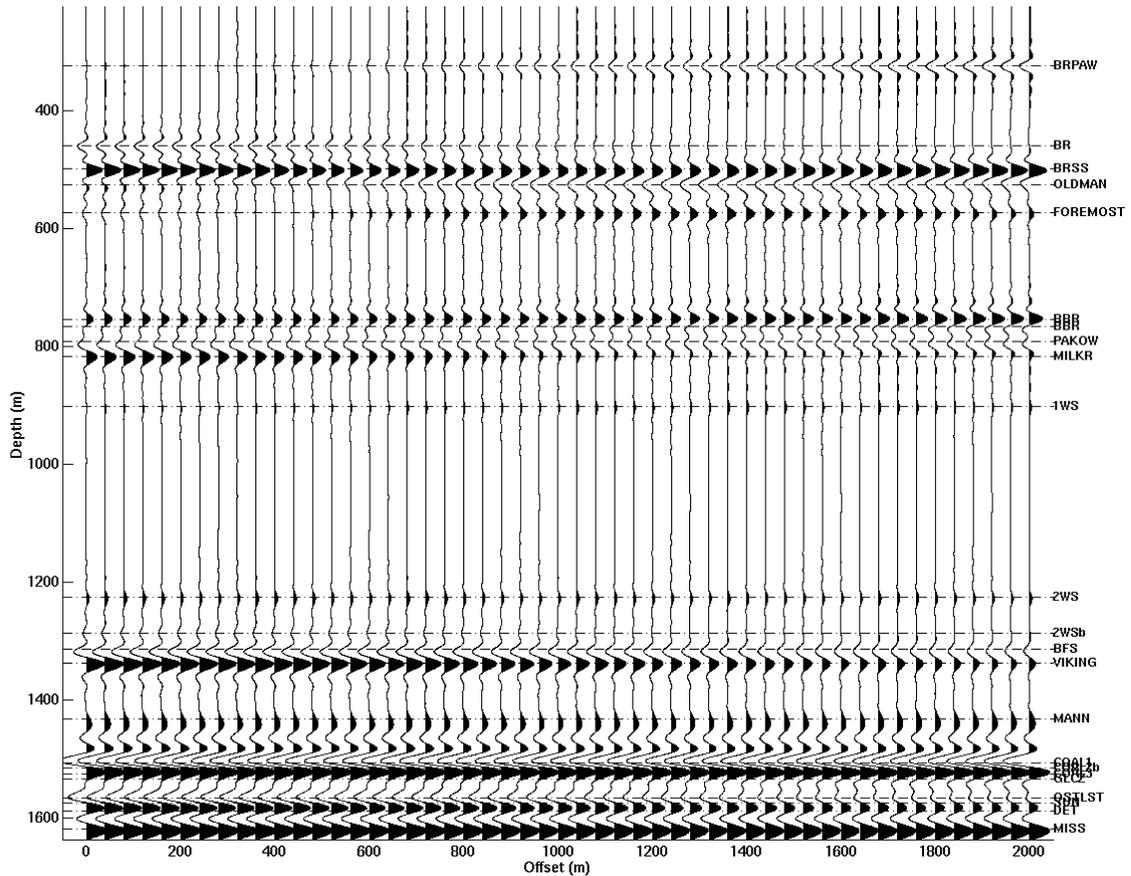
Figure 3.36: Computed P-P synthetic seismogram corresponding to the non-producing regional well at 09-17-023-23W4. This section was computed using a zero-phase wavelet with a pass-band at 5-10-60-75 Hz.

An important point to consider is the temporal (or depth) and lateral resolution characteristics of P-P and P-S surface seismic data. Toksoz et al. (1978), observed brine and water saturated rocks are generally more attenuative to shear waves compared to compressional waves (i.e. $Q_S > Q_P$). It was further observed that shear waves are generally expected to attenuate more quickly than compressional waves, more than can otherwise be accounted for by their slower velocity alone. Geis et al. (1990), observed

converted wave VSP sections have superior temporal resolution than P-wave VSP sections. This result leads to the conclusion that shear waves are most strongly attenuated in the near-surface. Since the simultaneous P-P and P-S inversion method combines two different datasets with different resolution characteristics, it is necessary to understand these differences and their effect upon the inversion results. As observed in chapter 2, the P-S reflection coefficient is most strongly dependent upon shear impedance contrasts, whereas the P-P reflection coefficient is most strongly dependent upon compressional impedance contrasts. Since the $\Delta J/J$ estimate using the simultaneous inversion method is most strongly dependent upon P-S reflectivities, the inversion result may be of reduced temporal resolution compared to using the P-wave only method alone. Generally, in the case of real data the resolution of P-P and P-S data in depth is approximately the same. In the case of this study, the P-P and P-S offset synthetic data were given similar vertical resolution characteristics.
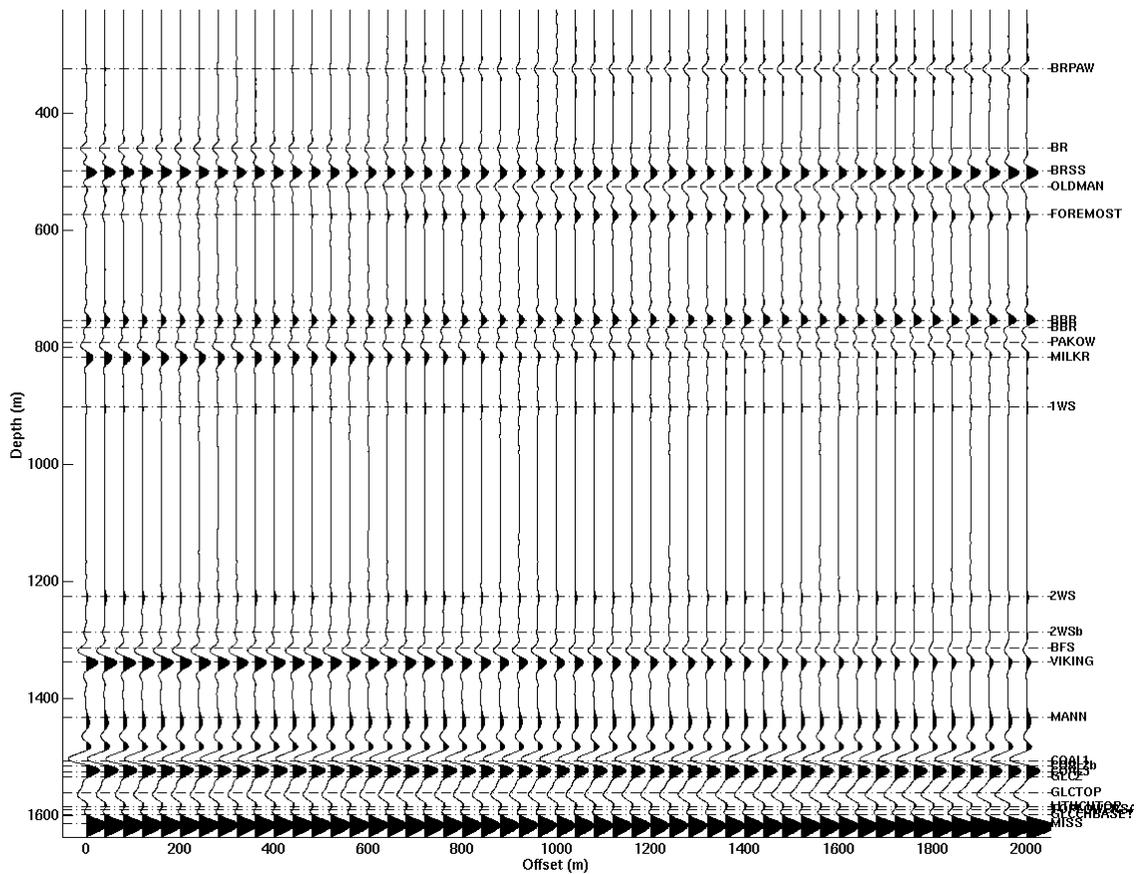
Figure 3.37: Computed P-P synthetic seismogram corresponding to the producing Glauconitic channel well at 08-08-023-23W4. This section was computed using a zero-phase wavelet with a pass-band at 5-10-60-75 Hz. The target zone corresponds to the GLCTOP marker at approximately 1560m depth.
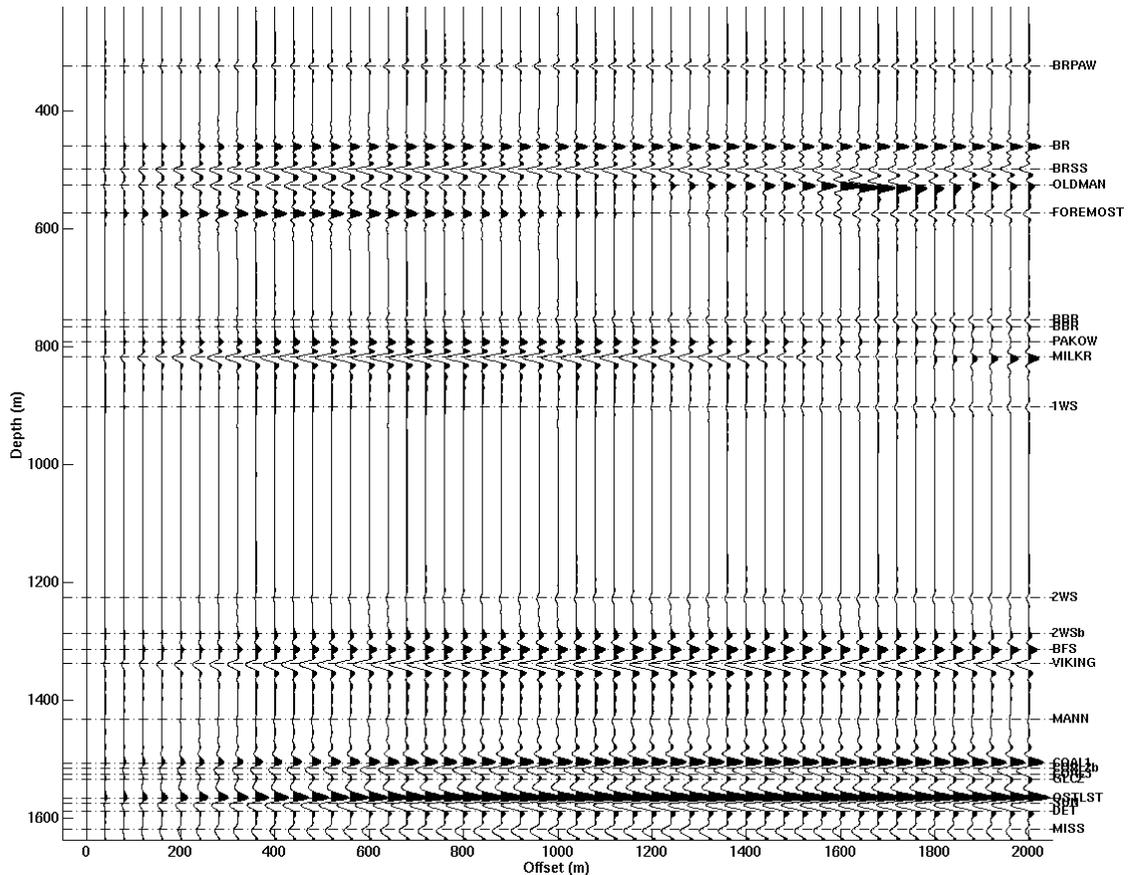
Figure 3.38: Computed P-S synthetic seismogram corresponding to the non-producing regional well at 09-17-023-23W4. This section was computed using a zero-phase wavelet with a pass-band at 5-10-40-55 Hz. Notice the vertical resolution is similar to figure 3.36 despite having a lower temporal frequency bandwidth since both sections were converted to depth prior to display.

The next step is to compute the weighted stack of the P-P and P-S offset gathers. This weighted stacking procedure may be attempted by multiplying each of the offset and depth dependent weights by its corresponding offset and depth dependent reflectivity sample. Following this procedure, each depth sample is summed over all offsets to form the depth-dependent inversion results of $\Delta I/I$, $\Delta J/J$ and $\Delta q/q$. The results of the weighted stacking procedure are displayed in figure 3.40 for the P-P only and simultaneous inversion methods at the regional 09-17 well location. As expected, both methods give similar results using synthetic, noise-free seismic data. However, the velocity/density vs.

depth model given in figure 3.26 violates several assumptions made in the Zoeppritz equation approximations, i.e. small elastic changes across a given interface. Since the target of interest (GLCC channel) is at approximately 1560m depth, and consequently has a limited maximum incidence angle, no attempt was made to limit the offset range used to calculate the weighted stack, i.e. no trace mute was used to eliminate far offsets. The maximum angles of incidence at the target depth do not exceed 35 degrees for the P-P and 50 degrees for the P-S datasets. Figure 3.39 (right) shows the exact, bandlimited reflection coefficients obtained directly from the blocked sonic and density logs at well 09-17-023-23W4. These reflection coefficients have the same vertical resolution as the input well logs.
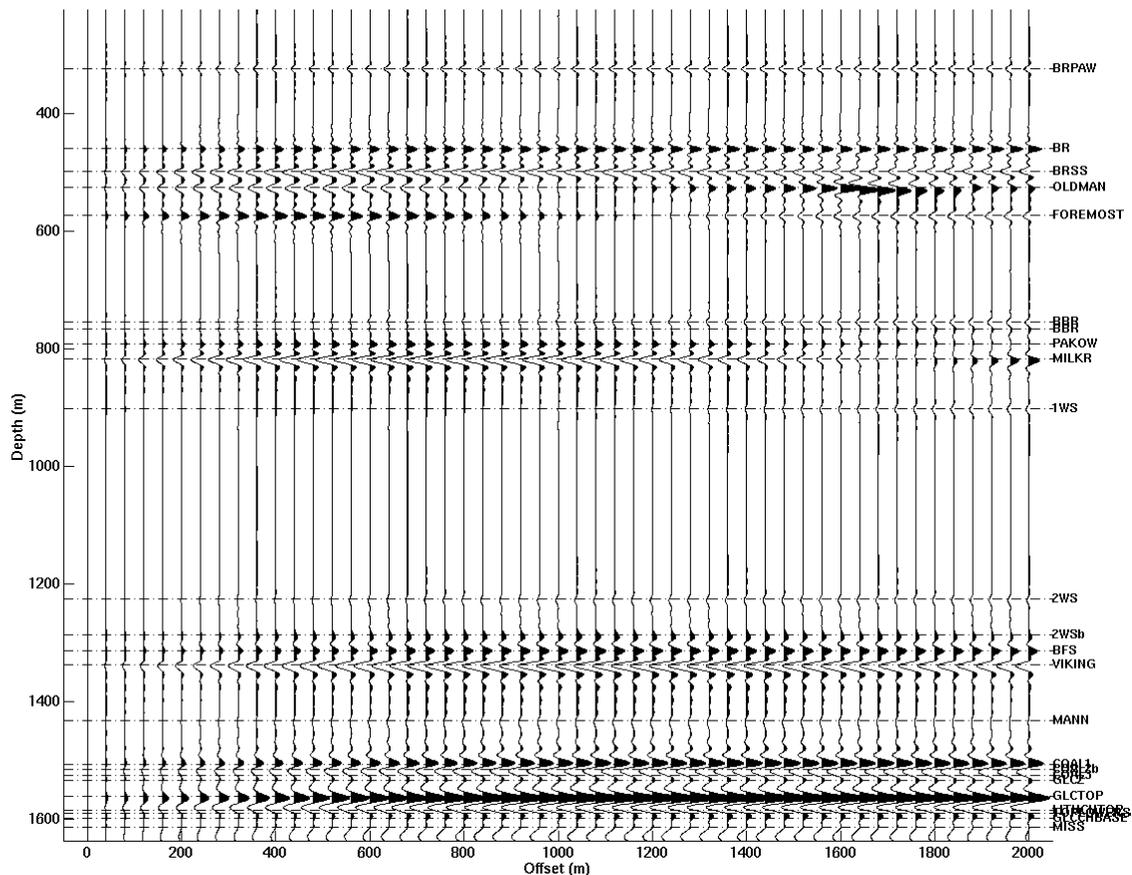

Figure 3.39: Computed P-S synthetic seismogram corresponding to the producing Glauconitic channel well at 08-08-023-23W4. This section was computed using a zero-phase wavelet with a pass-band at 5-10-40-55 Hz.

Since the vertical resolution of the P-P and P-S datasets differ slightly, the bandwidth of the inversion results in figure 3.40 appears different for the two methods tested. As noted previously, the vertical resolution of P-P and P-S surface seismic data is generally comparable. Significant tuning effects can be observed when comparing figures 3.40a (left and center) and 3.40b as a result of the limited frequency band of the inversion results. Notice however the strong correlation between the exact values and the computed inversion result. There is slightly higher frequency content in figure 3.40a (center) compared with the bandlimited inversion result (right) due to the higher frequency content of the input P-S seismic data.
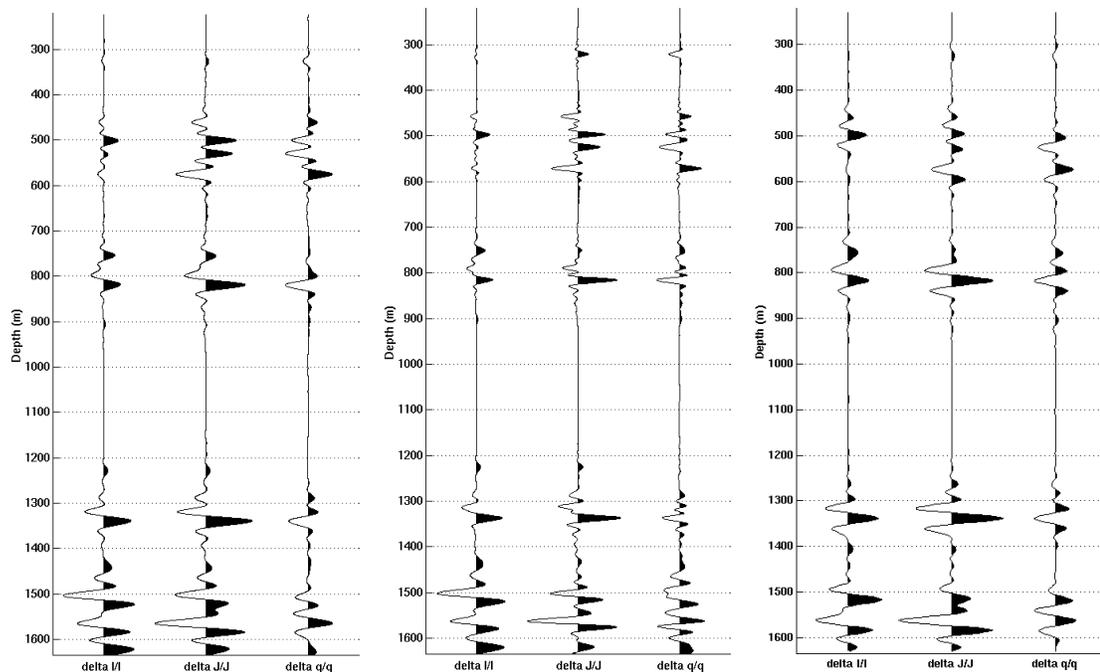
Figure 3.40a: Computed results of the weighted stacks for the P-P only (left) and simultaneous inversion methods (center) at the non-producing, 09-17, regional well location. Both methods give comparable results for this simple noise free case. Some difference can be observed in the frequency bandwidth of these estimates using the P-P and simultaneous P-P and P-S inversion methods. Exact fractional values of $\Delta I/I$, $\Delta J/J$ and $\Delta q/q$ (right) in the bandlimited case derived from the composite well log in figure 3.25 (left). Exact fractional values of $\Delta I/I$, $\Delta J/J$ and $\Delta q/q$ (lower) computed directly from well logs.
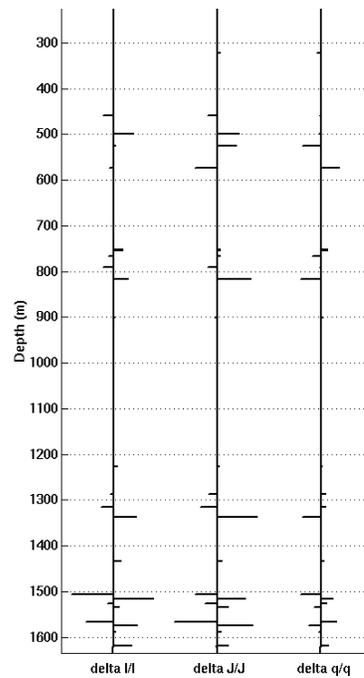
Figure 3.40b: Exact fractional values of ΔI/I, ΔJ/J and Δq/q (lower) computed directly from well logs.

The same procedure is used to compute the weighted stack for the known Glauconitic channel well location at 08-08-023-23W4. The results of this weighted stack are given in figure 3.41. Again notice the close correlation between the inversion results using the Smith-Gidlow and simultaneous inversion methods. The greatest differences between these two methods are observed at the depth of the channel zone (at 1560-1600m depth in figure 3.41) where tuning effects are most significant.
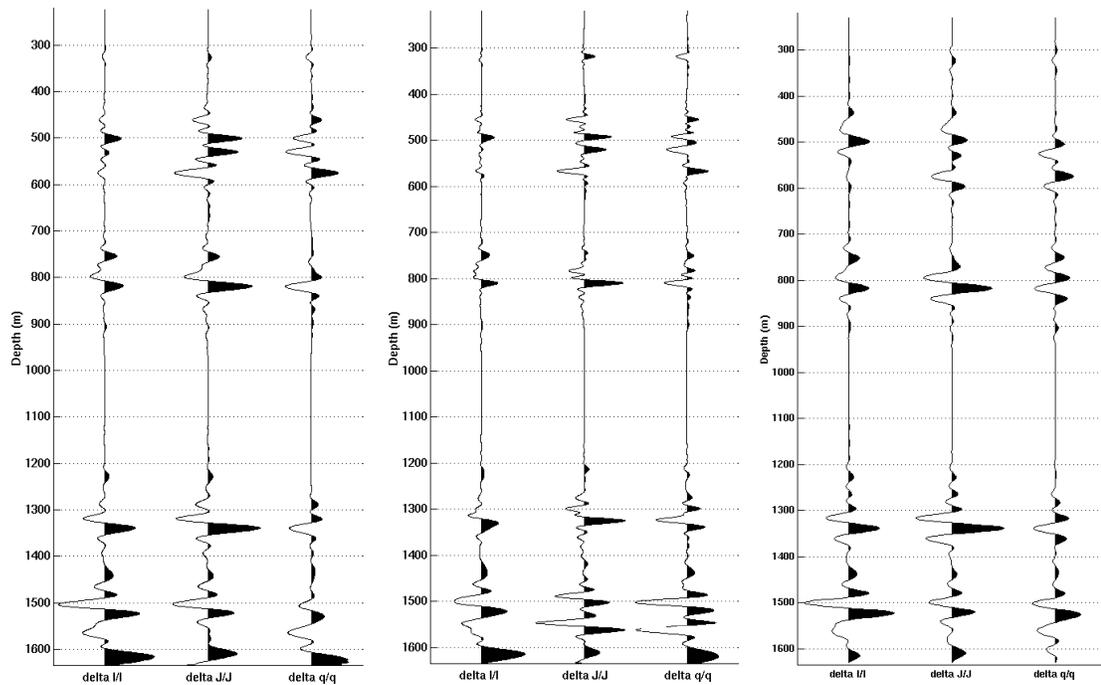
Figure 3.41a: Computed results of the weighted stacks for the P-P only (left) and simultaneous inversion methods (center) at the Glauconitic channel well location. Both methods give comparable results for this simple noise free case. Exact fractional estimates of $\Delta I/I$, $\Delta J/J$ and $\Delta q/q$ (right) for the bandlimited case derived from the composite well log in figure 3.26 (right). The $\Delta J/J$ estimate using the simultaneous inversion method (center) appears to be higher resolution due to the slightly greater resolution in depth of the P-S synthetic dataset.
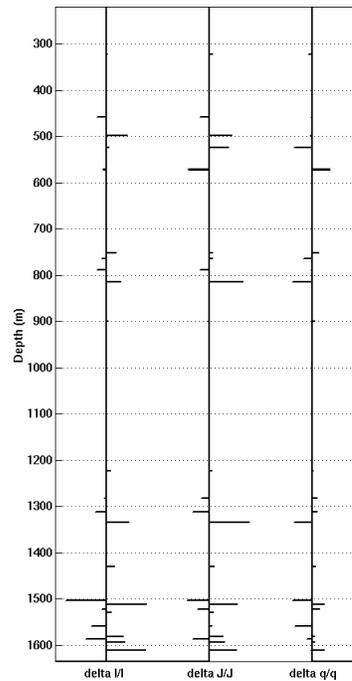
Figure 3.41b: Exact fractional values of ΔI/I, ΔJ/J and Δq/q (lower) computed directly from well logs.

3.6.3 Blackfoot synthetic study with added noise

As shown previously, the simultaneous inversion method has advantages in improving the signal-to-noise of impedance estimates in a single-layer reflectivity case. The next step is to compare the P-P and simultaneous inversion methods by utilizing band-limited synthetic data with added noise. These sets of tests were constructed using the same weights as the previous section with the only difference being the amount of noise added. This noise is derived using the Matlab function RNOISE, which computes noise defined in the time-domain by measuring the RMS power of the input signal and scaling a set of pseudo-random numbers to have a user-input RMS signal-to-noise ratio. The strength of this noise is based upon the RMS amplitude of all traces in the entire offset gather. This noise is also distributed normally about the entire offset gather.
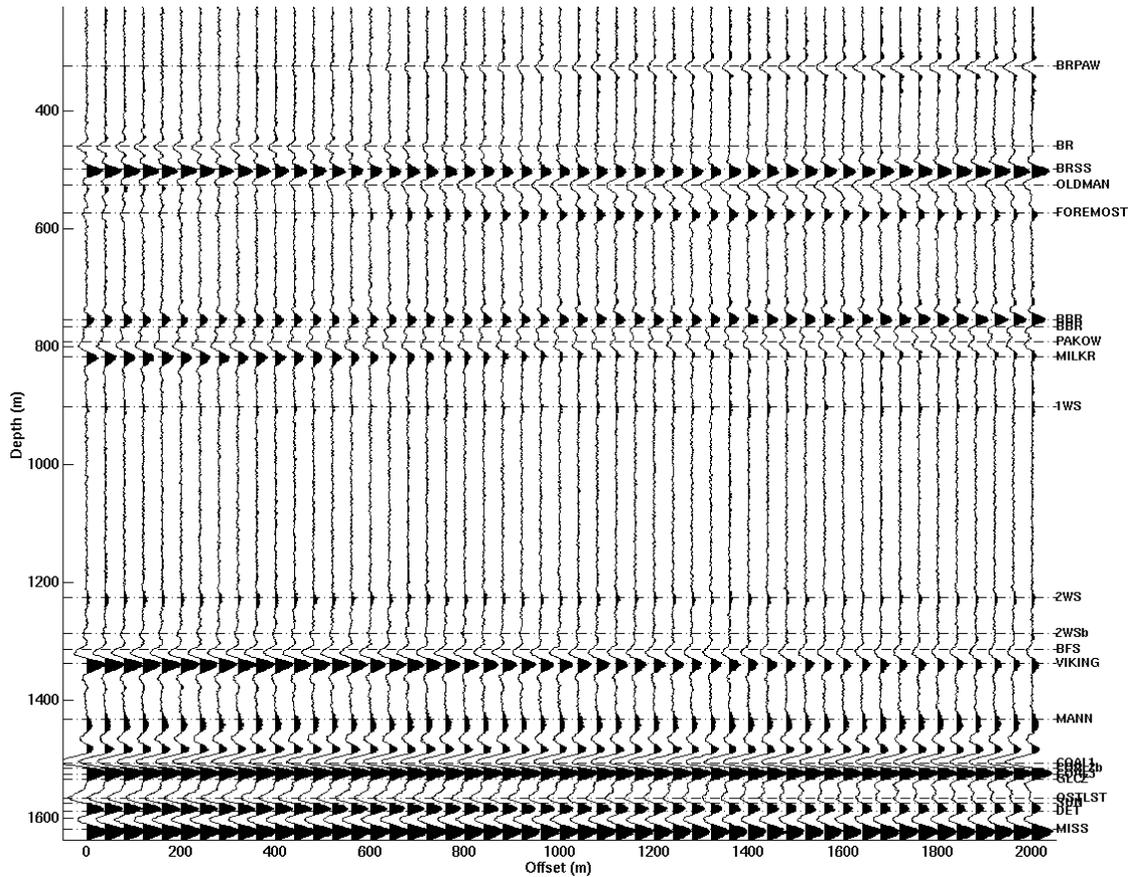
Figure 3.42: P-P offset synthetic with pseudo-random noise added. The RMS signal-to-noise ratio equals 5 and is defined over the entire offset gather.

Once the noise is calculated, it is then added to the noise-free, synthetic offset gather to obtain the data shown in figures 3.42 and 3.43. The application of the weighting procedure is now straightforward and may be performed in the same manner as previously discussed.

As in the previous section, it is important to consider the polarity of the input seismic data. In the case of this study, a positive reflection coefficient results in a shaded peak and a negative reflection coefficient results in a trough. Again, no attempt was made to mute data at far offset in the near-surface since the target of interest is at a significantly greater depth.
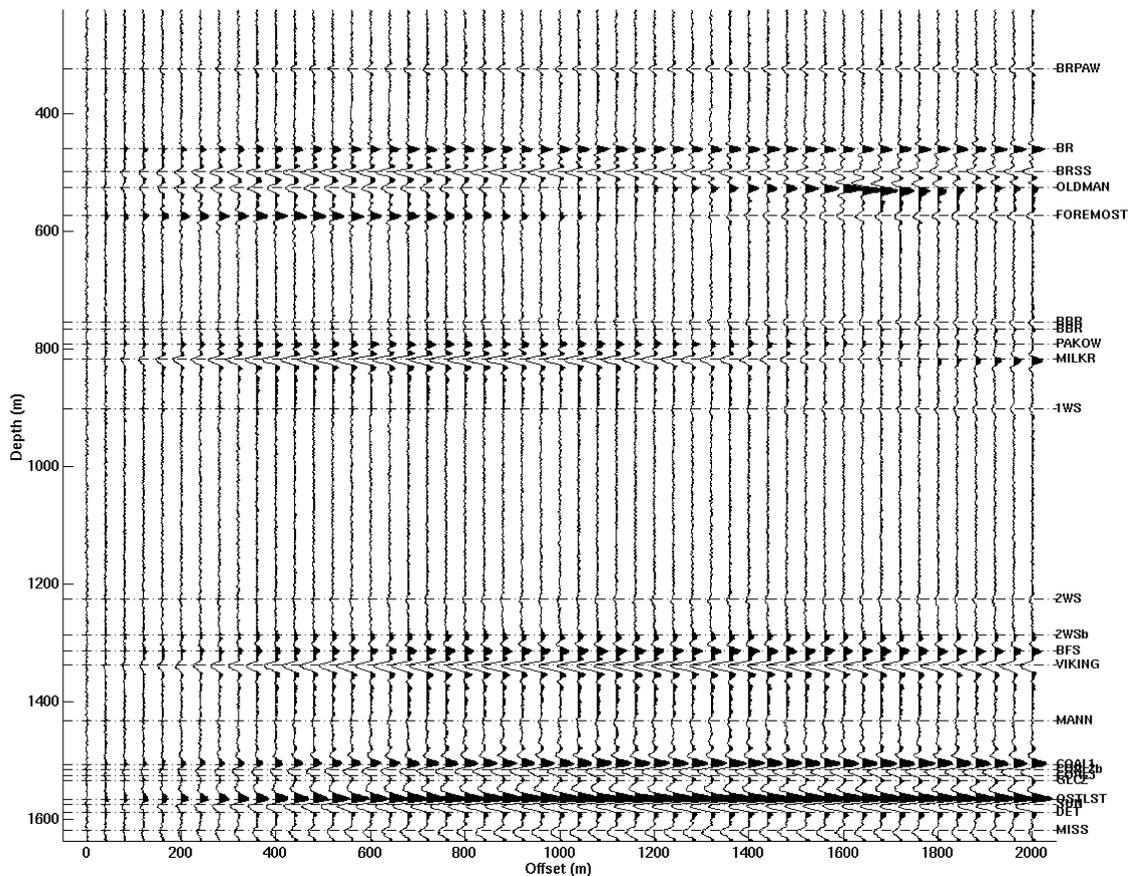
Figure 3.43: P-S offset synthetic with pseudo-random noise added. The RMS signal-to-noise ratio equals 5 and is defined over the entire offset gather.

The results of the weighted stacking procedure as shown in figure 3.44 show the simultaneous inversion method provides less noisy impedance estimates than the P-P inversion method. The ideal bandlimited, noise-free inversion results are shown in figure 3.45. Notice the traces in figure 3.44 indicated by 2 and 3 that represent the $\Delta J/J$ estimates for the P-P and simultaneous inversion methods respectively show significantly different levels of noise. This increase in noise suppression using the simultaneous inversion method as observed previously is due to both the greater amount of data used to derive each impedance estimate and a different weighting method. Notice the stacked section traces numbered 6 and 7 show the least amount of noise due to their ideal weighting, i.e. each offset is equally weighted. The same observation can be made on the

simultaneous inversion traces (2, 4 and 6) near the maximum depth of the synthetic recording where the weights are nearly equal over all offsets.

0 - ΔI/I weighted stack using P-P method, 1 - ΔI/I weighted stack using the simultaneous inversion method
2 - ΔJ/J weighted stack using P-P method, 3 - ΔJ/J weighted stack using the simultaneous inversion method
4 - Δq/q weighted stack using the P-P method, 5 - Δq/q weighted stack using the simultaneous inversion method, 6 – P-P stacked trace, 7 – P-S stacked trace

Figure 3.44: Inversion results using the previously calculated weights and the offset gathers from figures 3.42 and 3.43. Notice the greater noise level obtained using the P-P method compared with the simultaneous inversion method.
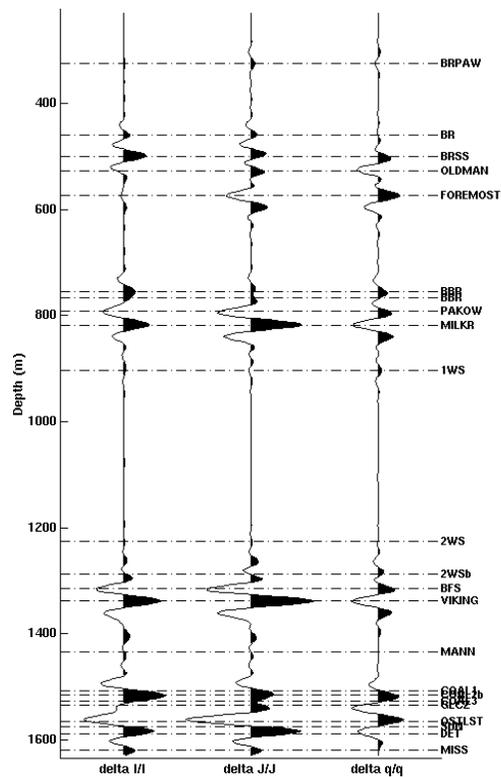
Figure 3.45: Exact bandlimited inversion results in the noise free case computed directly from well logs at the 09-17 regional well location.

A similar set of noisy P-P and P-S offset gathers was next constructed with an RMS signal-to-noise ratio of 3. Again, this noise was designed using the Matlab function RNOISE using the RMS amplitudes of the entire offset gather as the basis for the scaling of the pseudo-random noise. The results of the weighted stack for the noisy P-P and P-S offset gathers are shown in figure 3.46. The same observations can be made regarding signal-to-noise improvements using the simultaneous inversion method.
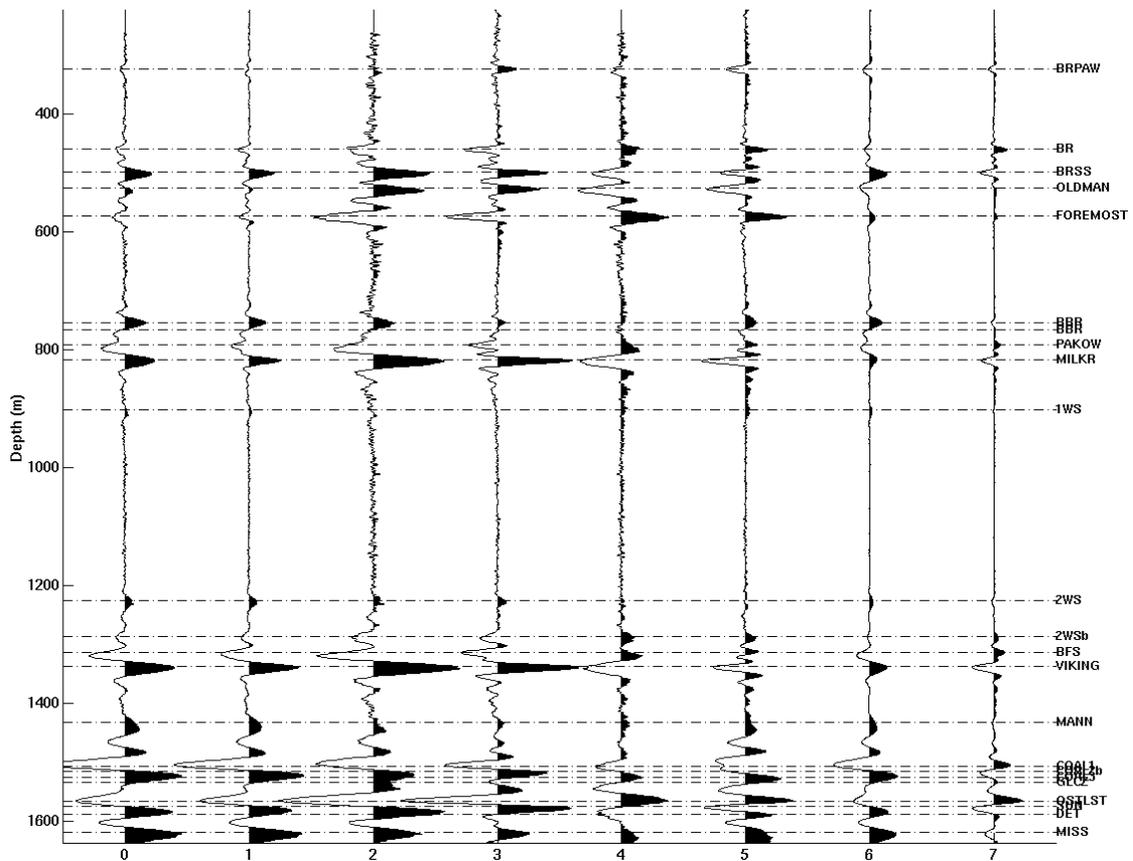
0 - $\Delta I/I$ weighted stack using P-P method, 1 - $\Delta I/I$ weighted stack using the simultaneous inversion method
2 - $\Delta J/J$ weighted stack using P-P method, 3 - $\Delta J/J$ weighted stack using the simultaneous inversion method
4 - $\Delta q/q$ weighted stack using the P-P method, 5 - $\Delta q/q$ weighted stack using the simultaneous inversion method, 6 – P-P stacked trace, 7 – P-S stacked trace

Figure 3.46: Inversion results using the previously calculated weights and P-P and P-S offset gathers with an RMS signal-to-noise ratio of 3.

3.7 Further sources of error

The results from the previous section show the simultaneous inversion method is accurate for a complex 1-D input model with noise and elastic parameter changes which exceed the assumptions made in the Zoeppritz equation approximations. These sets of tests incorporated a well-constrained background velocity-depth model and a set of ideally processed P-P and P-S offset gathers. In the case of real data these parameters may not be known in such detail, consequently several important points should be made regarding the application of the simultaneous inversion method to field seismic data.

3.7.1 Event correlation

One of the most important sources of error in using the simultaneous inversion method is the problem of correlating P-P and P-S reflection events in time or depth. In the set of tests conducted in section 3.6, the exact velocity-depth model was known, and used to correlate the P-P and P-S synthetic sections in depth. In the case of field data, a gross P-wave velocity-depth model is generally known, however shear velocity control is often limited. A number of methods are available to estimate a shear velocity model.

The simplest method is to assume a constant V_P/V_S ratio and correlate the P-P and P-S sections directly from a common datum. The first problem with this method is the difficulty with P-S refraction statics analysis that prevents the P-P and P-S datasets from being referenced to the same datum. The second problem with this assumption is, as discussed in chapter 1, V_P/V_S varies significantly with lithology and pore fluid content. Of even greater concern is the extreme variation in the V_P/V_S ratio with proximity to the near surface or in unconsolidated sediments.

Another simple method is to apply the "low-frequency compression" of P-S time to P-P time using the ARCO mudrock line relating compressional and shear velocity. It can be shown the mudrock line gives a good approximation for V_P/V_S especially in brine-saturated, relatively unconsolidated sand and shale sequences. Again the problem with P-S refraction analysis prevents this method from providing an accurate correlation datum between the P-P and P-S sections. This method also fails in areas where the mudrock line is not applicable or is inaccurate due to local variations in lithology or pore fluid content. This method does however provide a dynamic correlation between the P-P and P-S sections.

Ferguson and Stewart (1996) outline a method of using P-S stacking velocities to estimate shear interval velocities. This method assumes an equivalent relationship between P-S stacking, and RMS velocities. It was shown this method is reliable in providing shear interval velocity estimates for both synthetic and field data. The primary difficulty with this method is the assumption that P-S stacking velocities are equivalent to RMS velocities. It can be shown that this assumption is highly accurate for small offsets

(Ferguson and Stewart, 1996). This method has the advantage of being data driven rather than driven by an empirical relationship that may or may not be applicable in a given area.

A common method for correlating P-P and P-S sections is an interpretive approach where the P-S time stretch factor is derived by matching picked events on P-P and P-S sections. A simple relationship used to relate interval V_P/V_S and P-P and P-S traveltimes is summarized as follows:

$$\gamma = \frac{\alpha}{\beta} = \left(\frac{2T_{PS} - T_{PP}}{T_{PP}} \right)$$
(3.5)

where T_{PP} and T_{PS} equal P-P and P-S one-way (or two-way) traveltimes respectively between two picked events. Assuming proper phase corrections to the P-P and P-S datasets, this method provides a reliable method for estimating V_P/V_S ratios and thus the P-S time stretch factors used to correlate the these two datasets. This method has the advantage of being completely independent of lithological assumptions such as the mudrock line. The disadvantage of this method is the need to rely upon accurate event identification using synthetic seismograms, thus good well control is needed. Also, because an event is picked on a specific point of phase, these events in P-P and P-S data will generally not tie in depth.

Chan and Stewart (1997) describe a method for correlating P-P and P-S sections in the logarithmic time domain. This method converts P-P and P-S sections to logarithmic traveltime and derives a P-S traveltime stretch factor for a given picked interval. These sections are converted to the linear traveltime domain and the P-S stretch factor is then applied to correlate the P-P and P-S sections.

Additional methods of correlating P-P and P-S events may be possible using a Vertical Seismic Profile (VSP) to make an in-situ determination of a velocity-depth model. This velocity-depth model would allow events on P-P and P-S sections to be converted to depth and correlated relative to a common datum. Pre-stack depth migration should also be considered as a possibility since a common velocity-depth model and

recording datum are used for the vertical and radial component datasets. Pre-stack depth migration should result in an exact correlation between P-P and P-S reflection events assuming proper steps are taken to ensure a reasonably accurate velocity-depth model is used and correct phase is maintained for both datasets.

3.7.2 Phase and polarity errors

It is important to consider both the polarity and phase of the input seismic data prior to applying the simultaneous inversion method. A consistent set of polarity conventions (Sheriff, 1991) should be maintained between the P-P and P-S seismic data. A simple procedure for checking for consistent polarity is to observe the polarity at near-zero offset. For instance, a positive compressional impedance contrast at near-zero offset should result in a positive polarity on the P-P dataset and a positive shear impedance contrast at near-zero offset should result in a positive polarity on the P-S dataset. Phase error are more difficult to predict and will be discussed in the next chapter.

3.8 Chapter summary

The previous sections have outlined a number of tests and comparisons between the simultaneous inversion method and the "Geostack" method utilizing P-P seismic data only. The simultaneous inversion method has been shown to weight each offset differently than the Geostack method. This difference in weighting behavior with offset has important implications in the suppression of random noise. The simultaneous inversion method was then applied to well log data from the Blackfoot field. The results of this test show that the simultaneous inversion method and the Geostack method give similar results for noise-free seismic data with similar temporal bandwidth. A similar set of tests was then conducted using synthetic data containing varying levels of noise. The results of these tests show the simultaneous inversion method gives superior noise-suppression characteristics compared to the P-P only inversion method. Finally, several sources of error specific to the simultaneous inversion method are discussed. It should now be possible to apply these inversion methods to multi-component field seismic data.

CHAPTER 4

Blackfoot 3C-3D case study

4.1 Introduction

Chapters 2 and 3 outline a least-squares, linearized, simultaneous inversion method in which band-limited P-P and P-S seismic data can be inverted to provide broadband estimates of compressional and shear impedance. In this chapter, the simultaneous inversion method is applied to a previously acquired and processed 3C-3D dataset. This procedure consists of several steps. The first is to obtain and process the 3C-3D seismic data to obtain quality, true-amplitude offset seismic data volumes. The second is to correlate P-P and P-S reflection events in depth or traveltime. The final step is to weight each offset data volume by a set of model-based weights and thus, compute the weighted reflectivity stack resulting in band-limited estimates of compressional and shear reflectivity.

4.2 Preparation of P-P and P-S pre-stack data

Several steps must be taken prior to applying the simultaneous weighted stacking procedure. The first is to acquire and process the 3C seismic data in a true-amplitude manner. Careful attention must be made in maintaining the correct phase and polarity of the processed seismic gathers.

4.2.1. Seismic processing

In November 1995, a 3C-3D survey was conducted over the Blackfoot field in Southern Alberta. The initial seismic processing was performed by Pulsonic Geophysical and Sensor Geophysical in 1996. The Blackfoot 3C-3D was then reprocessed in 1998/1999 to improve the signal-band and signal-to-noise over previous versions (Lu and Margrave, 1998). Careful attention in this case was paid to the large source and receiver statics present in the radial component dataset. To solve this problem, the common receiver stack method was used. This method allows for the correction of large receiver statics, but is restricted to areas with small lateral changes in reflector time. After removing these large receiver statics, a surface-consistent method was used to eliminate residual source and receiver statics. Processing flows for vertical and radial components are given in tables 4.1 and 4.2 respectively.

SEG-D FORMATTED DE-MULTIPLEX INPUT
3D GEOMETRY ASSIGNMENT
TRACE EDIT
TRUE AMPLITUDE RECOVERY
SURFACE CONSISTENT DECONVOLUTION
TIME VARIANT SPECTRAL WHITENING
ELEVATION AND REFRACTION STATICS CORRECTIONS
VELOCITY ANALYSIS
RESIDUAL SURFACE CONSISTENT STATICS
NORMAL MOVEOUT
TRIM STATICS
FRONT END MUTING
CDP STACK
TIME VARIANT SPECTRAL WHITENING
TRACE EQUALIZATION
F-XY DECONVOLUTION
3D PHASE-SHIFT MIGRATION

Table 4.1: Processing flow for vertical component data. (Lu and Margrave, 1998)

SEG-D FORMATTED DE-MULTIPLEX INPUT
COMPONENTS SEPARATION
3D GEOMETRY ASSIGNMENT
TRACE EDIT
ASYMPTOTIC BINNING
SURFACE CONSISTENT DECONVOLUTION
TIME VARIANT SPECTRAL WHITENING
ELEVATION STATICS
FINAL REFRACTION AND RESIDUAL STATICS FROM P-P
CONSTRUCT INITIAL P-SV VELOCITY FROM FINAL P-P VELOCITY

VELOCITY ANALYSIS
RECEIVER RESIDUAL STATICS
VELOCITY ANALYSIS
CONVENTIONAL RESIDUAL STATICS
VELOCITY ANALYSIS
NORMAL MOVEOUT
ACP TRIM STATICS
FRONT END MUTING
ACP STACK (DEPTH-VARIANT STACK AND DMO STACK)
TIME VARIANT SPECTRAL WHITENENING
TRACE EQUALIZATION
F-XY DECONVOLUTION
3D PHASE SHIFT MIGRATION

Table 4.2: Processing sequence for radial component data. (Lu and Margrave, 1998).

In order to decrease the amount of data needed for AVO analysis, a simple limited-offset stacking procedure was used for the vertical and radial component datasets. The offset ranges for the P-P and P-S datasets at the depth of the Glauconitic channel are given in table 4.3.

P-P OFFSET RANGE (m)	P-S OFFSET RANGE (m)	NAMING CONVENTION
0-450	0-700	NEAR
225-675	350-1050	MID-NEAR
450-900	700-1400	MID
675-1135	1050-1750	MID-FAR
900-1350	1400-2100	FAR

Table 4.3: Offset ranges used to construct limited-offset stacks at the depth of the Glauconitic channel.

As shown in chapter 3, the effect of limited offset stacking on inversion accuracy for data with a high signal-to-noise ratio is negligible. Inversion accuracy for limited-offset stacked data is a function of both the number of offsets used, and the amount of noise present in the data.

As discussed in chapter 2, the Zoeppritz equations and the Zoeppritz equation approximations assume plane waves. This assumption is generally considered to be valid at great distances from the seismic source. Treitel et al. (1981) discusses a method of

decomposing a point source recording into a set of plane wave seismograms for arbitrary angles of incidence. This method should allow for field seismic data to be considered as approximately plane wave.

4.2.2 Amplitude correction

In order to obtain true reflectivity amplitudes on data which have a statistical amplitude recovery applied (Automatic Gain Control), a simple inverse procedure was used. This procedure involved the use of the SYNTH algorithm (Lawton and Howell, 1992; Margrave and Foltinek, 1995) to compute average expected amplitude behavior from dipole sonic information. The following formulae have been applied to correct each dataset

$$R_{PP}(t,h) = \frac{\int_0^{T_{max}} \left| S_{model\,PP}(t',h) \right| dt'}{\int_0^{T_{max}} \left| S_{data\,PP}(t',h) \right| dt'} S_{data\,PP}(t,h), \qquad (4.1)$$

$$R_{PS}(t,h) = \frac{\int_0^{T_{max}} \left| S_{model\,PS}(t',h) \right| dt'}{\int_0^{T_{max}} \left| S_{data\,PS}(t',h) \right| dt'} S_{data\,PS}(t,h), \qquad (4.2)$$

where $R_{PP}(t,h)$ and $R_{PS}(t,h)$ are the corrected reflection coefficient amplitudes at a given time (t) and offset (h), $S_{dataPP}(t,h)$ and $S_{dataPS}(t,h)$ are the reflection coefficient inputs from a trace equalized time sample, and $S_{modelPP}(t,h)$ and $S_{modelPS}(t,h)$ are calculated model-based reflection coefficient amplitudes from the SYNTH algorithm. Each trace as a result has the same time-averaged amplitude as the synthetic.

4.3 Event correlation

The process of correlating P-P and P-S events in depth or P-P traveltime in this study follows a relatively simple procedure. Table 4.4 describes the method used in this study to correlate P-P and P-S events in depth.

1. Pick a common, easily identifiable regional horizon relatively free of thin-bed tuning effects or phase distortions above the presumed channel zone.

2. Flatten both P-P and P-S limited offset data volumes relative to the horizon obtained in step 1.

3. Output limited-offset time slices relative to the flattened horizon in intervals of 2ms (the data sample interval) trough the presumed channel zone.

4. Compute a smoothed time-depth model using full-waveform sonic logs in the channel zone for P-wave and converted wave zero-offset traveltimes.

5. Linearly interpolate reflection events on the P-P and P-S offset sections using the previously obtained time-depth model.

Table 4.4: Method used to correlate P-P and P-S reflection events in depth.

The method outlined in table 4.4 follows a relatively simple procedure that relies upon accurate picking by the user to define a common reflection event used to correlate the P-P and P-S offset sections. This method requires a common P-P and P-S reflection horizon relatively free of tuning effects or other phase conditions that may affect picking accuracy. This method can only be used for a limited depth interval but has the advantage of being relatively unaffected by source-receiver or residual statics problems. Given a sufficiently detailed velocity-depth model, both P-P and P-S offset sections can be converted to depth and directly correlated relative to a common datum or horizon.

Perhaps a more robust method of correlating P-P and P-S timeslices is to compute an amplitude envelope over a set of timeslices for each P-P and P-S dataset and correlate the result. This method may also reduce errors in the inversion result due to incorrect phase in the input P-P and P-S offset sections.

4.4 Computation of weights for limited-offset stacks

The calculation of weights for the P-P and P-S limited offset stacks is a straightforward procedure. Using the same set of model-based weights described in chapter 3 for the Blackfoot field, a set of limited-offset weights were calculated for each limited-offset stack. These weights were calculated for each offset via raytracing through a smoothed V_P and V_S velocity model as described previously and averaged over the entire offset range of each limited-offset P-P and P-S dataset.

4.5 Results from the Blackfoot field

The Blackfoot field is located approximately 30km east-south-east of the town of Strathmore as shown in figure 4.1. As discussed in chapter 3, the primary target of interest in the Blackfoot field are the lower Cretaceous age, Glauconitic sandstone incised valley deposits. These incised valley deposits generally trend in a north-south direction as shown in figure 4.2.
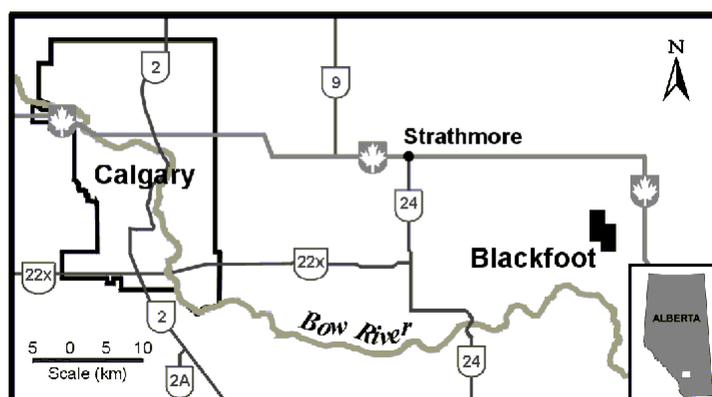
Figure 4.1: Area map showing the location of the Blackfoot 3C-3D survey.

Of special interest in this study is the presence of reservoir gas in the upper Glauconitic incised valley. As shown in figure 3.23, the upper incised valley shows a characteristic strong negative compressional impedance anomaly and a relatively weak positive shear impedance anomaly. This anomaly results in a strong P-P AVO response and a relatively weak P-S AVO response.

Since several cycles of valley incision may occur in the area of study, multiple hydrocarbon prospects are possible within the Glauconitic incised valley system. Figure 4.3 shows the three main incised valley fills; the Upper Valley (40), Lithic Valley (35) and Lower Valley (30).
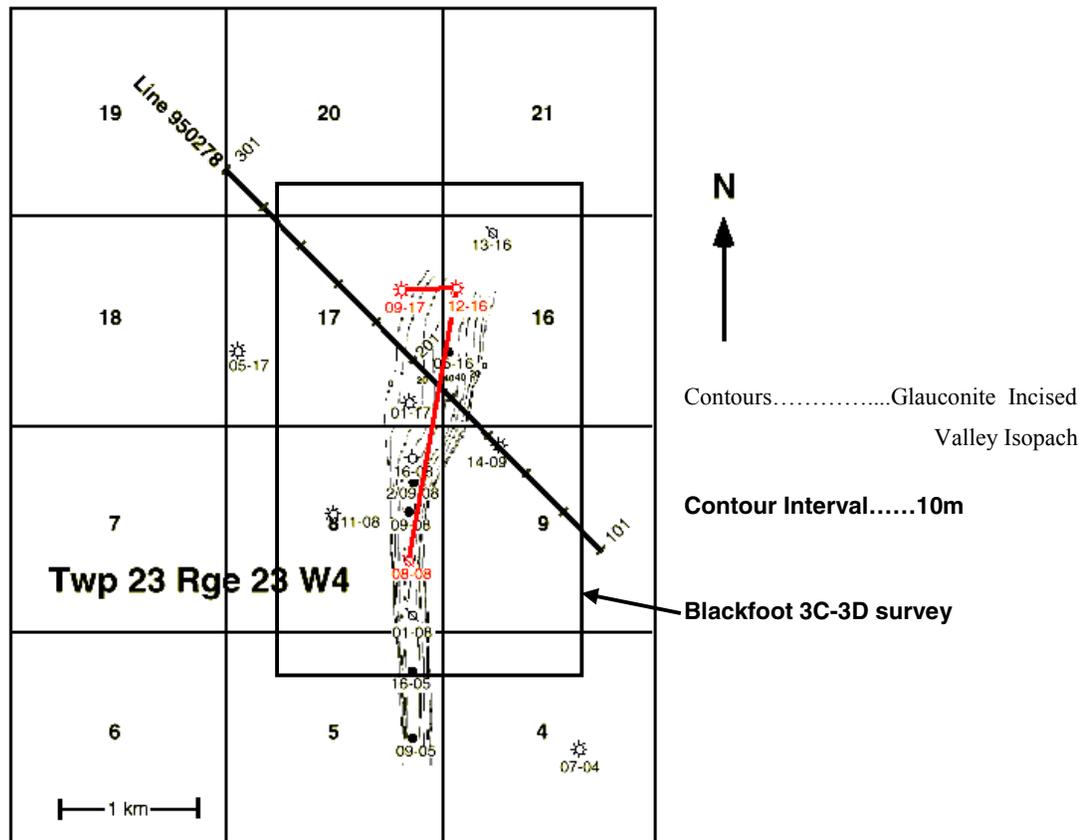
Figure 4.2: Glauconitic incised valley isopach from the Blackfoot field (Modified from Miller, 1996).

Figure 4.4 shows a vertical channel timeslice (full offset stack) at the depth of the top of the Upper incised valley. An apparent negative reflectivity anomaly exists in the area between wells 16-08 and 09-08. Figures 4.5, 4.6, 4.7, 4.8, 4.9 and 4.10 show inline and crossline views of the vertical and radial component datasets flattened at the lower Mannville marker. The Upper Valley top is apparent at approximately 10ms and 15ms below the Lower Mannville marker for the vertical and radial component datasets respectively. Notice the radial component dataset has a lower temporal resolution than the comparable vertical component dataset. Both section types have approximately the same resolution in depth. The Upper Valley top also appears less distinct in the case of the radial component dataset.
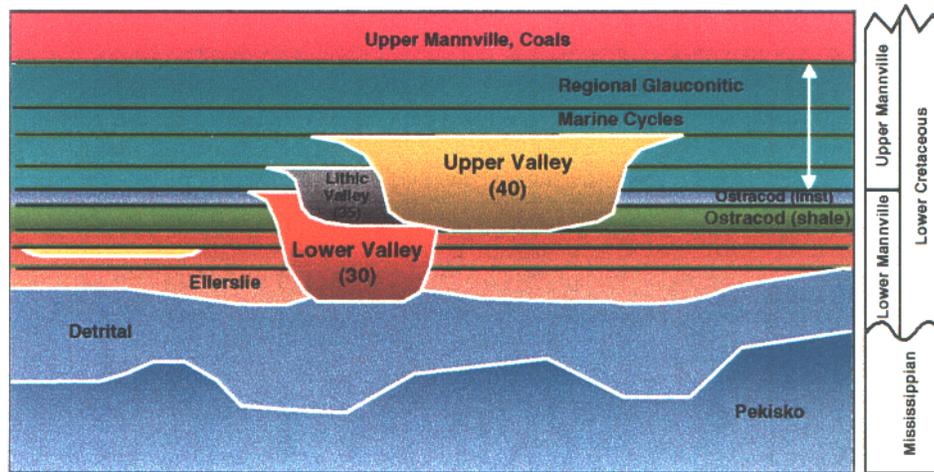
Figure 4.3: Schematic stratigraphy of the Blackfoot area showing three different incised valleys and the regional lithologies (Dufour et al., 1998).
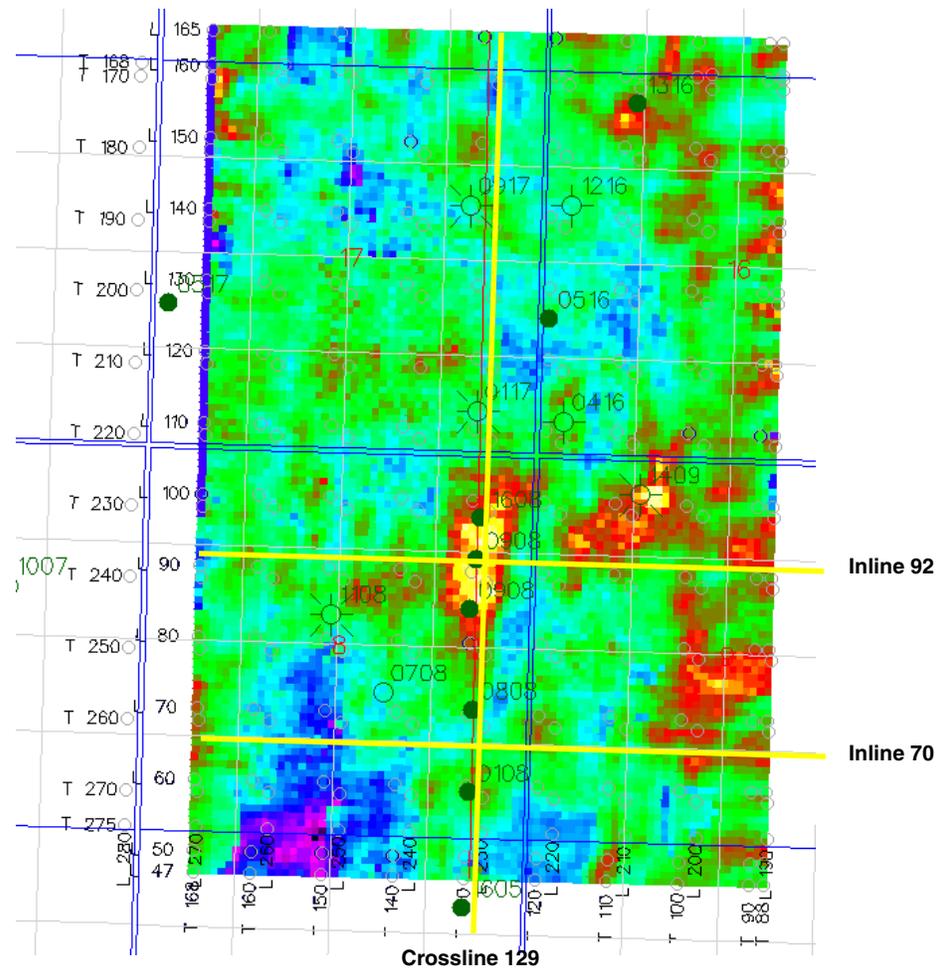
Figure 4.4: Basemap of the Blackfoot 3C-3D survey area showing the vertical component reflectivity amplitudes at the depth of the upper Glauconitic incised valley.
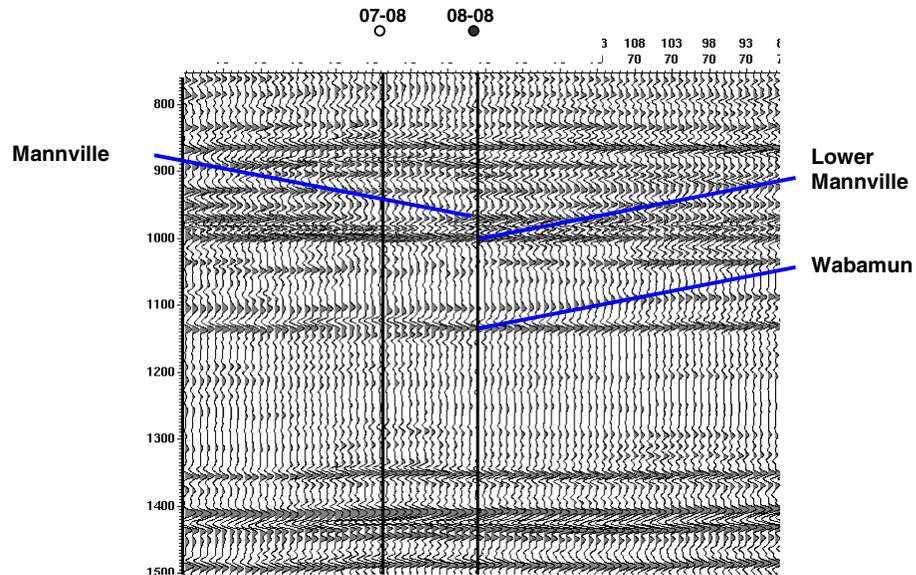
Figure 4.5: Inline 70 (vertical component) showing the presumed Glauconitic incised valley approximately 10ms below the lower Mannville marker at the 08-08 well location.
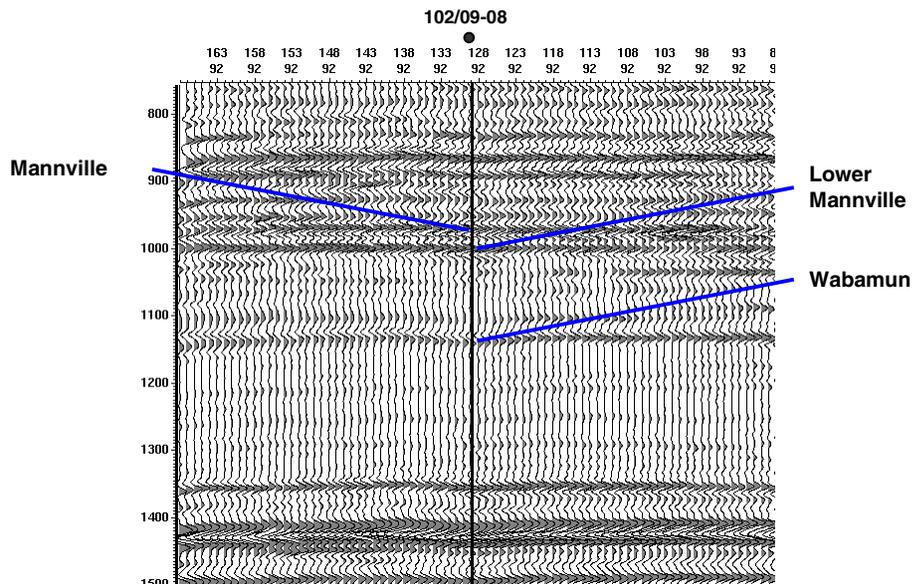
Figure 4.6: Inline 92 (vertical component) showing the presumed Glauconitic incised valley approximately 10ms below the lower Mannville marker at the 102/09-08 well location. A strong amplitude anomaly is associated with the upper channel due to the presence of reservoir gas.
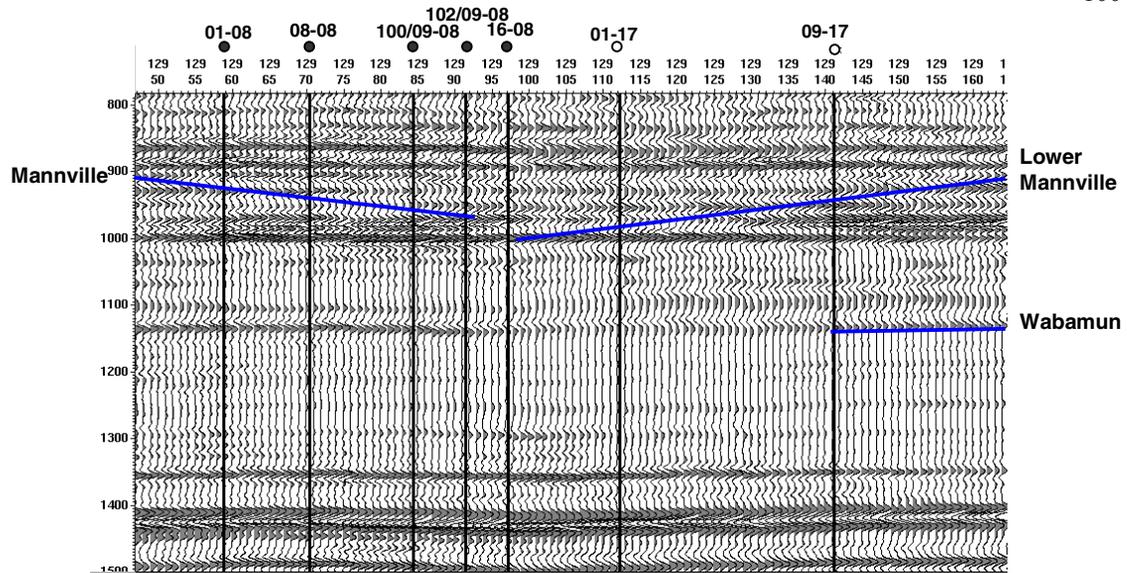
Figure 4.7: Crossline 129 (vertical component) showing the presumed Glauconitic incised valley approximately 10ms below the lower Mannville marker at the 01-08, 08-08, 100/09-08, 102/09-08 and 16-08 well locations.

Timeslices at the Upper incised-valley and the Lower incised-valley boundary are shown in figures 4.11 and 4.12 respectively for both vertical and radial component datasets. Well locations indicated with a solid black dot represent oil wells, white dots represent dry holes in shale plugged or regional well locations. Notice the apparent P-P reflectivity anomaly on both vertical component timeslices in figures 4.11 and 4.12. Both figures show a "geometrical footprint" on the radial component datasets. These geometrical footprints are an imprint of the acquisition geometry of the 3C-3D survey.
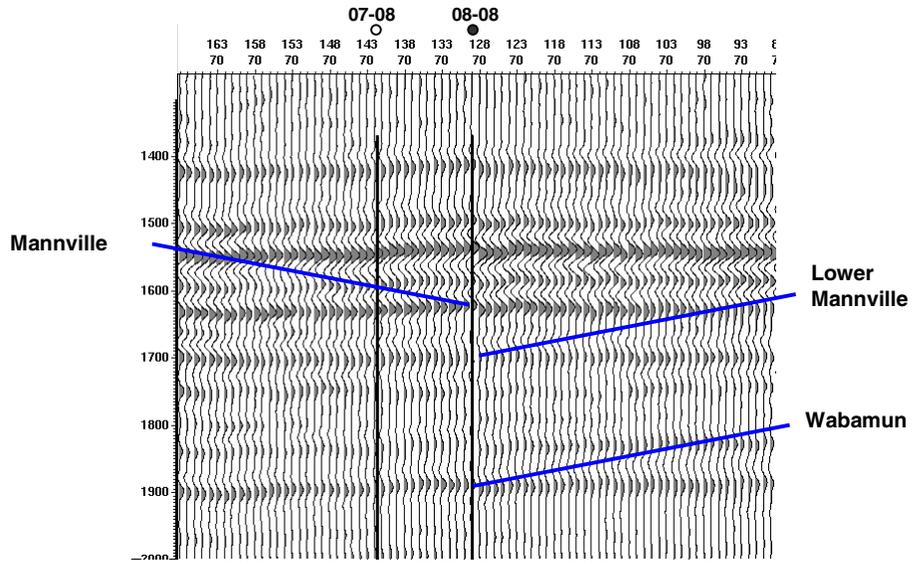
Figure 4.8: Inline 70 (radial component) showing the presumed Glauconitic incised valley approximately 15ms below the lower Mannville marker at the 08-08 well location.
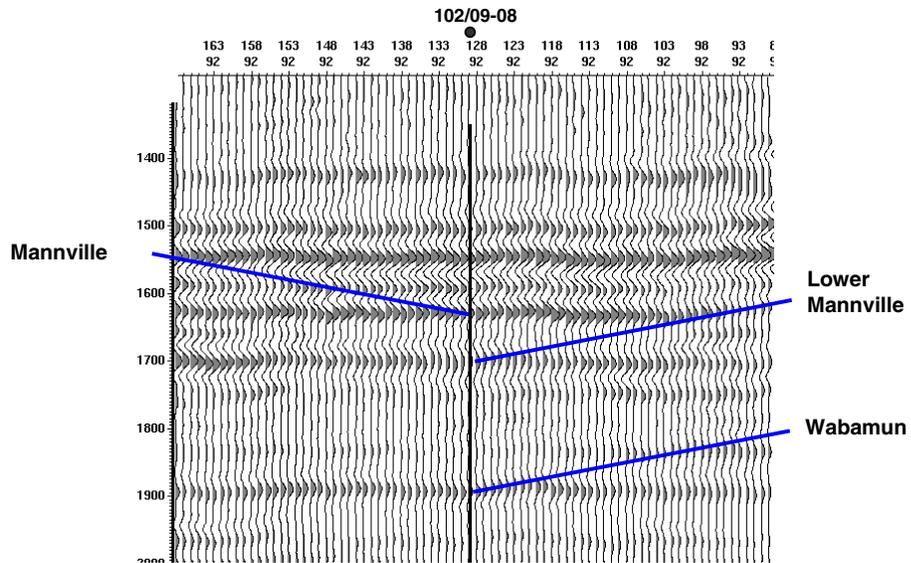

Figure 4.9: Inline 92 (radial component) showing the presumed Glauconitic incised valley approximately 15ms below the lower Mannville marker at the 102/09-08 well location.
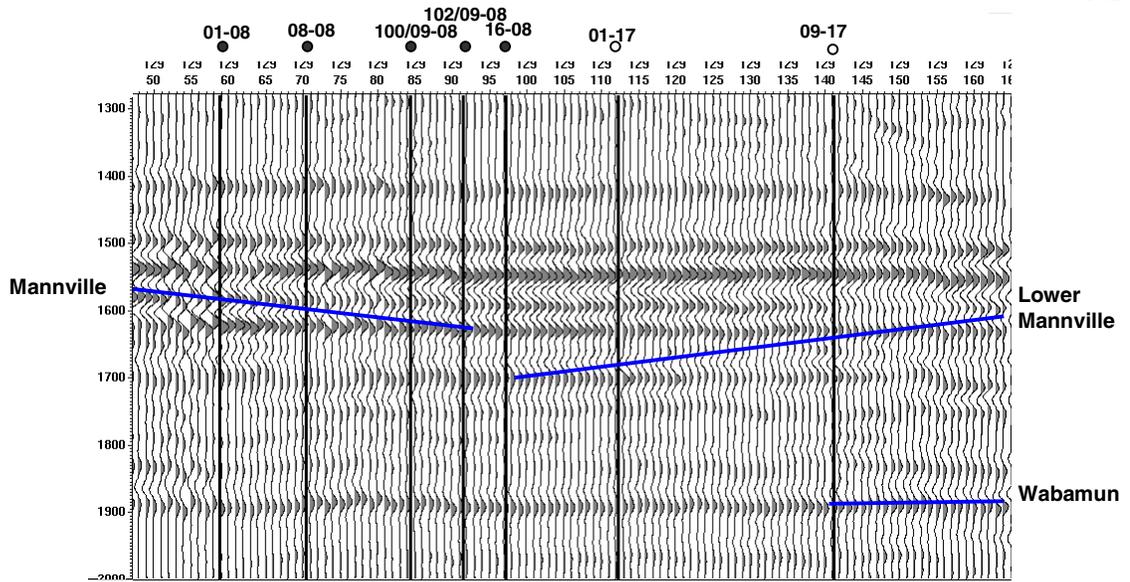
Figure 4.10: Crossline 129 (radial component) showing the presumed Glauconitic incised valley approximately 15ms below the lower Mannville marker at the 102/09-08 well location.
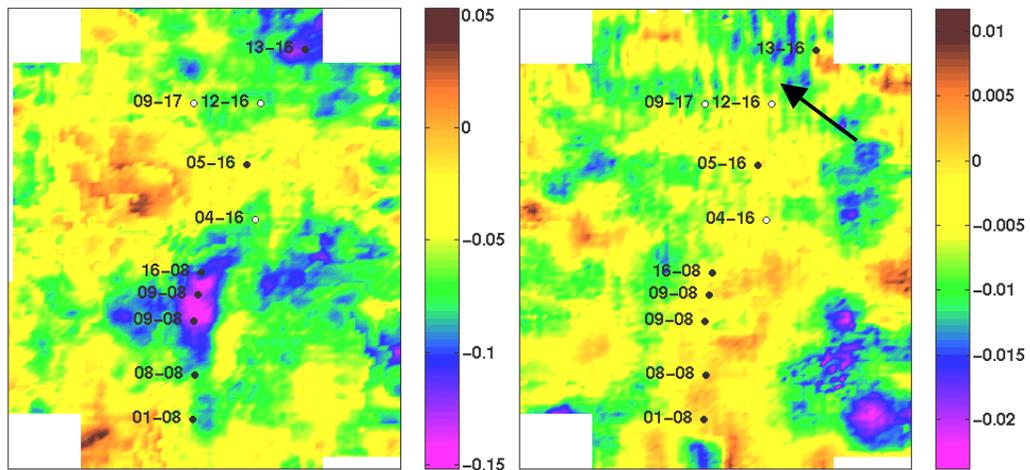
Figure 4.11: Amplitude slice of the full-offset vertical (left) and radial (right) component datasets corresponding to the upper Glauconitic channel boundary. The strong negative reflectivity anomaly on the vertical component dataset is due to the presence of reservoir gas. An arrow on the radial component dataset indicates the presence of a geometrical footprint.
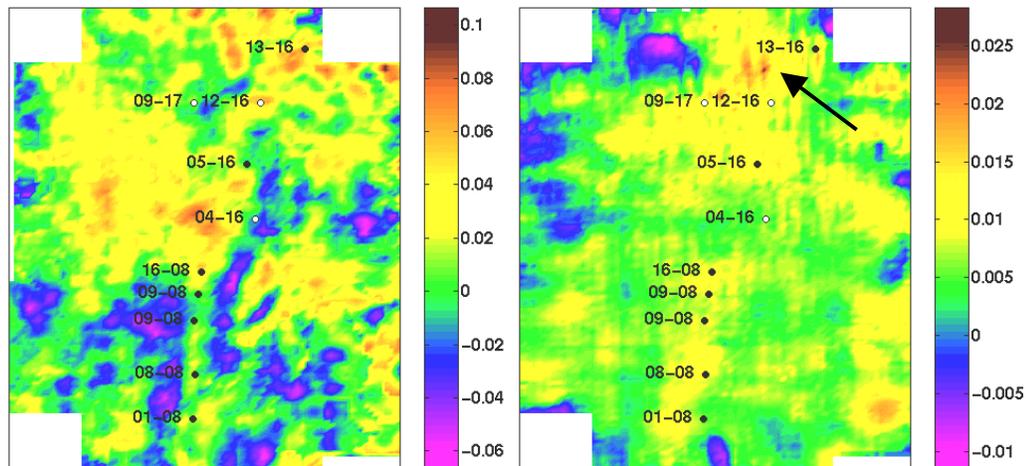
Figure 4.12: Amplitude slice of the full-offset vertical (left) and radial (right) component datasets corresponding to the base of the Glauconitic channel. An arrow on the radial component dataset indicates the presence of a geometrical footprint.

Figure 4.13 shows vertical component, limited-offset timeslices using the offsets given in table 4.3 at the Upper valley interface. Notice the correlation between increasing offset and the appearance of a negative reflectivity anomaly from the 08-08 to 16-08 well locations. Radial component, limited-offset timeslices at the Upper valley interface are shown in figure 4.14. The channel anomaly appears most distinct on the far offset possibly due to the apparent decrease in the effect of the geometrical footprint indicated earlier. The apparent channel anomaly is less distinct in the radial component dataset for several reasons. First, the radial dataset is primarily a function of P-S reflectivities and as such is more highly dependent upon shear impedance contrasts than P-P reflectivity alone. Since the shear impedance contrast is smaller than the compressional impedance contrast (as shown in figure 3.23), the anomaly should be less apparent. Second, the radial component dataset generally contains more noise than the comparable vertical component dataset. Finally, the radial component dataset is generally more affected by statics problems, phase errors and may be of reduced resolution in depth than the corresponding vertical component dataset.
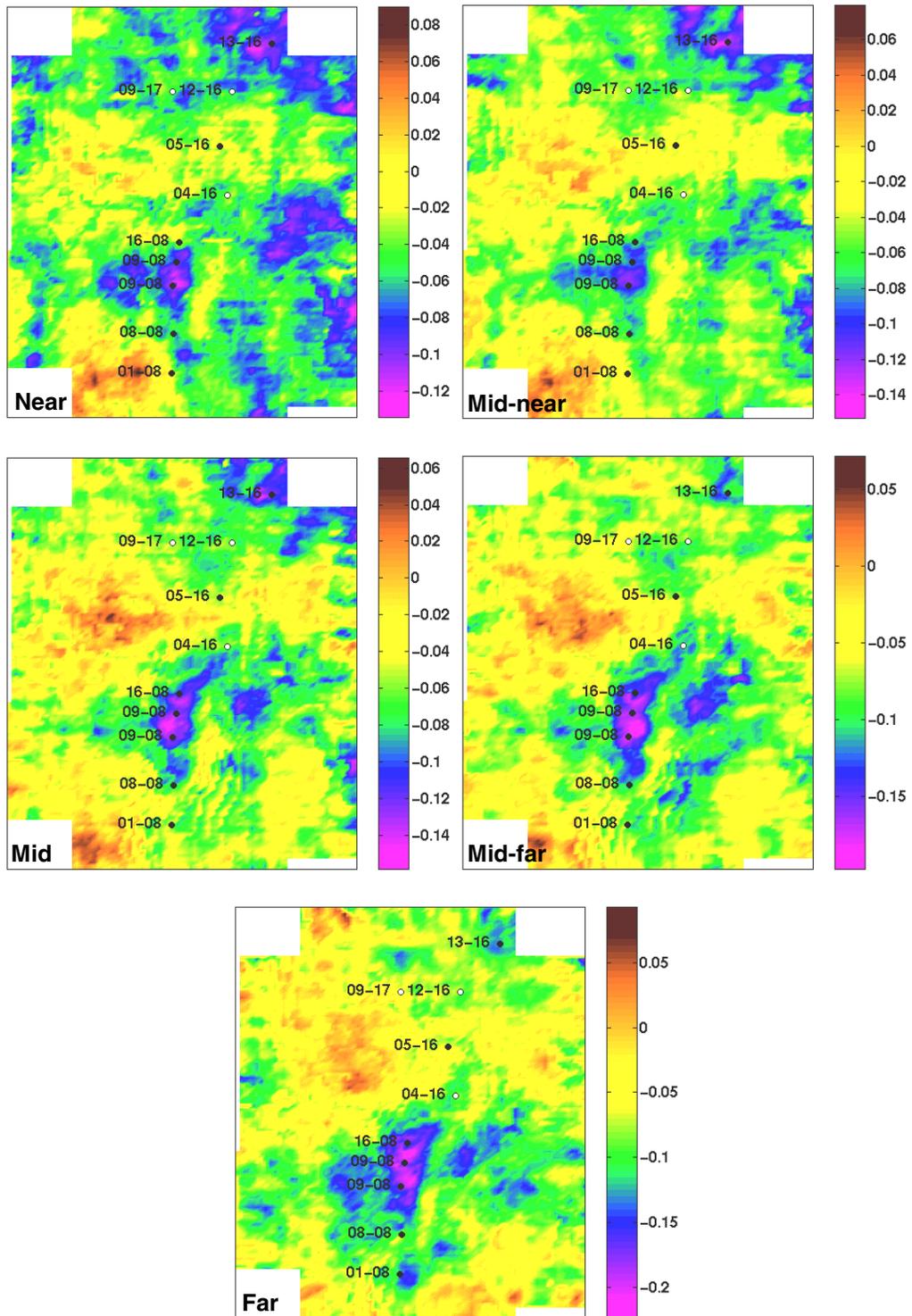
Figure 4.13: Vertical component limited-offset stacks corresponding to the upper channel zone using the offsets ranges given in table 4.3.
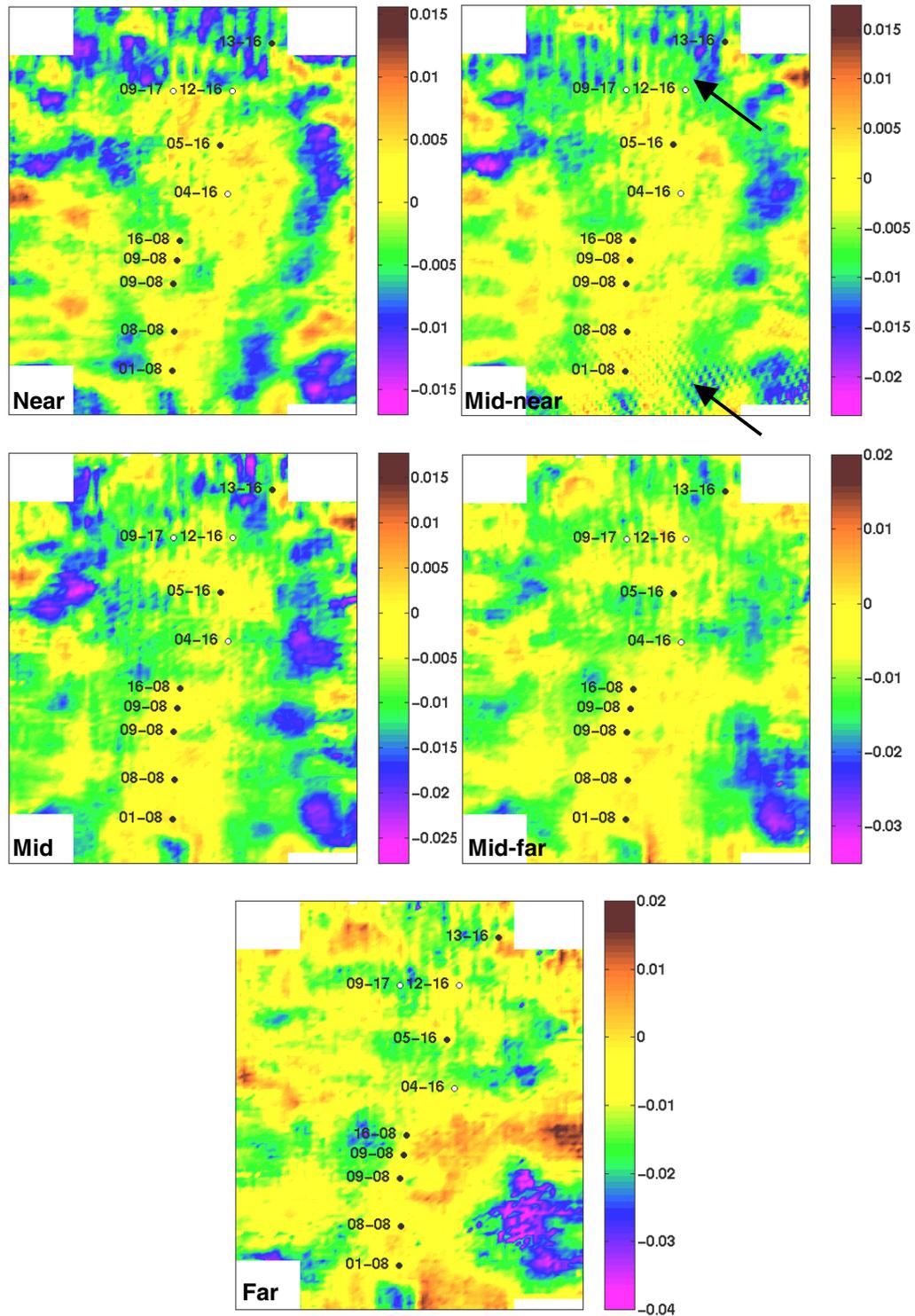
Figure 4.14: Radial component limited-offset stacks corresponding to the upper channel zone using the offset ranges given in table 4.3. A geometrical (acquisition) footprint appears most strongly at near offsets as indicated by the arrows above.

Impedance contrast estimates from the weighted stacking procedure are compared with well control in table 4.5 for the Upper incised valley interface. Results were obtained by directly computing results from blocked well logs and from the P-P and simultaneous inversion methods. Table 4.6 shows the RMS error values obtained from the data in table 4.5 for each elastic parameter contrast. The simultaneous inversion method shows a smaller RMS error than the P-P inversion method for each elastic parameter contrast.

Figures 4.15 to 4.17 show the results for the P-P and simultaneous inversion methods at the upper incised valley interface for $\Delta I/I$, $\Delta J/J$ and $\Delta q/q$ reflectivities respectively. Notice the $\Delta I/I$ reflectivity timeslice appears to better correspond with the location of the known channel anomaly using the simultaneous inversion method. The reflectivity amplitude values in figures 4.15 to 4.17 appear to more closely correspond to the theoretical values calculated from blocked well logs in table 4.5 using the simultaneous inversion method. The greatest difference between the two inversion methods is observed in figure 4.16 for the $\Delta J/J$ reflectivity.

Well	01-08[1]	08-08[1+]	09-08[1]	16-08[1]	12-16[2+]	13-16[1]	09-17[3+]	
$\Delta I/I$	-0.129	-0.141	-0.209	-0.173	-0.110	-0.175	-0.057	
$\Delta J/J$	---	0.015	---	---	-0.050	---	-0.037	
$\Delta q/q$	---	-0.156	---	---	-0.060	---	-0.020	Calculated results
$\Delta(\lambda\rho)/\lambda\rho$	---	-0.783	---	---	-0.413	---	-0.178	from blocked well
$\Delta(\mu\rho)/\mu\rho$	---	0.030	---	---	-0.100	---	-0.074	logs
$\Delta(\lambda/\mu)/(\lambda/\mu)$	---	-0.813	---	---	-0.313	---	-0.104	
$\Delta\sigma/\sigma$	---	-0.362	---	---	-0.139	---	-0.046	
$\Delta(\kappa\rho)/\kappa\rho$	---	-0.499	---	---	-0.304	---	-0.142	
$\Delta I/I$	-0.120	-0.140	-0.210	-0.124	-0.130	-0.183	-0.089	
$\Delta J/J$	-0.026	0.052	0.053	0.053	-0.048	-0.014	-0.034	
$\Delta q/q$	0.014	-0.192	-0.263	-0.177	-0.082	-0.169	-0.055	
$\Delta(\lambda\rho)/\lambda\rho$	0.021	-0.896	-1.264	-0.816	-0.523	-0.908	-0.355	P-P inversion
$\Delta(\mu\rho)/\mu\rho$	-0.052	-0.104	0.106	0.106	-0.096	-0.028	-0.068	method
$\Delta(\lambda/\mu)/(\lambda/\mu)$	0.073	-1.000	-1.370	-0.922	-0.427	-0.880	-0.287	
$\Delta\sigma/\sigma$	0.033	-0.445	-0.610	-0.410	-0.190	-0.392	-0.128	
$\Delta(\kappa\rho)/\kappa\rho$	-0.005	-0.548	-0.787	-0.495	-0.374	-0.602	-0.255	
$\Delta I/I$	-0.113	-0.138	-0.218	-0.176	-0.120	-0.177	-0.058	
$\Delta J/J$	-0.021	0.012	0.017	0.013	-0.051	-0.041	-0.040	
$\Delta q/q$	-0.092	-0.150	-0.235	-0.189	-0.069	-0.136	-0.018	
$\Delta(\lambda\rho)/\lambda\rho$	-0.521	-0.757	-1.190	-0.959	-0.461	-0.790	-0.174	Simultaneous P-P
$\Delta(\mu\rho)/\mu\rho$	-0.042	0.024	0.034	0.026	-0.102	-0.082	-0.080	and P-S inversion
$\Delta(\lambda/\mu)/(\lambda/\mu)$	-0.479	-0.781	-1.224	-0.985	-0.359	-0.708	-0.094	method
$\Delta\sigma/\sigma$	-0.213	-0.348	-0.545	-0.488	-0.160	-0.315	-0.042	
$\Delta(\kappa\rho)/\kappa\rho$	-0.354	-0.485	-0.764	-0.615	-0.336	-0.544	-0.141	

[1] Sand channel well, [2] Shale plugged channel well, [3] Regional well, [+] Includes full-waveform sonic

Table 4.5: Expected values of $\Delta I/I$, $\Delta J/J$, $\Delta q/q$, $\Delta(\lambda\rho)/\lambda\rho$, $\Delta(\mu\rho)/\mu\rho$, $\Delta(\lambda/\mu)/(\lambda/\mu)$, $\Delta\sigma/\sigma$ and $\Delta(\kappa\rho)/\kappa\rho$ from blocked sonic and density logs and each inversion method at the Upper Glauconitic incised valley interface.

	P-P inversion method	Simultaneous inversion method
$\Delta I/I$	0.0238	0.0081
$\Delta J/J$	0.0215	0.0025
$\Delta q/q$	0.0316	0.0064
$\Delta(\lambda\rho)/\lambda\rho$	0.1369	0.0316
$\Delta(\mu\rho)/\mu\rho$	0.0775	0.0050
$\Delta(\lambda/\mu)/(\lambda/\mu)$	0.1648	0.0329
$\Delta\sigma/\sigma$	0.0735	0.0148
$\Delta(\kappa\rho)/\kappa\rho$	0.0818	0.0202

Table 4.6: RMS error between each inversion method and the ideal results obtained from well logs in the survey area.

In this case the weights applied to the radial component dataset for the simultaneous inversion method are significantly different than those applied to the P-P dataset and as a result give different results from the P-P inversion method alone. Table 4.7 shows the weights applied to each limited-offset dataset at the top of the Upper incised valley. The P-P inversion weights generally change sign with increasing offset and as a result near and far offsets are differenced. In the case of the simultaneous inversion weights, the weights generally remain in the same polarity but differ only in magnitude.

	Offset	$\Delta I/I$ weights	$\Delta J/J$ weights	
P-P	Near	1.071	2.536	**P-P inversion method**
	Mid-near	0.849	1.779	
	Mid	0.487	0.533	
	Mid-far	0.056	-0.972	
	Far	-0.423	-2.685	
P-P	Near	0.365	0.248	**Simultaneous inversion method**
	Mid-near	0.354	0.174	
	Mid	0.339	0.052	
	Mid-far	0.327	-0.095	
	Far	0.325	-0.263	
P-S	Near	-0.069	-0.223	
	Mid-near	-0.133	-0.429	
	Mid	-0.185	-0.598	
	Mid-far	-0.214	-0.693	
	Far	-0.223	-0.721	

Table 4.7: Sample weights applied for each limited-offset range to the $\Delta I/I$ and $\Delta J/J$ fractional elastic parameters for each inversion method.

Figure 4.17 shows the results of the $\Delta q/q$ reflectivity (the difference between the $\Delta I/I$ and $\Delta J/J$ timeslices). In this case the two inversion methods give similar results except the simultaneous inversion timeslice appears to better contrast the known Upper incised valley anomaly. The simultaneous inversion method in this case seems to better remove the effect of the geometrical footprint on the inversion result.
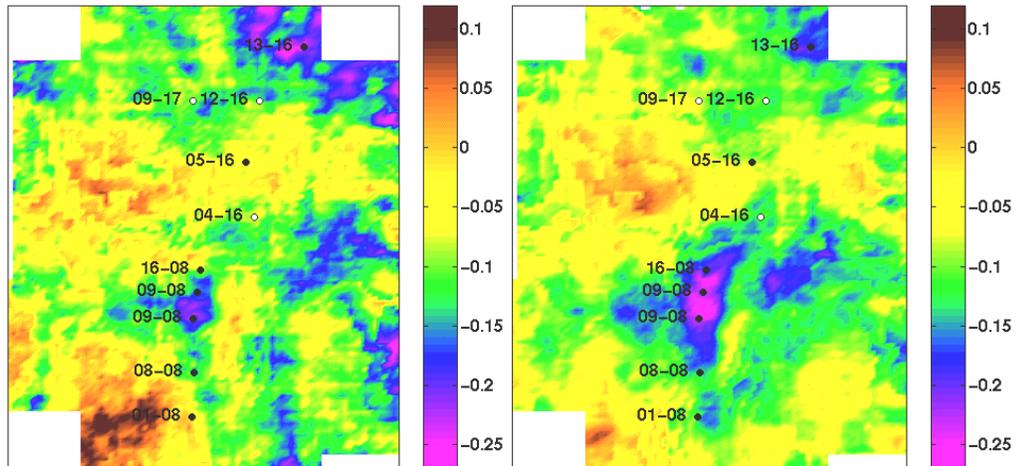
Figure 4.15: Weighted ΔI/I stacks for the P-P only (left) and simultaneous inversion methods (right) at the top of the upper Glauconitic channel.
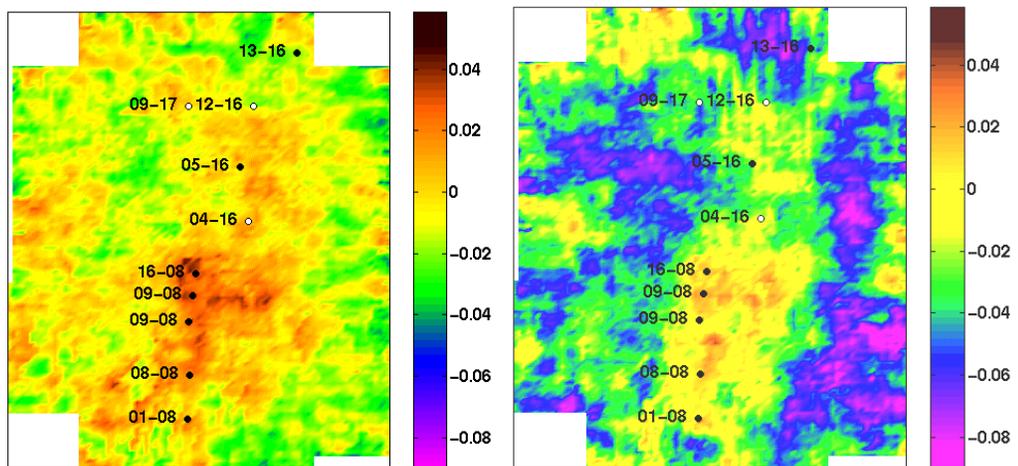
Figure 4.16: Weighted ΔJ/J stacks for the P-P only (left) and simultaneous inversion methods (right) at the top of the upper Glauconitic channel.
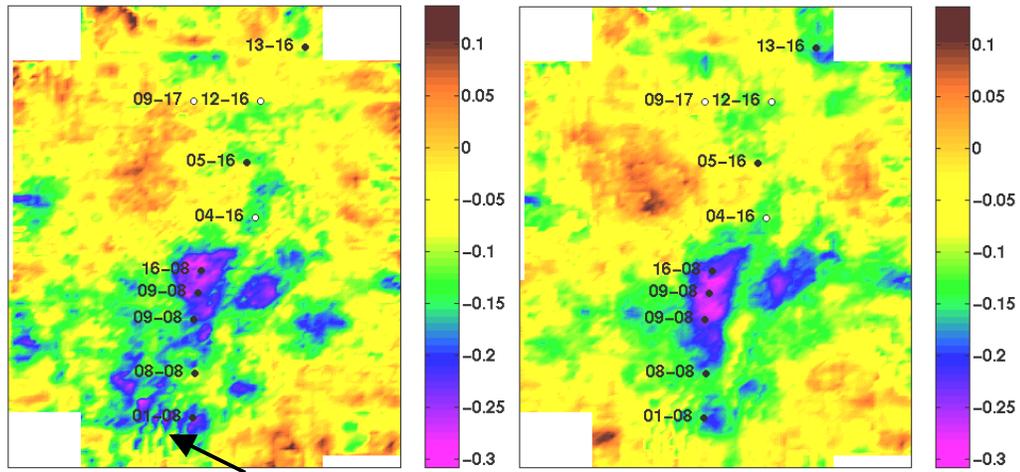
Figure 4.17: Weighted $\Delta q/q$ stacks for the P-P only (left) and simultaneous inversion methods (right) at the top of the upper Glauconitic channel. The arrow denotes the interference effect of the geometrical footprint of the input seismic data.

Figures 4.18 to 4.20 show the $\Delta I/I$, $\Delta J/J$ and $\Delta q/q$ weighted stacks at the bottom of the lower incised-valley. The $\Delta I/I$ timeslices shown in figure 4.18 show a close correspondence between the producing wells from 01-08 to 16-08 in the channel zone. The simultaneous inversion method has a general improvement in signal-to-noise over the P-P inversion method. This is likely due to the difference in weighting methods between the two inversion methods tested and the doubling of the input data fold into the simultaneous inversion method. The $\Delta J/J$ timeslices shown in figure 4.19 again show a distinct difference for the two inversion methods tested. The shear impedance anomaly should again appear less distinct than the compressional impedance anomaly as shown in figure 3.23. The $\Delta q/q$ timeslice shown in figure 4.20 appears to better define the incised-valley fill associated with the producing well locations from 01-08 to 16-08.
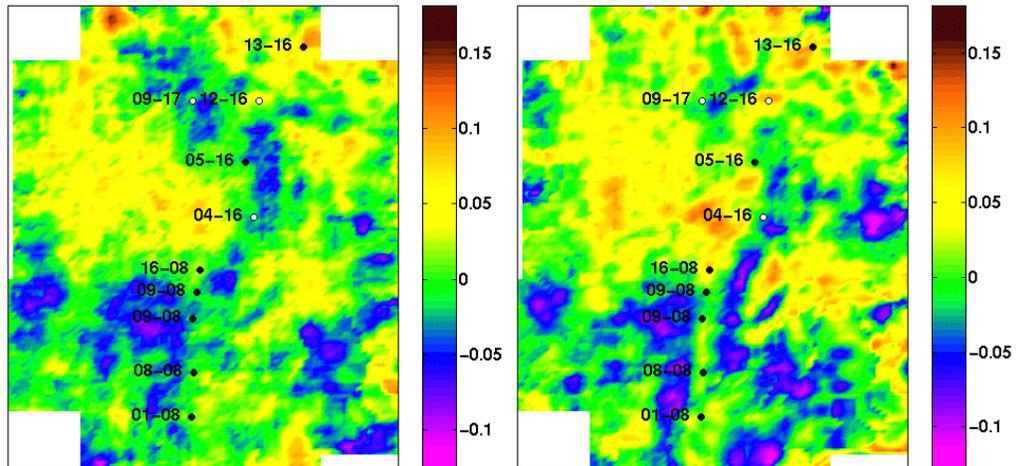
Figure 4.18: Weighted ΔI/I stacks for the P-P only (left) and simultaneous inversion methods (right) at the bottom of the Glauconitic channel.
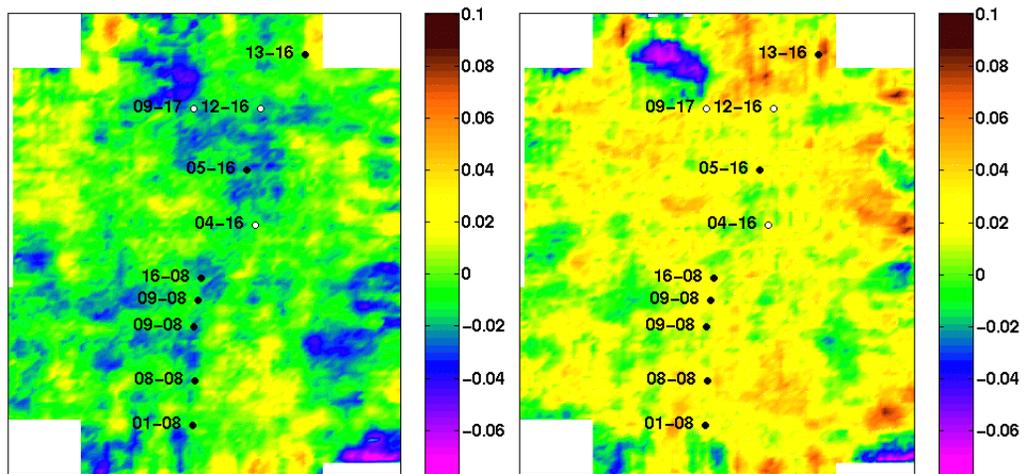
Figure 4.19: Weighted ΔJ/J stacks for the P-P only (left) and simultaneous inversion methods (right) at the bottom of the Glauconitic channel.
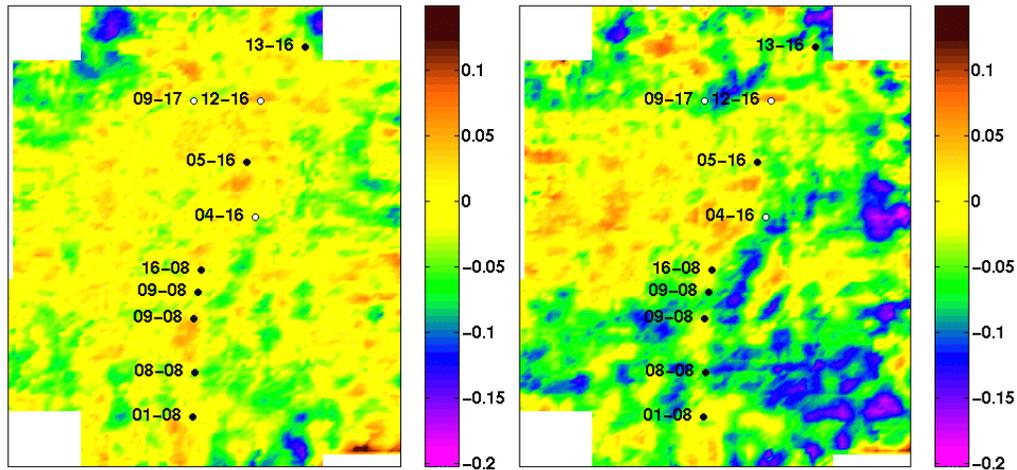
Figure 4.20: Weighted Δq/q stacks for the P-P only (left) and simultaneous inversion methods (right) at the bottom of the Glauconitic channel.

As shown in section 2.3.3 the parameters $\Delta I/I$ and $\Delta J/J$ can be recast into various elastic parameters that have the potential to improve petrophysical discrimination, i.e. the distinction between rock and/or fluid types. For the purposes of this study, the parameters examined are $\Delta(\lambda\rho)/\lambda\rho$, $\Delta(\lambda/\mu)/(\lambda/\mu)$, $\Delta\sigma/\sigma$ and $\Delta(\kappa\rho)/\kappa\rho$ where λ is the Lame compressibility modulus, μ is the Lame shear modulus, σ is Poisson's ratio and κ is the bulk modulus. The examination of these parameters involves applying different weights to each of the $\Delta I/I$ and $\Delta J/J$ timeslices and summing the result. As shown in equation 2.54, the $\Delta(\mu\rho)/\mu\rho$ parameter is equivalent to the $\Delta J/J$ section amplitudes multiplied by 2, thus no improvement in petrophysical discrimination is obtained. Similarly, equations 2.55 and 2.56 show the parameters $\Delta(\lambda/\mu)/(\lambda/\mu)$ and $\Delta\sigma/\sigma$ are equivalent to the $\Delta q/q$ timeslice amplitudes multiplied by a scalar value. Figure 4.21 shows the $\Delta(\lambda\rho)/\lambda\rho$ reflectivity stacks at the top of the Upper incised valley. Both inversion methods appear similar. The simultaneous inversion method does show a significant negative anomaly at wells 01-08 and 13-16 that more closely corresponds to the trend of the presumed Upper incised valley. Figure 4.22 shows the $\Delta(\lambda/\mu)/(\lambda/\mu)$ reflectivity stack for both inversion methods tested. The results appear quite similar to those obtained in figure 4.21. The simultaneous inversion results show a more distinct contrast between the presumed channel zone and the regional geology. In the case of the weighted $\Delta\sigma/\sigma$ and $\Delta(\kappa\rho)/\kappa\rho$

stacks shown in figures 4.23 and 4.24 respectively there again appears to be a negative reflectivity anomaly associated with the extent of the presumed Upper incised valley. The $\Delta(\kappa\rho)/\kappa\rho$ anomaly shown in figure 4.24 appears nearly identical for the two inversion methods tested. In this case both the P-wave inversion method and the simultaneous inversion method show a distinct channel boundary between wells 08-08 and 16-08.
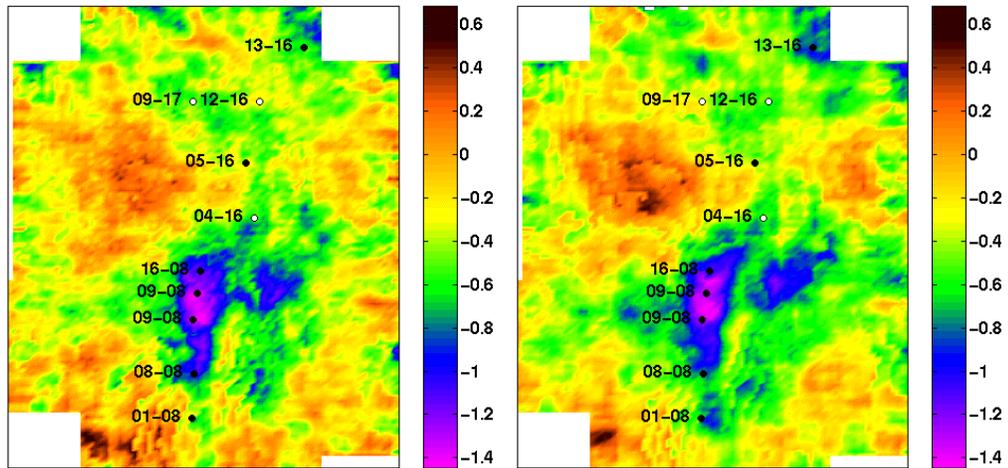

Figure 4.21: Weighted $\Delta(\lambda\rho)/\lambda\rho$ reflectivity stacks for the P-P only (left) and simultaneous inversion methods (right) at the top of the upper Glauconitic channel.
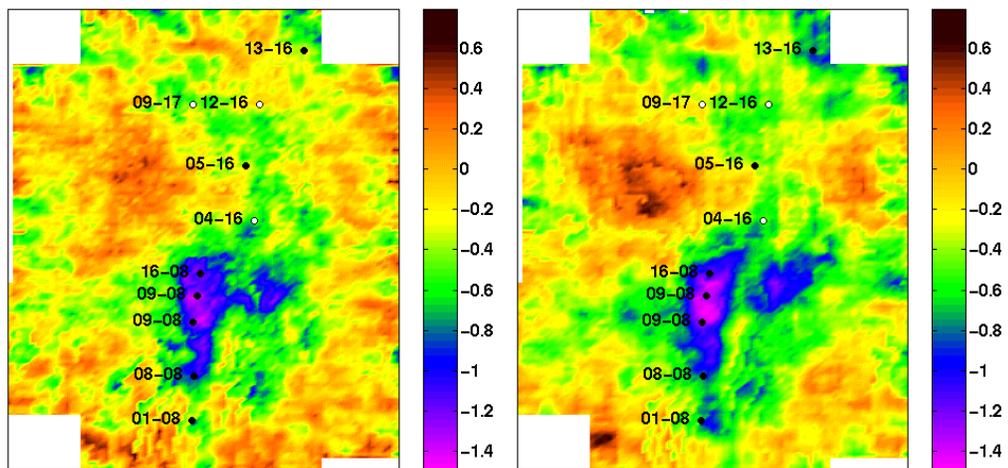
Figure 4.22: Weighted $\Delta(\lambda/\mu)/(\lambda/\mu)$ reflectivity stacks for the P-P only (left) and simultaneous inversion methods (right) at the top of the upper Glauconitic channel.
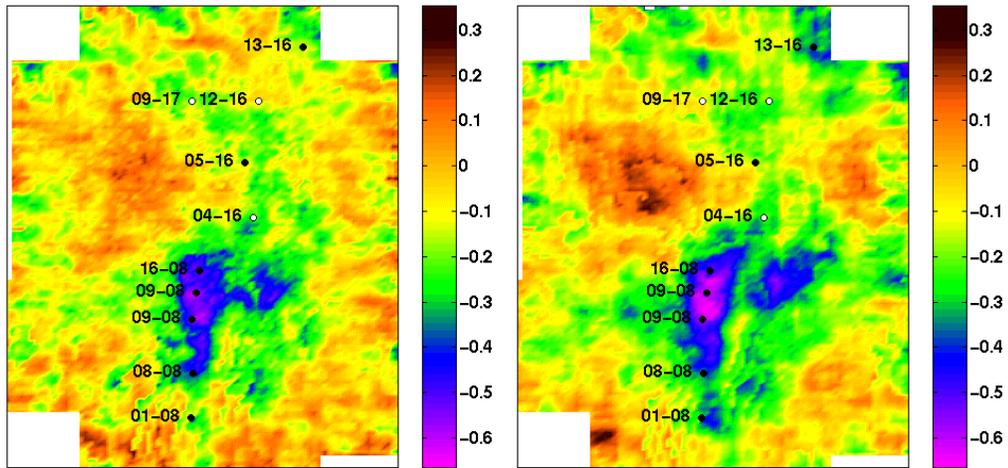
Figure 4.23: Weighted Δσ/σ (Poisson's ratio reflectivity) stacks for the P-P only (left) and simultaneous inversion methods (right) at the top of the upper Glauconitic channel.
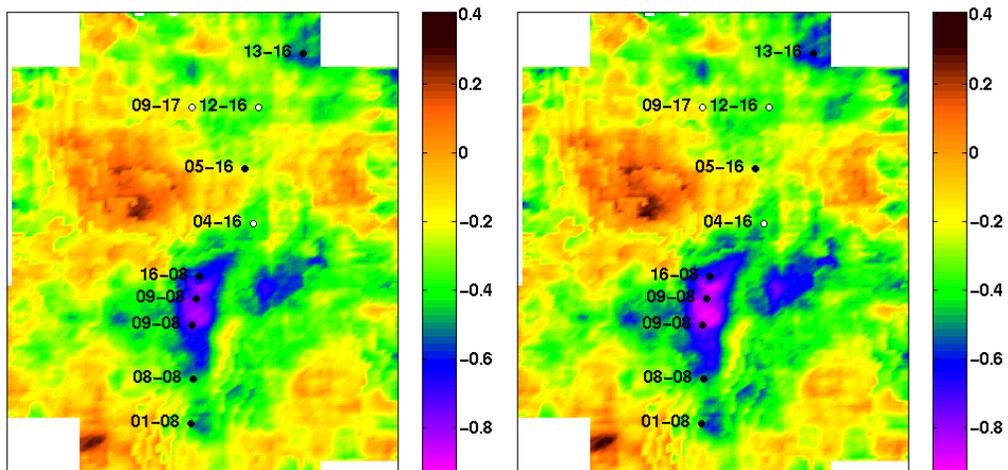
Figure 4.24: Weighted Δ(κρ)/κρ reflectivity stacks for the P-P only (left) and simultaneous inversion methods (right) at the top of the upper Glauconitic channel.

4.6 Chapter Summary

This chapter compared the application and results of the simultaneous P-P and P-S and P-P inversion methods as applied to the Blackfoot 3C-3D dataset. This procedure included basic processing flows for the vertical and radial component datasets. Next, a simple method for preserving relative amplitudes using multi-component synthetic seismogram data was discussed. An event correlation method based upon depth conversion from a common reflection horizon was reviewed. Following event correlation,

the application of the various weights for each dataset was discussed for the case of a set of limited-offset seismic gathers. Finally, the simultaneous inversion method was applied to processed, limited-offset and depth converted seismic gathers to extract elastic parameter reflectivity estimates of compressional and shear impedances. From these impedance reflectivity estimates, various Lame modulus, Poisson's ratio and bulk modulus reflectivity parameters were computed. It has been shown the simultaneous inversion method more closely corresponds to expected values from well logs and results in improvements in signal-to-noise over the P-P or "Smith-Gidlow" weighted stacking method.

CHAPTER 5

Conclusions and Future Work

5.1 Conclusions

P-P and P-S reflection amplitudes can be simultaneously inverted using weighted stacks and recursive inversion to provide broadband estimates of compressional and shear impedances or velocities. This method can be extended to the case of a 3-parameter inversion giving compressional and shear velocities and density estimates of the subsurface. It can further be shown the simultaneous 3-parameter weighted stack requires a shorter recording aperture than a 3-parameter method using P-P seismic data alone.

It was shown the 2-parameter simultaneous weighted stacking method was significantly more accurate than the P-P weighted stacking method in the presence of random noise. This effect was the result of doubling the data fold input into each estimate of compressional and shear impedance and modifying the weighting method to more equally weight each offset resulting in higher data fold for each compressional and shear impedance weighted stack. The addition of other reflection modes (S-P and S-S) should further increase the performance of the simultaneous inversion method in the presence of random noise.

The weighted stacking results from the Blackfoot 3C-3D show the P-P weighted stacking method does not adequately predict the extent of the upper incised-valley. The simultaneous weighted stacking method more clearly defines the upper incised valley, especially in the compressional impedance anomaly. The lower incised-valley is also better predicted using the simultaneous inversion method and the results in both cases more closely tie with expected results from blocked well logs.

5.2 Future Work

P-P and P-S event correlation methods should be tested for accuracy in areas of poor shear velocity control. A simple interpretive procedure should be accurate in such an area over a limited depth interval between two picked horizons. Conversion of P-P and P-S reflection events to depth relative to a common reflection horizon should also be tested for accuracy in such an area.

The effect of incorporating different reflection modes (S-P, S-S) in addition to the simultaneous P-P and P-S inversion method should be attempted. The effect upon inversion accuracy and noise suppression could be significant with the addition of these extra reflection modes. This test would require field data with both compressional and shear sources. These tests as a result would require additional seismic data acquisition costs over the data used in testing the simultaneous P-P and P-S inversion method.

The simultaneous P-P and P-S, 3-parameter linearized inversion method should be tested for viability and accuracy given bandlimited noisy seismic data. This method has the potential to extract normalized estimates of compressional and shear velocities and density values. Since three parameters would be available, lithology and pore fluid content changes could be more fully described using this inversion method. Since both P-P and P-S seismic data represent independent estimates of the same subsurface reflecting layers, this method should reduce the non-uniqueness problem inherent in 3-parameter inversion methods utilizing P-P seismic data only.

The non-linear Generalized Linear Inversion (GLI) simultaneous inversion method described in chapter 2 should be tested for P-P and P-S data with varying levels of noise. Preliminary tests show the non-linear inversion method is more sensitive to improper seismic processing and higher levels of noise than the linearized inversion method. The simultaneous non-linear inversion method does reduce the non-uniqueness problem inherent in the standard P-P GLI inversion method.

References

Aki, K., and Richards, P.G., 1980, Quantitative Seismology: Theory and Methods, W.H. Freeman and Company. Vol. 1.

Biot, M.A., 1956, The theory of propagation of elastic waves in a fluid-saturated solid, I lower frequency range, II higher frequency range: J. Acoust. Soc. Am., 28, 179-191.

Bortfeld, R. K. and Tan, T.H., 1984, A guide to true amplitude migration: 54th Annual Internat. Mtg., Soc. Expl. Geophys., Expanded Abstracts, Session:S19.1.

Castagna, J.P., Batzle, M.L., and Eastwood, R.L., 1985, Relationship between compressional and shear-wave velocities in clastic silicate rocks: Geophysics, 50, 551-570.

Castagna, J.P., Batzle, M.L., and Kan, T.K., 1993, Rock physics: the link between rock properties and AVO response in Castagna, J.P., and Backus, M.M., Eds., Offset-dependent reflectivity – Theory and practice of AVO analysis, Soc. Expl. Geophys., 135-171.

Chan, W. and Stewart, R.R., 1997, Logarithmic correlation of P-P and P-S seismic data: The CREWES Research Report, Vol. 9, Ch. 35.

Debski, W., and Tarantola, A., 1995, Information on elastic parameters obtained from the amplitudes of reflected waves: Geophysics, 60, 1426-1436.

Demirbag, E., and Çoruh, C., 1988, Inversion of Zoeppritz equations and their approximations: 58th Ann. Internat. Mtg., Soc. Expl. Geophys., Expanded Abstracts, 1199-1203.

Demirbag, E., Çoruh, C., and Costain, J.C., 1993, Inversion of P-wave AVO in Castagna, J.P., and Backus, M.M., Eds., Offset-dependent reflectivity – Theory and practice of AVO analysis, Soc. Expl. Geophys., 287-302.

Deregowski, S. M., 1990, Common-offset migrations and velocity analysis: First Break, 08, no. 06, 224-234.

Domenico, S.N., 1977, Elastic Properties of unconsolidated porous sand reservoirs: Geophysics, 42, 1339-1369.

Drufuca, G., and Mazzotti, A., 1995, Ambiguities in AVO inversion of reflections from a gas-sand: Geophysicss, 60, 134-141.

Dufour, J., Squires, J., Edmunds, A. and Shook, I., 1998, Integrated geological and geophysical interpretation of the Blackfoot area, Southern Alberta: Geo-Triad Expanded Abstracts, 234-236.

Fatti, J.L., Smith, G.C., Vail, P.J., Strauss, P.J., and Levitt, P.R., 1994, Detection of gas in sandstone reservoirs using AVO analysis: Geophysics, 59, 1362-1376.

Ferguson, R.J., and Stewart, R.R., 1996, Shear wave interval velocity from P-S stacking velocities: The CREWES Project Research Report, 8, Ch. 22.

Ferguson, R.J., 1996, P-S Seismic Inversion: Modeling, Processing, and Field Examples: M.Sc. Thesis.

Fuller, B.N., Iverso, W.P., and Smithson, S.B., 1989, AVO for thin bed detection: 59th Ann. Internat. Mtg., Soc. Expl. Geophys., Expanded Abstracts, 826-828.

Gardner, G.H.F., and Harris, M.H., 1968, Velocity and attentuation of elastic waves in sands: Society of Professional Well Log Analysts Annual Logging Symposium, 9th, New Orleans, La., 1968, Transactions, p. M1-M19.

Gardner, G. H. F., Gardner, L.W., and Gregory, A. R., 1974, Formation velocity and density: The diagnostic basis for stratigraphic traps: Geophysics, 39, 770-780.

Gidlow, P.M., Smith, G.C., and Vail, P.J., 1992, Hydrocarbon detection using fluid factor traces; A case history: SEG/EAGE Workshop.

Geis, W.T., Stewart, R.R., Jones, M.J., and Katopodis, P.E., 1990. Processing, correlating, and interpreting converted shear-waves from borehole data in southern Alberta: Geophysics, 55, 660-669.

Goodway, B., Chen, T., and Downton, J., 1997, Improved AVO fluid detection and lithology discrimination using Lame petrophysical parameters; "$\lambda\rho$", "$\mu\rho$" and "$\lambda\mu$ fluid stack", from P and S inversions: CSEG Expanded Abstracts, 148-151.

Gray, S.H., 1997, True-amplitude seismic migration: A comparison of three approaches: Geophysics, 62, 929-936.

de Haas, J.C., and Berkhout, A.J., 1988, On the information content of P-P, P-SV, SV-SV and SV-P reflections: 58th Ann. Internat. Mtg., Soc. Expl. Geophys., Expanded Abstracts, 1190-1194.

de Haas, J.C. and Berkhout, A. J., 1989, Practical approach to nonlinear inversion of amplitude versus offset information: 59th Annual Internat. Mtg., Soc. Expl. Geophys., Expanded Abstracts, 839.

Hampson, D. and Russell, B., 1990, AVO inversion: theory and practice: 60th Ann. Internat. Mtg., Soc. Expl. Geophys., Expanded Abstracts, 1456-1458.

Ito, H., Devilbiss, J., and Nur, A., 1979, Compressional and shear waves in saturated rock during water-steam transition: J. Geophys. Res., 84, 4731-4735.

Johnson, W. E., 1988, Amplitude versus offset for sandstones in shales and carbonates, 58th Ann. Internat. Mtg., Soc. Expl. Geophys., Expanded Abstracts, 593-595.

Koefoed, O., 1955, On the effect of Poisson's ratios of rock strata on the reflection coefficients of plane waves: Geophys. Prosp., 3, 381-387.

Krajewski, Paul, Krajewski, Christina and Grummt, Sabine, 1993, True-amplitude processing of P- and PS- (converted) -wave data for AVO-analysis: 55th Mtg. Eur. Assoc. Expl Geophys., Abstracts, Session:C013.

Kuster, G.T., and Töksoz, N.M., 1974, Velocity and attenuation of seismic waves in two-phase media, I. Theoretical formulations: Geophysics, 39, 607-618

Lawton, D.C., and Howell, T.C., 1992, P-P and P-SV synthetic stacks, Expanded Abstract, 62nd SEG Ann. Internat. Mtg., 1344-1347.

Lawton, D.C., Stewart, R.R., Cordsen, A., and Hrycak, S., 1996, Advances in 3C-3D design for converted waves: The CREWES Project Research Report, Vol. 8.

Layer, D.B., and Members of Staff, Imperial Oil Ltd., 1949, Leduc oil field, Alberta, a Devonian coral reef discovery: Bulletin of American Association of Petroleum Geologists, 33, 576-602.

Leckie, D.A., Bhattacharaya, J.P., Bloch, J., Gilboy, C.F., Norris, B., 1994, Cretaceous Colorado/Alberta Group of the Western Canadian Sedimentary Basin. In: Geological Atlas of the Western Canadian Sedimentary Basin. G.D. Mossop and

I. Shetsen (Comps.). Calgary, Canadian Society of Petroleum Geologists and Alberta Research Council, p. 335-352.

Lindseth, Roy O., 1979, Synthetic sonic logs - A process for stratigraphic interpretation: Geophysics, 44, no. 01, 3-26.

Lines, L.R., and Treitel, S., 1984, Tutorial: a review of least-squares inversion and its application to geophysical problems: Geophys. Prosp., 32, 159-186.

Lines, L.R., 1998, Density contrast is difficult to determine from AVO: CREWES Project Annual Research Report, Vol. 10, Ch. 47.

Macdonald, C., Davis, P.M., and Jackson, D.D., 1987, Inversion of reflection traveltimes and amplitudes: Geophysics 52, 606-617.

Margrave, G.F., and Foltinek D.F., 1995, Synthetic P-P and P-SV cross sections: CREWES Project Annual Research Report, Vol. 7, Ch. 5.

Mazzotti, A., 1984, Prestack analysis of seismic amplitude anomalies: 54th Annual Internat. Mtg., Soc. Expl. Geophys., Expanded Abstracts, 84, Session: S17.1. Menke, W., 1989, Geophysical data analysis: Discrete inverse theory: Academic Press Inc.

Miller, S.M.,1996, Multicomponent Seismic Data Interpretation: M.Sc. thesis, University of Calgary.

Murphy, W.F., 1982, Effects of microstructure and pore fluids on acoustic properties of granular sedimentary materials: Ph.D. dissertation, Stanford Univ.

Ostrander, W. J., 1982, Plane wave reflection coefficients for gas sands at nonnormal angles of incidence: 52nd Annual Internat. Mtg., Soc. Expl. Geophys., Expanded Abstracts, 82, Session:S16.4.

Pickett, G.R., 1963, Acoustic character logs and their application in formation evaluation: J. Petr. Tech., 15, 650-667

Ramirez, Luis C., 1990, AVO statistical analysis: A useful tool for interbedded salt body detection: 60th Annual Internat. Mtg., Soc. Expl. Geophys., Expanded Abstracts, 90, 1483-1485.

van Rijssen, E.P.F., and Herman, G.C., 1988, Resolution of elastic inversion: Presented at the 50th Mtg., Eur. Assn. Expl. Geophys.

Russell, B.H., 1988, Introduction to seismic inversion methods: SEG Continuing Education Course Note Series, Vol. 2, Soc. Expl. Geophys.

Schneider, J. and Krey, Th, 1985, True amplitude migration using the summation method: Some examples and practical aspects: 55th Annual Internat. Mtg., Soc. Expl. Geophys., Expanded Abstracts, Session:S8.6.

Sheriff, R.E., 1991, Encyclopedic dictionary of exploration geophysics, Soc. Expl. Geophys.

Shuey, R.T., 1985, A simplification of the Zoeppritz equations, Geophysics 50, 609-614.

Simin, V., Margrave, G.F. and Yang, G.C., 1996, AVO measurements for P-P and P-S data in the Blackfoot 3C-3D dataset: The CREWES Research Report, Vol. 8, Ch. 42.

Smith, G.C., and Gidlow, P.M., 1987, Weighted stacking for rock property estimation and detection of gas: Geophys. Prospec., 35, 993-1014.

Smith, G.C., 1996, 3-parameter geostack: 66th Annual Internat. Mtg., Soc. Expl. Geophys., Expanded Abstracts, 1747-1750.

Stewart, R.R., 1990, Joint P and P-SV inversion: The CREWES Project Research Report, Vol. 2, 112-115.

Stewart, R.R., 1994, The present and promise of P-S seismic exploration: The CREWES Project Research Report, Vol. 6, Ch. 1.

Stewart, R.R., Zhang, Q., and Guthoff, F., 1995, Relationships among elastic-wave values: Rpp, Rps, Rss, Vp, Vs, κ, σ and ρ: The CREWES Project Research Report, Vol. 7

Tatham, R.H., and Stoffa, P.L., 1976, Vp/Vs – A potential hydrocarbon indicator: Geophysics, 41, 837-849.

Toksöz, M.N., Cheng, C.H., and Timur, A.: 1976, Velocities of seismic waves in porous rocks: Geophysics, 41, 621-645.

Toksöz, M.N, Johnston, D.H., and Timur, A., 1979. Attenuation of seismic waves in dry and saturated rocks: Laboratory measurements: Geophysics, 44, 681-690.

Tsingas, C., and Kanasewich, E.R., 1991, Seismic reflection amplitude versus angle variations over a thermally enhanced oil recovery site: Geophysics, 56, 292-301.

Thomsen, L., 1990, Poisson was not a geophysicist: The Leading Edge, December 1990, 27-29.

Treitel, S., Gutowski, P.R., Hubral, P. and Wagner, D.E., 1981, Plane wave decomposition of seismograms, 51st Annual Internat. Mtg., Soc. Expl. Geophys., Reprints: , Session:S16.5.

Wang, Z., and Nur, A., Velocities in hydrocarbons and hydrocarbon-saturated rocks and sands: 57th Annual Internat. Mtg., Soc. Expl. Geophys., Expanded Abstracts, , Session:BHG1.1.

Wright, J., 1984, The effects of anisotropy on reflectivity-offset: 54th Annual Internat. Mtg., Soc. Expl. Geophys., Expanded Abstracts, 84.

Wood, J.M., and Hopkins, J.C., 1992, Traps associated with paleovalleys and interfluves in an unconformity bounded sequence: Lower Cretaceous Glauconitic Member, Southern Alberta, Canada: The American Association of Petroleum Geologists Bulletin, 76(6), 904-926.

Xu, Y., and Bancroft, J.C., 1997, Joint AVO analysis of PP and PS seismic data: The CREWES Project Research Report, Vol. 9.